UNIVERSITY OF CALIFORNIA
Santa Barbara

Quantum Optical Control of Single Spins in Diamond

A dissertation submitted in partial satisfaction
of the requirements for the degree of

Doctor of Philosophy

in

Physics

by

Christopher Gordon Yale

Committee in charge:

Professor David D. Awschalom, Chairperson

Professor Andrew N. Cleland

Professor Chetan Nayak

December 2015

The dissertation of Christopher Gordon Yale is approved:

Andrew N. Cleland

Chetan Nayak

David D. Awschalom, Committee Chairperson

September 2015

Quantum Optical Control of Single Spins in Diamond

Christopher Gordon Yale

to my parents who inspired in me a lifelong love of science,
and to my love, Anna-Marie, who inspires me everyday.

Acknowledgments

The science described in this thesis would not have been possible without the support and collaboration of many individuals. Foremost, I would like to thank my advisor, David Awschalom. Throughout my time in his group, I have come to truly appreciate the incredibly collaborative yet diversely independent approach that he fosters in the group, pulling together scientists with a wide array of interests and talents. David's enthusiasm and drive to explore new avenues of research provides each of us the support to pursue and develop our own experiments. It has been a privilege to have David as a mentor and friend.

A significant portion of my growth as a scientist can be attributed to two individuals who have served as mentors, colleagues, and friends throughout my time in the Awschalom group: Joe Heremans and Bob Buckley. Joe was one of the first guys that I met when I joined the group, and he's been one of my closest friends throughout graduate school. From those initial days showing me the ropes of confocal microscopy to working on our latest "Team Cold Diamond" projects, we've formed an incredible rapport bouncing crazy ideas off of one another. His incredible work ethic and ability to juggle multiple projects continue to amaze me, and I wish him the best of luck as he heads off to start a lab at Argonne National Lab. Bob Buckley and I worked together for several very fruitful years, and his drive and commitment were always impressive. As one of the cleverest scientists I've worked with, Bob is also very down-to-earth and was always willing to help flesh out any concept. Learning from and working with him was a privilege.

Having David Christle as a partner-in-crime during our first year locked away in the third floor office moving from problem set to problem set (and in particular, the impossible sphere held at alternating 'tangerine slice' potentials) made that first year immensely more tolerable, along with

unhealthy doses of Cactus Cooler, Michael Jackson, and Subway. Since then, his deep knowledge of Bayesian statistics and numerical modeling have been invaluable to several of our experiments, and his fearlessness to dive headfirst into a new challenge is admirable. In addition, I've had the pleasure of working with Lee Bassett, whose careful and deep thinking about science was worth every penny. In the past year, Brian Zhou has joined the Cold Diamond effort, and has become a valued member of the team. In particular, Brian has brought a new and different perspective that has been incredibly useful in developing the Berry phase work. With Brian's always inquisitive approach, I know that Team Cold Diamond is in excellent hands moving forward.

As part of the Cold Diamond effort, we've formed a very productive partnership with Guido Burkard's theory group at the University of Konstanz. Guido is a brilliant theorist who has provided a lot of the theoretical backing to a number of the projects on which I've worked. Just a Skype call away, Guido has a unique fascination with how the experiment works that is helpful as we work to bridge the gap between theory and experiment. More recently, we've been working with Adrian Auer from Guido's group. During our frequent calls to Germany, Adrian has been more than willing to implement any number of iterations and changes to the simulations, even as he was finishing up his own thesis. Both Guido and Adrian are excellent scientists, and it has been rewarding to work with them.

In addition to these individuals with whom I've worked closely, there are many other group members who have been excellent sounding boards and offer unique perspectives based on their many disparate projects and interests. Ken Ohno, my roommate throughout our time in Santa Barbara, was our resident diamond grower, and has a determination and drive that is unparalleled. Ken has been an excellent friend, and I've come to appreciate our many conversations, whether they be about science or an exchange

about Japanese and American cultures. Will Koehl, a fellow Texan, could always provide deep and considered thoughts on any subject, and I mean any. Upon moving the lab to Chicago, we merged the two separate lab locations from Santa Barbara, into one hallway, and as a result, I got to know Paolo Andrich much better, along with his enthusiasm and wonderful wackiness. Andrew Yeats always has a unique and creative solution up his sleeve to whatever experimental problem may come his way. I've had many a productive conversation with Charlie de las Casas as we bounce ideas off one another about our respective experiments. Abram Falk, a former postdoc and very talented scientist has been a wonderful resource along with his frank but good-humored approach. In addition, Paul Klimov has exhibited incredible dedication and adeptness in his scientific endeavors.

Everyone I've interacted with in David's group has been wonderful to work with including former post-docs: Greg Fuchs, Jayna Jones, Joerg Bochmann, Alberto Politi, and Benji Alemán, as well as former grad students: Greg Calusine, David Toyli, Brian Maertz, Viva Horowitz, Shawn Mack, and Mark Nowakowski. Best of luck to our newest crop of grad students: Chris Anderson, whose creativity and broad interests rival that of Joe, as well as Peter Mintun, Kevin Miao, Alex Crook, Berk Diler, Paul Jerger, Erzsebet Vincent, Masaya Fukami, and Alexandre Bourassa. I know the group has a bright future. Also, I'd like to acknowledge my committee members, Andrew Cleland and Chetan Nayak, who not only have been there to ask insightful questions and help guide my progress, but also taught two of the most enriching classes I took during my first year of grad school, the first quarter of quantum mechanics and statistical mechanics, respectively.

Behind the scenes, a great number of people have helped to ensure that we can do the science we want to do without having to deal with too much bureaucracy. In particular, at CNSI at UC Santa Barbara, Holly Woo, Eva

Deloa, Lynne Leininger, and Daniel Daniels have helped out in numerous ways. From the Physics department, Dave Prine always ensured we had liquid helium no matter what, and Mike Deal worked tirelessly to help keep our building running and functional. In our move to Chicago, Diana Morgan was particularly helpful in getting us all set up here in Chicago, and Mary Pat McCullough has been wonderful in helping out with a variety of issues the past few months. The projects presented in this thesis were largely funded by the Air Force Office of Scientific Research, as well as the Army Research Office, the Defense Advanced Research Projects Agency, and the National Science Foundation. (That is to say, taxpayers like you!)

Most importantly, I'd like to thank the first scientists I ever met, my parents, Leslie and David, for providing me with love and support throughout my life. Whether it was teaching me about different rock formations during our vacations, staring up at the night sky, or driving me all around town to sketch the spectra of different light sources for the science fair, they've always been there for me. In addition, my brother, Nate, has been the best brother anyone could ask for. I've known him his entire life, and he's been a wonderful accomplice in all of our shenanigans as we've grown up together. And finally, I'd like to thank my fiancée, Anna-Marie, whom I met when we audited all of our group's equipment, searching for ghosts of experiments past. Since then, she has always been there, and even moved halfway across the country for me. She is a constant inspiration, and I can't thank her enough for all of her support and love.

Vitæ

Education

2009 B.S., Physics, Yale University

2013 M.A., Physics, University of California, Santa Barbara

2015 Ph.D., Physics, University of California, Santa Barbara

Publications

"Optical manipulation of Berry phase in a solid-state spin qubit," C. G. Yale*, F. J. Heremans*, B. B. Zhou*, A. Auer, G. Burkard, and D. D. Awschalom, *submitted* (2015).

"Ultrafast optical control of orbital and spin dynamics in a solid-state defect," L. C. Bassett*, F. J. Heremans*, D. J. Christle, C. G. Yale, G. Burkard, B. B. Buckley, and D. D. Awschalom, *Science* **345**, 1333 (2014).

"All-optical control of a solid-state spin using coherent dark states," C. G. Yale*, B. B. Buckley*, D. J. Christle, G. Burkard, F. J. Heremans, L. C. Bassett, and D. D. Awschalom, *Proc. Natl. Acad. Sci. USA* **110**, 7595 (2013).

"Homoepitaxial growth of single crystal diamond membranes for quantum information processing," I. Aharonovich*, J. C. Lee*, A. P. Magyar, B. B. Buckley, C. G. Yale, D. D. Awschalom, and E. L. Hu, *Advanced Materials* **24**, OP54 (2012).

"Electrical Tuning of Single Nitrogen-Vacancy Center Optical Transitions Enhanced by Photoinduced Fields," L. C. Bassett*, F. J. Heremans*, C. G. Yale*, B. B. Buckley*, and D. D. Awschalom, *Phys. Rev. Lett.* **107**, 266403 (2011).

*denotes equal contribution

Fields of study

Major field: Physics

Quantum Optical Control of Single Spins in Diamond

Professor David D. Awschalom

Abstract

Quantum Optical Control of Single Spins in Diamond

by

Christopher Gordon Yale

The nitrogen-vacancy (NV) center in diamond has garnered great interest over the past decade as its electronic spin shows promise as a quantum bit (qubit) and nanoscale sensor. Consisting of a substitutional nitrogen adjacent to a vacant site within the carbon lattice of diamond, this defect exhibits millisecond-long spin coherence times extending beyond room temperature, spin-dependent optical addressability, coupling to intrinsic and nearby nuclear spins, and it can be controlled and manipulated through electrical, magnetic, and optical means. In particular, at cryogenic temperatures ($T < 25\,K$), the NV center's excited state becomes sharp and optically resolvable, providing a solid-state quantum optical testbed. In this thesis, I describe several experiments that explore this quantum optical interface to facilitate the development of a photonic network of single spins linked and controlled by light. We begin by exploring how electric fields tune the orbital levels within the NV center through the DC Stark effect, finding a surprising photo-induced field that aids in the ability to tune multiple NV centers' optical transitions to degeneracy. We then develop techniques to fully control the spin state of the NV center by coupling through a lambda (Λ) system, an energy configuration consisting of two lower levels coupled to one of higher energy. When a Λ system is optically driven, the spin becomes trapped in a dark state, or the eigenstate of the system that

is not coupled to the light fields through destructive interference, forming the basis for the various types of control demonstrated. We demonstrate arbitrary-basis initialization and readout of the spin state through coherent population trapping, as well as the ability to rotate about any arbitrary basis through stimulated Raman transitions. Combining these techniques, we measure the NV center's spin coherence through a completely optical measurement. We then extend these Λ system techniques to adiabatically move the dark state in trajectories around the Bloch sphere. Such trajectories accumulate a quantum mechanical phase that depends only on the geometry of the path enclosed, not on the energetics or time of the interaction. We characterize the interaction, measure this phase, known as Berry phase, and explore the limits of its control and resilience to noise. Finally, we demonstrate another all-optical control technique that uses strong ultrafast pulses of light to transfer the spin between the ground and excited states, deriving spin manipulation from the excited state dynamics. This technique also provides time-resolved spectroscopy of the excited state and its various decay and decoherence mechanisms. These experiments advance the progress toward the development of photonic networks coupling and controlling defects through light-matter interactions.

Contents

List of Figures

List of Tables

Chapter 1

Quantum optics and the NV center

1.1 Introduction

The interaction of light and matter underlies how we perceive and study the world around us. In particular, materials emit and absorb electromagnetic radiation in different ways, which is revealed through the distinct spectra of each material. In the late 1660s, Sir Isaac Newton discovered the dispersion of light into its component colors, or spectrum, through a prism [1]. Spectroscopy developed further with the experiments of Joseph von Fraunhofer using diffraction gratings in the early 1800s [2, 3]. By dispersing the light radiating from a material through a diffraction grating, distinct emission (bright) or absorption (dark) lines can be resolved within the visible spectrum. These lines act as a way to identify the constituent elements within a material.

The reasoning for these emission and absorption lines is understood through quantum mechanics. At its most basic level, when we examine the atoms that make up a material, we find that electrons within an atom have distinct energy levels, or eigenstates. A given energy separation, E, between these levels corresponds to a particular frequency of light, ν, such that

$$E = h\nu \tag{1.1}$$

where h is Planck's constant and ν is related to its wavelength, λ, through the speed of light $c = \lambda\nu$. An atom can absorb or emit radiation of that frequency, ν, causing a transition from one level to another. As we combine atoms to form macroscopic materials, the component atoms bond and develop a series of emission and absorption lines or bands that are the hallmark of that particular material.

One such material, diamond, sought after not only for its perceived rarity and beauty but also for its excellent thermal conductivity and extreme hardness, nominally does not emit or absorb electromagnetic radiation in the visible range. This is because when carbon bonds tetragonally in an sp^3 configuration, it forms a large energy bandgap. Bandgaps occur in semiconductors and insulators when no electron states exist at those energies. The bandgap of diamond is 5.5 eV, corresponding to light at a wavelength of 225 nm, well into the ultraviolet region. However, defects in the crystal lattice, such as vacancies, substitutional or interstitial atoms, and com-

plexes of these, can form energy levels that exist within this bandgap, allowing the emission and absorption of different wavelengths of visible or infrared light.

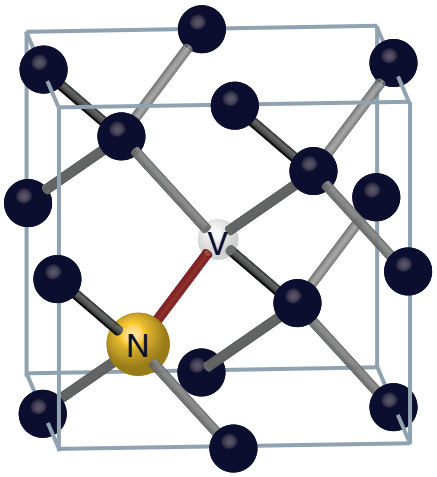

Figure 1.1: NV center schematic The NV center consists of a substitutional nitrogen (yellow) adjacent to a vacant site (transparent) within the sp^3 bonded carbon lattice (dark blue) of diamond.

Diamonds that appear yellow are due to significant amounts of substitutional nitrogen defects within the lattice. Likewise, diamonds that fluoresce blue under ultraviolet illumination are a result of a defect known as the N3 center, consisting of three substitutional nitrogen atoms surrounding a vacant site. In particular, this can be seen in these diamonds on bright sunny days. The rare and prized pink diamond is likely due to large concentrations of a particularly fascinating defect known as the nitrogen-vacancy (NV) center, a single substitutional nitrogen adjacent to a vacant site in the lattice, which emits red light (Fig. 1.1). This de-

fect in particular has garnered attention over the past decade as it acts as a trapped atom or molecule within the carbon lattice. When negatively charged, the defect consists of six electrons trapped closely to the defect site. The energy levels of these electrons give rise to a series of levels that exist within the bandgap of diamond, which will be discussed in detail later in this chapter (§1.6.1). The particulars of this energy configuration, the ability to isolate individual instances of these defects, and a long-lived spin coherence make the NV center a promising quantum bit (qubit) for quantum information processing as well as a capable and comprehensive nanoscale sensor. In this thesis, I will describe experiments that probe the interface between light and an individual NV center to fully control its spin through optical means. These demonstrations are important steps in the development of photonic networks of solid-state defects controlled and linked by light.

1.2 Quantum optics for quantum information processing

The study of the interaction between light and matter at its most fundamental levels is known as quantum optics. Until the development of quantum mechanics, the understanding of these interactions was largely empirical as seen in spectroscopy. While the exact nature of light had been debated for centuries as to whether it was corpuscular or wave-like.

Around the advent of the 20th century, Max Planck partially formulated light as existing in packets, or quanta, in order to model the behavior of blackbody radiation [4]. It was later expanded by Albert Einstein in his understanding of the photoelectric effect [5]. This description gained further traction, when, in 1913, Niels Bohr used the quantization of light along with the quantization of energy levels within atoms to describe the observed spectral emission of the hydrogen atom. As quantum mechanics further developed, the nomenclature "photon" was soon ascribed to these quanta of light having both a particle and wave-like nature.

With the advent of quantum mechanics, study of the fundamental interactions between photons and matter grew, but it was not until the development of the laser in the latter half of the 20th century [6], that this field truly developed. While quantum optics underlies significant advances in atomic and solid-state physics, such as the development of laser cooling, atomic clocks, frequency combs, photonic crystals, and Bose-Einstein condensates, this chapter will focus on using light to control individual quantum systems. Such efforts were pioneered in the 1990s by physicists including David Wineland and Serge Haroche who were awarded the Nobel Prize in Physics in 2012 for their experiments exploring the fundamental interactions of light and matter to control trapped ions [7] and individual photons [8], respectively.

The ability to control individual quantum systems is essential for the

development of quantum information processing (QIP). In this framework, an individual quantum system plays the role of a quantum bit, or qubit. A qubit is analogous to a bit of information found in a classical computer. Classically, a bit has two distinct states, on and off (0 or 1). A qubit instead takes advantage of the probabilistic nature of quantum mechanics. Here, a qubit can exist in either 0 or 1, as well as any superposition of those two states, much like the famous Schrödinger's cat. Qubits come in many flavors, from trapped ions to superconducting Josephson junctions; however, our qubit of choice is the diamond NV center. To develop protocols for QIP, it is necessary to have the ability to initialize a qubit into a particular state, rotate from one state to another in a quantum gate, and to readout its final state. As I discuss below, light provides the control field mechanism for such a qubit.

1.3 The dipole interaction

To develop an understanding of the interaction of light with a qubit, we begin by investigating the effect of an external electromagnetic field on that of an electron bound to an atom. We start with the time-dependent Schrödinger equation,

$$i\hbar\frac{\partial}{\partial t}\left|\psi\right\rangle = \hat{H}\left|\psi\right\rangle, \tag{1.2}$$

which describes how a quantum system evolves in time, where $\hat{H}$ is the Hamiltonian of the system, $|\psi\rangle$ is the wavefunction describing the quantum

state, and $\hbar = h/2\pi$. The standard Hamiltonian for an electron bound to an atom (or a defect) is given by,

$$\hat{H}_0 = \frac{1}{2m}\hat{\boldsymbol{P}}^2 + V(r), \tag{1.3}$$

where $\hat{\boldsymbol{P}} = -i\nabla$ and $V(r)$ describes the binding interaction (in the case of atoms, this is the Coulomb interaction) which determines the energy structure of the given quantum system. In complex combinations of atoms, such as crystal lattices, whole fields of study exist to determine these energy levels and bands. The energy level structure is the series of eigenstates, or solutions of $\hat{H}_0$, $|\psi_{0,n}\rangle$ with eigenenergy E_n. In our case, we are interested in what happens to this quantum system in the presence of an external field. This interaction Hamiltonian takes the form of a dipole interacting with an external field,

$$\hat{H}_E = -\hat{\boldsymbol{d}} \cdot \boldsymbol{F}(t), \tag{1.4}$$

$$\hat{H}_B = -\hat{\boldsymbol{\mu}} \cdot \boldsymbol{B}(t), \tag{1.5}$$

where $\hat{\boldsymbol{d}}$ and $\hat{\boldsymbol{\mu}}$ are the electric and magnetic dipoles, and $\boldsymbol{F}(t)$ and $\boldsymbol{B}(t)$ are the electric and magnetic fields. A complete derivation of these interaction Hamiltonians can be found in [9].

From this interaction, given different types of driving fields, detunings, and level configurations, we can derive various important phenomena in quantum optics relevant to the experiments discussed in this thesis. While certain aspects of quantum optics rely upon full quantization of the elec-

tromagnetic field, for the purpose of this dissertation, it is not necessary, so we will restrict ourselves to a semiclassical description of the radiation.

We begin by looking at the effect of a fixed electric field, with no time dependence, $\boldsymbol{F}(t) = \boldsymbol{F}$, on transitions within an atom or defect. This was first discovered by Johannes Stark in 1913 when he observed spectral lines of various atoms and molecules shift in response to an external fixed electric field [10]. These shifts are a direct result of the electric dipole Hamiltonian. If we view the electric dipole interaction Hamiltonian $\hat{H}_E$ as a perturbation on $\hat{H}_0$, we find the first order shift of the eigenenergies E'_n, for eigenstates $|\psi_{0,n}\rangle$ is given by,

$$E'_n = \langle\psi_{0,n}| - \hat{\boldsymbol{d}} \cdot \boldsymbol{F} \, |\psi_{0,n}\rangle = -\boldsymbol{F} \cdot \langle\hat{\boldsymbol{d}}\rangle_n. \tag{1.6}$$

Essentially, to first order, the energy of various levels shifts linearly within the system as a function of field strength and the dipole associated with the transition. Quadratic and higher order effects can similarly be derived through higher order perturbation theory. In terms of the NV center, there is an electric dipole associated with transitions between different orbital levels, and these orbitals shift with the application of external electric fields fields as well as internal strain, and an experiment describing these effects is found in Ch. 2.

Similarly, any eigenstates associated with a magnetic dipole moment can shift according to the Zeeman effect through the application of a magnetic field. In the NV center, this corresponds to the spin sublevels within

the various orbital levels, and the effect can be derived in a similar manner.

1.4 Two-level systems

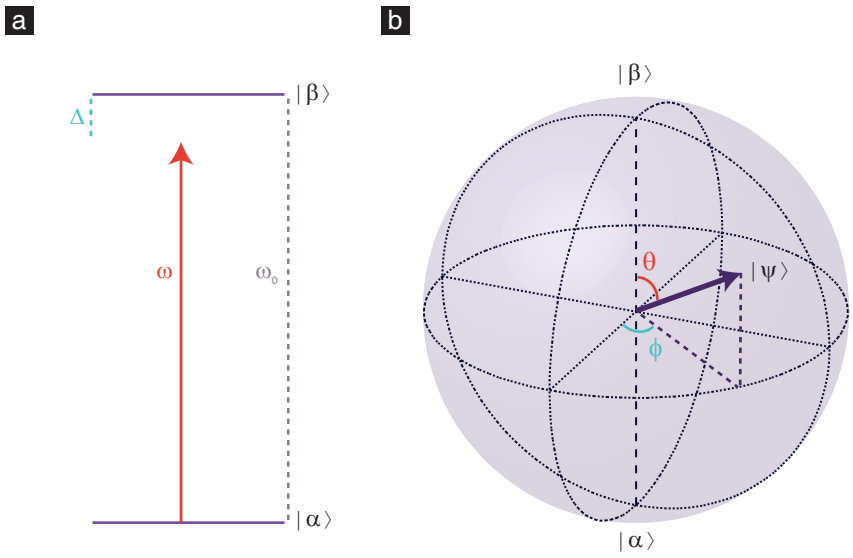

Figure 1.2: Two-level system and Bloch sphere representation a) Two levels $|\alpha\rangle$ and $|\beta\rangle$ are separated by energy, $\hbar\omega_0$, and are excited by electromagnetic radiation (laser or microwave source) at energy, $\hbar\omega$, detuned by $\hbar\Delta = \hbar\omega_0 - \hbar\omega$. **b)** Bloch sphere representation of a two level system spanned by $|\alpha\rangle$ and $|\beta\rangle$. Any superposition of these two states, $|\psi\rangle$, exists on the surface of the sphere and is defined by the polar angle, θ, and azimuthal angle, ϕ. The superposition state $|\psi\rangle$ is fixed on the sphere when observed in the rotating frame of the energy separation, $\hbar\omega_0$.

To further explore the dipole interaction, we examine a two-level system (Fig. 1.2a), with the unperturbed Hamiltonian $\hat{H}_0$ in matrix notation:

$$\hat{H}_0 = E_\alpha |\alpha\rangle \langle\alpha| + E_\beta |\beta\rangle \langle\beta| = \begin{pmatrix} E_\alpha & 0 \\ 0 & E_\beta \end{pmatrix}. \tag{1.7}$$

This Hamiltonian is spanned by its eigenstates:

$$|\alpha\rangle = \begin{pmatrix} 1 \\ \\ 0 \end{pmatrix} \qquad\qquad |\beta\rangle = \begin{pmatrix} 0 \\ \\ 1 \end{pmatrix}, \tag{1.8}$$

with energies E_α and E_β, respectively. The energy difference between the states can be related to an angular frequency, ω_0, as $E_\beta - E_\alpha \equiv \omega_0$. We can also define a state that is a superposition of these two eigenstates $|\alpha\rangle$ and $|\beta\rangle$. Such a state lies on the Bloch sphere, or the surface corresponding to all possible superpositions. These superpositions take the form:

$$|\psi(t)\rangle = \cos(\theta)\,|\alpha\rangle + \sin(\theta)e^{-i\phi}\,|\beta\rangle = \begin{pmatrix} \cos(\theta) \\ \\ \sin(\theta)e^{-i\phi} \end{pmatrix}, \tag{1.9}$$

where θ defines the polar, or altitudinal position of the superposition state on the Bloch sphere, while ϕ defines the azimuthal position of that superposition state (Fig. 1.2b).

1.4.1 Rabi oscillations

Now, by examining the effect of a time varying field on this two-level system, we find a number of important interactions. In this case, we look at an electric field of the form $\boldsymbol{F}(t) = \boldsymbol{F}\cos(t)$. The electric dipole operator takes the form:

$$\hat{\boldsymbol{d}} = \boldsymbol{d}\,|\alpha\rangle\langle\beta| + \boldsymbol{d}^*\,|\beta\rangle\langle\alpha| \tag{1.10}$$

Thus our interaction Hamiltonian is,

$$\hat{H}_i = \hat{\boldsymbol{d}} \cdot \boldsymbol{F}(t) = \hbar \begin{pmatrix} 0 & \Omega\cos(\omega t) \\ \Omega\cos(\omega t) & 0 \end{pmatrix}, \tag{1.11}$$

where $\boldsymbol{d} \cdot \boldsymbol{F} = \hbar\Omega$. A similar derivation to what is described below can be done to describe an AC magnetic field interacting with spin sublevels, and the effect is essentially the same.

We define an arbitrary time-evolving superposition state that consists of $|\alpha\rangle$ and $|\beta\rangle$ with state amplitudes C_α and C_β, which takes the form:

$$|\psi(t)\rangle = \begin{pmatrix} C_\alpha(t)e^{-iE_\alpha t/\hbar} \\ C_\beta(t)e^{-iE_\beta t/\hbar} \end{pmatrix} = e^{-iE_\alpha t/\hbar} \begin{pmatrix} C_\alpha(t) \\ C_\beta(t)e^{-i\omega_0 t} \end{pmatrix}, \tag{1.12}$$

which is rewritten to extract a global phase $E_\alpha t/\hbar$. This leaves a phase relation between the $|\alpha\rangle$ and $|\beta\rangle$ components equivalent to $\omega_0 t$. This can be thought of as a point oscillating at frequency ω_0 on a fixed Bloch sphere, or a fixed point on a Bloch sphere that is rotating about its energy eigenstate axis at frequency ω_0. The point precessing at ω_0 is observed in the "lab frame," while if we jump onto the rotating Bloch sphere, we now observe a fixed point in the "rotating frame" of the two-level system. We now look at this state in the context of the interaction Hamiltonian within the Schrödinger equation,

$$\begin{aligned} \frac{i\hbar\partial\,|\psi(t)\rangle}{\partial t} &= \left(\hat{H}_0 + \hat{H}_i\right)|\psi(t)\rangle \\ &= \hbar e^{-iE_\alpha t/\hbar} \begin{pmatrix} \omega_\alpha & \Omega\cos(\omega t) \\ \Omega\cos(\omega t) & \omega_\beta \end{pmatrix} \begin{pmatrix} C_\alpha(t) \\ C_\beta(t)e^{-i\omega_0 t} \end{pmatrix}. \end{aligned} \tag{1.13}$$

Solving this, we find a series of coupled equations describing the state amplitudes:

$$\frac{\partial C_\alpha}{\partial t} = -i\Omega \cos(\omega t) e^{-i\omega_0 t} C_\beta, \tag{1.14}$$

$$\frac{\partial C_\beta}{\partial t} = -i\Omega \cos(\omega t) e^{i\omega_0 t} C_\alpha. \tag{1.15}$$

We expand the $\cos(\omega t)$ in exponentials,

$$\frac{\partial C_\alpha}{\partial t} = -\frac{i\Omega}{2}\left(e^{-i(\omega_0-\omega)t} + e^{-i(\omega_0+\omega)t}\right) C_\beta, \tag{1.16}$$

$$\frac{\partial C_\beta}{\partial t} = -\frac{i\Omega}{2}\left(e^{i(\omega_0+\omega)t} + e^{i(\omega_0-\omega)t}\right) C_\alpha. \tag{1.17}$$

In these equations, for $\omega \sim \omega_0$, we now see a co-rotating term, oscillating at $\omega_0 - \omega \equiv \Delta$, defined as the one-photon detuning. It also includes a counter-rotating term, oscillating at $\omega_0 + \omega$. As long as $\omega \ll \Omega$, we can eliminate this counter-rotating term in what is known as the rotating wave approximation, leading to:

$$\frac{\partial C_\alpha}{\partial t} = -\frac{i\Omega}{2} e^{-i\Delta t} C_\beta, \tag{1.18}$$

$$\frac{\partial C_\beta}{\partial t} = -\frac{i\Omega}{2} e^{i\Delta t} C_\alpha. \tag{1.19}$$

We have now entered the rotating frame of the driving field, ω, and the state now precesses at the one-photon detuning, Δ, relative to our rotating frame. Now eliminating C_α, we arrive at

$$\frac{\partial^2 C_\beta}{\partial t^2} - i\Delta \frac{\partial C_\beta}{\partial t} + \frac{\Omega^2}{4\hbar^2} C_\beta = 0. \tag{1.20}$$

The general solution to this is given by:

$$C_\beta(t) = A_+ e^{i\chi_+ t} + A_- e^{i\chi_- t}, \tag{1.21}$$

where

$$\chi_{\pm} = \frac{1}{2}(\Delta \pm \Omega_R), \tag{1.22}$$

and

$$\Omega_R = \sqrt{\Delta^2 + \Omega^2}. \tag{1.23}$$

We define Ω_R as the Rabi frequency, where at $\Delta = 0$, $\Omega_R = \Omega$. Now assuming that we begin with the level $|\alpha\rangle$ occupied and $|\beta\rangle$ empty i.e. $C_\alpha(0) = 1$ and $C_\beta(0) = 0$, this sets conditions on the amplitudes A_+ and A_-, which lead to the following solutions:

$$C_\beta(t) = \frac{i\Omega}{\Omega_R} e^{\frac{-i\Delta t}{2}} \sin\left(\frac{\Omega_R t}{2}\right), \tag{1.24}$$

$$C_\alpha(t) = e^{\frac{-i\Delta t}{2}} \left[\cos\left(\frac{\Omega_R t}{2}\right) + \frac{i\Delta}{\Omega_R} \sin\left(\frac{\Omega_R t}{2}\right)\right]. \tag{1.25}$$

The probability the state will occupy $|\beta\rangle$ as a function of time is given by:

$$P_\beta(t) = |C_\beta(t)|^2 = \frac{\Omega^2}{\Omega_R^2} \sin^2\left(\frac{\Omega_R t}{2}\right) = \frac{\Omega^2}{\Omega_R^2}\left[\frac{1}{2} - \frac{1}{2}\cos(\Omega_R t)\right]. \tag{1.26}$$

Likewise,

$$P_\alpha(t) = |C_\alpha(t)|^2 = 1 - \frac{\Omega^2}{\Omega_R^2}\left[\frac{1}{2} - \frac{1}{2}\cos(\Omega_R t)\right]. \tag{1.27}$$

These probabilities can be observed if we monitor the state occupation as a function of time, and their salient features are seen in Fig. 1.3. For $\Delta = 0$, full complete oscillations are seen between $|\alpha\rangle$ and $|\beta\rangle$ at a frequency $\Omega_R = \Omega$. In the Bloch sphere picture, these oscillations appear as a rotation about an equatorial axis on the rotating frame Bloch sphere. As we detune

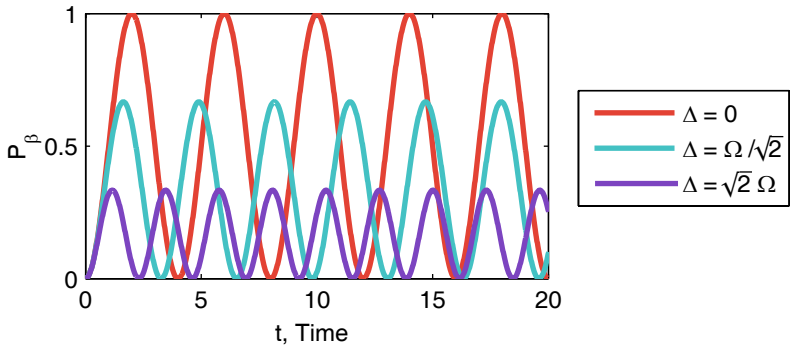

Figure 1.3: Rabi oscillations Probability of the state, beginning in $|\alpha\rangle$, being in $|\beta\rangle$ as a function of time, t, for various detunings, Δ.

the driving frequency ω from resonance at ω_0, the Rabi oscillations increase in frequency, but do not fully populate the opposite state, $|\beta\rangle$.

This type of interaction is necessary in many of the experiments discussed in this thesis. In particular, we use microwaves to drive oscillations between spin sublevels of the NV center ground state. Likewise, resonant light can be used to drive oscillations between the ground and excited state orbitals of the NV center. Ideally, these pulses are on resonance allowing for full population inversion. A π pulse is defined as a pulse that fully inverts the population of the initial state, while a $\pi/2$ pulse is defined as a pulse that rotates the spin halfway, typically from a pole to the equator, or from the equator to a pole. These $\pi/2$ pulses are typically used to project from one basis to another.

1.4.2 The rotating frame

An alternative approach to entering the rotating frame is accomplished by applying a transformation to the wavefunction, $U^\dagger |\psi\rangle$, where

$$U = \begin{pmatrix} 1 & 0 \\ 0 & e^{-i\omega t} \end{pmatrix}, \tag{1.28}$$

which then leads to a transformation of the Hamiltonian:

$$\frac{i\hbar\partial U^\dagger |\psi(t)\rangle}{\partial t} = U^\dagger \frac{i\hbar\partial |\psi(t)\rangle}{\partial t} + i\hbar \frac{\partial U^\dagger}{\partial t} |\psi(t)\rangle , \tag{1.29}$$

$$\frac{i\hbar\partial U^\dagger |\psi(t)\rangle}{\partial t} = U^\dagger H U U^\dagger |\psi(t)\rangle - \hbar\omega U^\dagger |\psi(t)\rangle , \tag{1.30}$$

$$\tilde{H} = U^\dagger H U - \hbar\omega |\beta\rangle \langle\beta| . \tag{1.31}$$

In the case of the two-level system described above, we arrive at a transformed rotating frame Hamiltonian:

$$\tilde{H} = \hbar \begin{pmatrix} \omega_\alpha & \frac{\Omega}{2}(1 + e^{-2i\omega t}) \\ \frac{\Omega}{2}(1 + e^{2i\omega t}) & \omega_\beta - \omega \end{pmatrix}. \tag{1.32}$$

Eliminating the counter-rotating terms (rotating at 2ω) per the rotating wave approximation, and additionally subtracting a constant ω_α yields the rotating frame Hamiltonian:

$$\tilde{H}' = \tilde{H} - \hbar\omega_\alpha I = \hbar \begin{pmatrix} 0 & \frac{\Omega}{2} \\ \frac{\Omega}{2} & \Delta \end{pmatrix}, \tag{1.33}$$

where $\Delta = \omega_0 - \omega$. For the rest of this chapter, we will investigate interactions in the context of their rotating frame Hamiltonians.

1.4.3 The AC Stark effect

One such effect that can be understood within a rotating frame two-level system, is known as the AC Stark effect, or Autler-Townes effect. In this instance, we once again begin with our levels $|\alpha\rangle$ and $|\beta\rangle$. However, in this case we are looking at instances where a significant one-photon detuning, Δ, exists between the driving field and the energy transition, such that there is little absorption. We begin with the two-level system in the rotating frame of the driving fields, equation 1.33.

The eigenstates of this driven Hamiltonian differ from the undriven Hamiltonian, and are known as dressed states. These dressed states are mixtures of the bare electronic energy levels, $|\alpha\rangle$ and $|\beta\rangle$, and the electromagnetic field driving the system. In this rotating frame, our bare states $|\alpha\rangle$ and $|\beta\rangle$ have an energy separation of the one-photon detuning, $\hbar\Delta$. Here, when we diagonalize the matrix, we find that the eigenenergies of the dressed states are given by:

$$E_{\pm} = \frac{\hbar\Delta}{2} \pm \frac{\hbar\sqrt{\Delta^2 + \Omega^2}}{2} \tag{1.34}$$

In Fig. 1.4, we see the bare levels split further into the dressed states, now separated by $\hbar\sqrt{\Delta^2 + \Omega^2}$. One way to observe this additional energy shift, or AC Stark shift, is when referenced to a third undriven, unshifted level. If we now look at the rotating frame defined by the reference level and one of our bare states, we see the AC Stark shift manifests as addi-

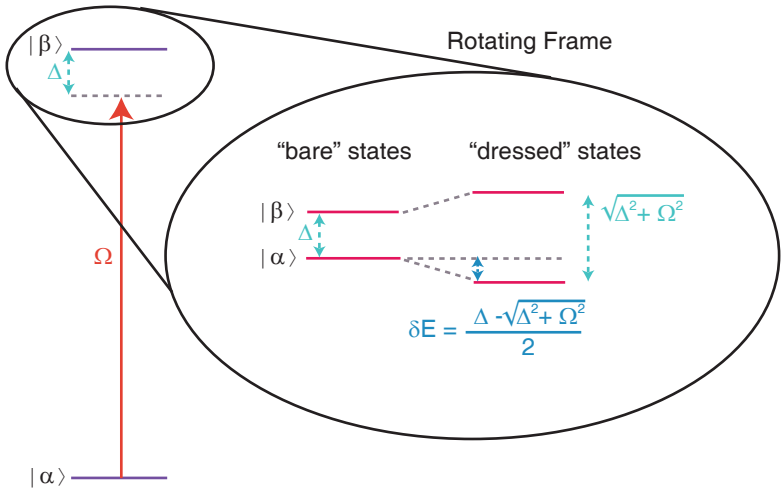

Figure 1.4: AC Stark effect Two-level system ($|\alpha\rangle$ and $|\beta\rangle$) driven at Ω with detuning, Δ, transformed into the rotating frame. In the rotating frame, the bare states (left), $|\alpha\rangle$ and $|\beta\rangle$, are separated by Δ. However, the eigenstates of this driven Hamiltonian, are the dressed states (right), which are separated by $\sqrt{\Delta^2 + \Omega^2}$, resulting in an energy shift from the bare to dressed states of $\pm\left(\frac{\Delta - \sqrt{\Delta^2+\Omega^2}}{2}\right)$.

tional precession of a quantum state in the predefined frame. These AC Stark shifts play important roles in realizing all-optical control of individual defects, and will be explored further in Ch. 3 and Ch. 4. In addition, while the AC Stark effect describes the role that the light plays upon the a quantum mechanical system (such as the spin of a defect), the system itself also affects the light through the Faraday effect. A derivation of both of these effects and their relation can be found in B. B. Buckley's thesis [11].

1.5 Three-level systems (Λ systems)

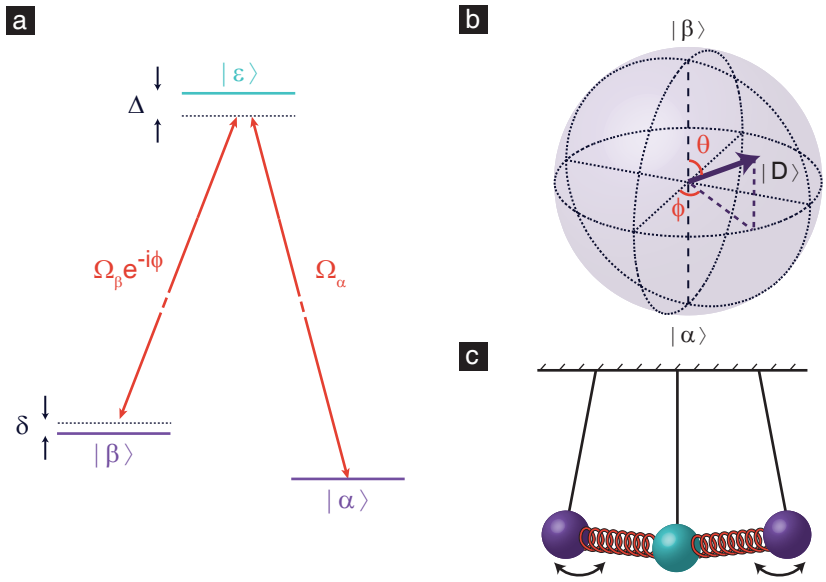

Figure 1.5: **Λ system and the dark state a)** Three-level system consisting of $|\alpha\rangle$, $|\beta\rangle$, and $|\varepsilon\rangle$ in a Λ (lambda) configuration. The two lower levels, $|\alpha\rangle$ and $|\beta\rangle$, are coupled to the excited state, $|\varepsilon\rangle$, by two driving fields, Ω_α and $\Omega_\beta e^{-i\phi}$. The one-photon detuning, Δ, and the two-photon detuning, δ, are indicated on the diagram. **b)** The zero-energy eigenstate of a Λ driven on resonance is the dark state, $|D\rangle = \cos(\theta/2)\,|\alpha\rangle - \sin(\theta/2)e^{-i\phi}\,|\beta\rangle$, where ϕ is the relative phase between the driving fields, and $\theta = 2\tan^{-1}(\Omega_\alpha/\Omega_\beta)$. This dark state is a superposition of the two lower levels and does not couple to the excited state. Its position on the Bloch sphere is fully defined by the relative pump intensities and phase relation. **c)** A classical analogue of a Λ system is given by three coupled pendula. The "dark" mode of this system is when the two outer pendula oscillate, while the center pendulum is unmoved. The spring constants of the coupling springs are analogous to the driving strengths, Ω_α and $\Omega_\beta e^{-i\phi}$.

If we expand our discussion of light-matter interactions by adding a third level, we can realize an energy configuration known as a Λ (lambda) system, with its energy levels forming a shape similar to the Greek letter

whose name it bears. Consisting of two lower levels, $|\alpha\rangle$ and $|\beta\rangle$, coupled to one upper level, $|\varepsilon\rangle$ (Fig. 1.5a), Λ systems have been used to realize myriad advances in quantum science including electromagnetically induced transparency, slow light, atomic clocks, laser cooling, and spin-photon entanglement. If we drive the Λ system along both transitions with optical pumps, Ω_α and $\Omega_\beta e^{-i\phi}$, we find a general Hamiltonian in the rotating frame that takes the form:

$$\tilde{H}' = \hbar \begin{pmatrix} 0 & 0 & \frac{\Omega_\alpha^*}{2} \\ 0 & \delta & \frac{\Omega_\beta^*}{2} e^{i\phi} \\ \frac{\Omega_\alpha}{2} & \frac{\Omega_\beta}{2} e^{-i\phi} & \Delta \end{pmatrix}, \tag{1.35}$$

in the basis $\{|\alpha\rangle, |\beta\rangle, |\varepsilon\rangle\}$, where Δ is the one-photon detuning, δ is the two-photon detuning, and ϕ is the relative phase between the driving fields.

1.5.1 What is a dark state?

If examine a Λ system that is driven exactly on resonance (i.e. $\delta = 0, \Delta = 0$), we find a solution that has an eigenenergy of zero. This eigenstate is known as the dark state as it does not couple to the light fields driving the system due to destructive interference. When the system is in the dark state it no longer absorbs photons, and it does not contain any of the excited state in its form:

$$|D\rangle = \frac{\Omega_\beta}{\sqrt{\Omega_\alpha^2 + \Omega_\beta^2}} e^{-i\phi} |\alpha\rangle - \frac{\Omega_\alpha}{\sqrt{\Omega_\alpha^2 + \Omega_\beta^2}} |\beta\rangle . \tag{1.36}$$

This can be rewritten with $\theta \equiv 2\tan^{-1}(\Omega_\alpha/\Omega_\beta)$, and an overall phase resulting in:

$$|D\rangle = \cos\left(\frac{\theta}{2}\right)|\alpha\rangle - \sin\left(\frac{\theta}{2}\right)e^{i\phi}|\beta\rangle\,. \tag{1.37}$$

This form reveals that the relative phase of the pumps defines where the dark state superposition lies azimuthally on the rotating frame Bloch sphere, while the relative amplitude between the pumps defines its altitudinal location (Fig. 1.5b). A classical analogue to this dark eigenstate is three pendula coupled by a springs, as seen in Fig. 1.5c. The "dark" solution to the coupled pendula problem is the mode in which the two outer pendula oscillate back and forth, while the center pendulum remains motionless. The oscillation of the outer pendula depends on the spring constants of the coupling springs, much like the form of the superposition depends on the relative strength and phase of the driving fields.

The dark state was first observed spectroscopically as a dip in the absorption of light through coherent population trapping (CPT) in atomic gasses in 1978 [12]. The dark state has been explored as a way to affect light transmission, as in electromagnetically induced transparency (EIT) where a material becomes transparent to a typically absorptive wavelength [13]. Such interactions can also cause a decrease in the group velocity of light, a phenomenon known as slow light. In addition, the dark state is used in protocols for highly efficient population transfer of quantum states, such as stimulated Raman adiabatic passage (STIRAP) [14].

For this thesis, several of the experiments focus on the ability to control precisely where the dark state is on the Bloch sphere through the relative amplitude and phase of the optical pumps. This allows us to develop all-optical control protocols based on coherent population trapping, CPT, and the AC Stark effect in a Λ system in Ch. 3. This is further developed using phase-controlled STIRAP to enclose a geometric phase, or Berry phase, in Ch. 4.

1.5.2 Coherent population trapping (CPT)

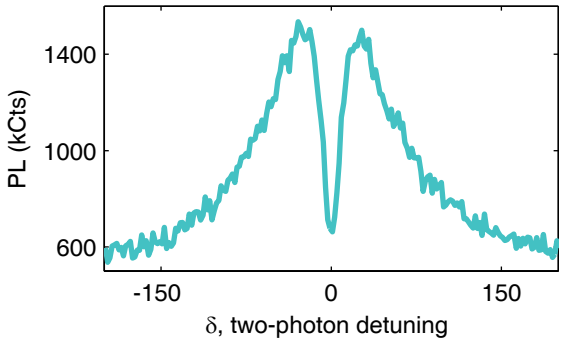

Figure 1.6: Coherent population trapping (CPT) dip An example spectroscopic CPT dip as seen on the $|A_2\rangle$ level of the NV center in diamond. The two-photon detuning, δ, is swept through the two-photon resonance, i.e. the energy separation of $|-1_g\rangle$ and $|+1_g\rangle$, the two lower levels of the Λ system.

First discovered in 1978, CPT is a dissipative interaction that is commonly seen through spectroscopic measurements. The absorption or photoluminescence (PL) of a medium is observed in the presence of two optical pumps. The separation in frequency between these pumps is swept result-

ing in a dip in the measured absorption or PL at the two-photon resonance, in Fig. 1.6. As a spectroscopic measurement, this has been observed in a number of systems including a wide variety of atomic systems [12, 13], NV centers in diamond [15, 16, 17], quantum dots [18], superconducting qubits [19], and optomechanical resonantors [20]. In Ch. 3, we explore this phenomenon in an individual NV center in diamond using time-resolved tomography techniques.

1.5.3 Stimulated Raman transitions (SRT)

When the optical driving fields in a Λ system are sufficiently detuned, an AC Stark effect is present, and this effect is also referred to as stimulated Raman transitions (SRT). One way to think about this is to reimagine the ground state levels of our Λ system. Rather than the standard levels, $|\alpha\rangle$ and $|\beta\rangle$, we can redefine the lower level basis to include the dark state, $|D\rangle$ and an orthogonal superposition, or "bright" state $|B\rangle$[1]. Both $|D\rangle$ and $|B\rangle$ span the ground state subspace, and exist at two orthogonal points on the $|\alpha\rangle$ / $|\beta\rangle$ rotating frame Bloch sphere (Fig. 1.7). The two pumps now appear as a single pump on $|B\rangle \rightarrow |\varepsilon\rangle$. As described in §1.4.3, we now see the dressed versions of $|B\rangle$ and $|\varepsilon\rangle$ split in energy by $\hbar\sqrt{\Delta^2 + \Omega^2}$.

[1]Note that this bright state is technically not a bright eigenstate of the system. Those typically refer to the other two solutions of the Hamiltonian that yield superpositions that include all three levels; however, this bright state is the superposition of the two bright eigenstates that eliminates the excited state.

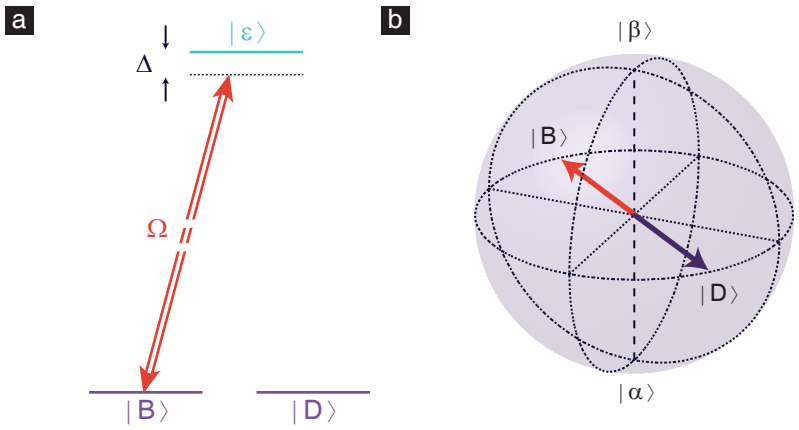

Figure 1.7: Dark / bright basis a) Λ system recast in basis of the ground-state orthogonal superpositions, the dark state, $|D\rangle$, and bright state, $|B\rangle$. The two driving fields are also recast as a single optical pump on the $|B\rangle \rightarrow |\varepsilon\rangle$ transition. **b)** An example $|D\rangle$ and $|B\rangle$ basis in relation to the original $|\alpha\rangle$ and $|\beta\rangle$ basis rotating frame Bloch sphere.

This splitting also shifts $|B\rangle$ relative to $|D\rangle$ and manifests as precession about the energy imbalance for any superposition of $|B\rangle$ and $|D\rangle$. Because $|D\rangle$, and as a result $|B\rangle$, are selectable superpositions based on the optical driving fields, we can define any axis of rotation within the $|\alpha\rangle$ / $|\beta\rangle$ Bloch sphere. Such single qubit rotations were first seen in trapped ion systems [21]. In Ch. 3, we describe how we apply these rotations to NV centers in diamond.

1.5.4 Stimulated Raman adiabatic passage (STIRAP)

Another technique used in Λ systems, known as stimulated Raman adiabatic passage, or STIRAP, is for highly efficient population transfer be-

tween levels. The idea behind STIRAP is that by shifting how the system is driven over time, the dark state defined by the system also changes. If the shift in the pumps is slow enough relative to the energetics of the system, or adiabatic, the dark state will move along the Bloch sphere without excitation through the potentially lossy excited state $|\varepsilon\rangle$. Adiabaticity is defined by the rate of change of the Hamiltonian relative to the energy scales involved. If evolution of the Hamiltonian is defined by some frequency, ω_A, then $\hbar\omega_A \ll E_g$, where E_g is the characteristic energy spacing of eigenstates defined by the Hamiltonian. Such techniques are commonly used in atomic physics to transfer population within a subspace without loss out of that subspace [14], and have recently been demonstrated in the solid state [22, 23]. In Ch. 4, we explore STIRAP within the NV center for another purpose, the enclosure of a quantum geometric phase known as Berry phase.

1.6 Light-matter interactions within the NV Center

With this review of light-matter interactions that can be used to control individual quantum systems, we now focus on our particular quantum system that shows promise as a qubit and nanoscale sensor. The negatively charged nitrogen-vacancy (NV) center consists of a substitutional nitrogen adjacent to a vacancy within the carbon lattice of diamond (Fig. 1.1).

An ensemble of these defects was first seen spectroscopically as an emission band consisting of a zero-phonon line at 637 nm and a red-shifted phonon sideband that extends out to 800 nm [24]. In 1997, individual nitrogen-vacancy centers were first isolated, and optically detected magnetic resonance of its spin triplet ground state was observed [25]. Since then, research on this defect has been quite a fruitful endeavor [26]. The level structure of the NV center plays a key role in motivating its use as a spin qubit and nanoscale sensor.

1.6.1 The NV center level structure

At the defect site, the three carbon dangling bonds around the vacancy provide an electron each, while the nitrogen dangling bond provides two electrons. If an extra electron is trapped within the site, these six electrons form the negatively charged NV center. The level structure of the NV center (Fig. 1.8) is understood through its symmetry point group, C_{3v} [27, 28], and consists of a ground state spin triplet, $^3A_2$ and an excited state orbital doublet, spin triplet, ^3E. These levels are separated by a 1.945 eV (637 nm), the zero-phonon line, within the 5.5 eV bandgap of diamond. In addition, the NV center contains long-lived spin singlet levels A_1 and E_1 separated by 1.190 eV (1042 nm) which are accessed via an intersystem crossing.

The NV center has distinct phonon-assisted emission and absorption

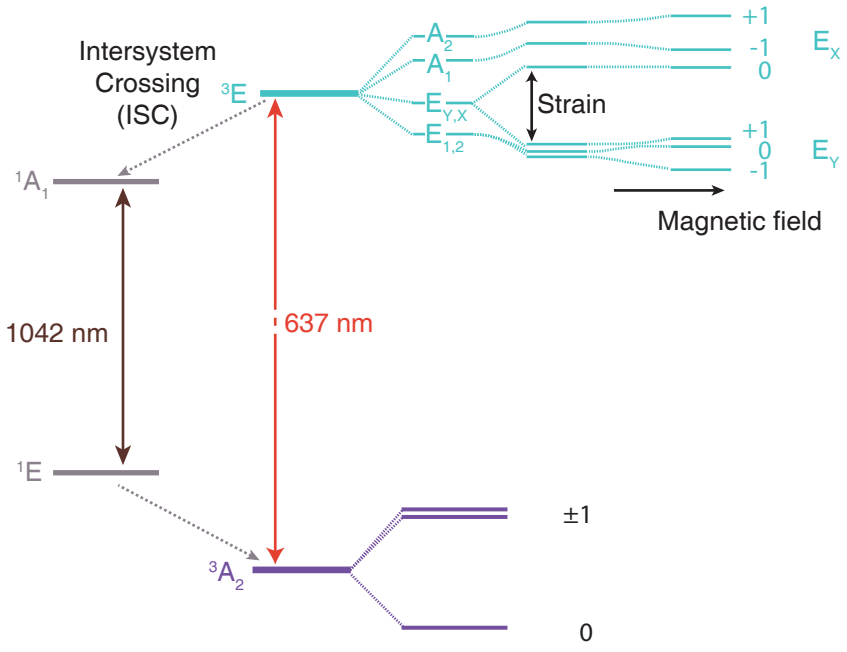

Figure 1.8: NV center level structure A schematic of the NV^- level structure, consisting of a ground state spin triplet, $^3A_2$ (purple), coupled to an excited state spin-triplet, orbital-doublet, ^3E (teal). These levels are separated by 1.945 eV (637 nm). Two spin singlet levels, $^1A_1$ and ^1E (grey), are accessed via an intersystem crossing, and are separated from each other by 1.190 eV (1042 nm). At zero-field (electric and magnetic), the excited state, ^3E (teal), consists of six spin-orbit levels A_2, A_1, degenerate levels E_X and E_Y, and degenerate levels E_1 and E_2 (left). The separation of these levels is determined by spin-spin and spin-orbit interactions. Inherent crystal strain and/or applied electric fields will split these levels into distinct orbital branches, E_X and E_Y (middle). An applied magnetic field will further split and resolve the spin sublevels of each orbital branch (right). The cartoon, while not exact, shows an approximately 10 GHz strain splitting, and magnetic field tuning out to 600 G. (In this graphic, the scale of the excited state manifold is such that 1 mm corresponds to 1 GHz of energy separation).

bands. The absorption band lies at the zero-phonon line (637 nm) and higher energies (extending out to 450 nm), while the emission band lies at the zero-phonon line and lower energies (extending out to 850 nm) (Fig.

1.9). This emission is largely within the phonon-shifted sideband with only 3% of the emission occurring in the zero-phonon line. Typically, the NV center is excited with 532 nm laser light (which lies within the NV center absorption band) in a confocal microscopy setup, and the NV center red-shifted emission, or photoluminescence (PL), is then collected by a silicon avalanche photodiode (see Appendix A).

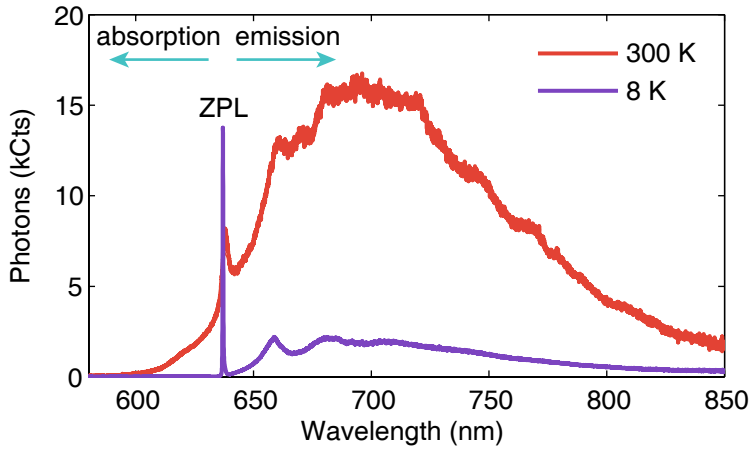

Figure 1.9: NV center emission spectrum The emission band of an ensemble of NV centers taken at both room temperature (300 K) and cryogenic temperature (8 K). The distinct zero-phonon line (ZPL) is seen at 637 nm, and the phonon-assisted sideband extends out to 850 nm. A reduction in the phonon-sideband is seen at $T = 8$ K. Like the shown emission band, a similarly shaped absorption spectrum can be found at 637 nm with a phonon-assisted absorption band at higher energies ($400 - 600$ nm). Spectrum courtesy of B. B. Buckley and F. J. Heremans.

This level structure permits spin-dependent optical readout and initialization, as different spin sublevels of the NV center excited states (^3E) couple with different strengths to the singlet level A_1 via the intersystem crossing. In general, the excited state $m_S = \pm 1$ sublevels couple more

strongly and can decay to the ground state through this "non-radiative" path (i.e. it emits radiation further into the infrared, beyond our collection range). In this manner, if we excite the NV center and cycle it between the ground and excited states, a spin beginning in $m_S = 0$ will emit more light into the phonon sideband than a spin beginning in either $m_S = \pm 1$ as those states will eventually pass through the intersystem crossing "shelving" in the long-lived singlets and not emitting photons in the collected phonon sideband, leading to a spin-dependent optical readout with contrasts as high as 40%.

This structure also enables initialization, as states that preferentially decay into the singlet states decay out of the singlets without preference. After several optical cycles, the spin is thus polarized into $m_S = 0$ with $\sim 80\%$ fidelity. As such, this structure for readout and initialization of spin states provides an excellent platform to enable many of the advances demonstrated with NV centers. In addition, this particular structure provides a framework for investigating other potential defects of interest [29], and recently, the divacancy in SiC has been identified as a similar defect in a more technologically mature material [30, 31, 32].

At zero magnetic field, the ground state spin sublevels of the NV center are split by a crystal field splitting, $D \approx 2.87$ GHz. These spin sublevels can be further split by a magnetic field through Zeeman tuning. They also couple to nearby nuclear spins, such as the one intrinsic to the nitrogen

as well as nearby carbon-13 atoms). This ground state is described by the Hamiltonian:

$$H = DS_Z^2 + g\mu_B BS_Z + AS \cdot I \tag{1.38}$$

where S is the electronic spin operator, S_Z is its z-component, $\mu_B = 9.27 \times 10^{-24} J/T$ is the Bohr magneton, $g = 2$ is the electron g factor, A is the hyperfine constant, and I is the nuclear spin operator. The spin of the ground state is typically read out and initialized through the intersystem crossing mechanism described above, while manipulation of this spin state is accomplished through Rabi oscillations using microwave fields tuned to the transitions between spin sublevels ($\omega_{mw} = (D \pm g\mu_B B)/\hbar$) of $\Delta m_S = 1$.

The excited state level structure is more complex consisting of six spin-orbit levels at zero magnetic and electric field. These orbital components can be tuned through DC Stark effect either through intrinsic strain within the crystal or an external electric field. Likewise, its spin components can be tuned through the Zeeman effect with an external magnetic field. At high magnetic and electric fields, these levels split into an orbital doublet, ${}^3E_Y$ and ${}^3E_X$, with each orbital containing a spin triplet. A more detailed treatment of the excited state can be found in [26, 27, 28, 33, 34], but relevant points will be discussed here. The spin-orbit levels are labelled by their symmetry $\{|E_2\rangle, |E_1\rangle, |E_Y\rangle, |E_X\rangle, |A_1\rangle, |A_2\rangle\}$, and when sufficiently split by electric and magnetic fields they evolve into the two orbitals with their spin sublevels, $\{|E_Y, -1\rangle, |E_Y, 0\rangle, |E_Y, +1\rangle, |E_X, 0\rangle, |E_X, -1\rangle, |E_X, +1\rangle\}$

roughly ordered energetically (specific details of the magnetic and electric field determine the final energetic ordering).

At sufficiently high strain, transitions to the excited state correspond to different dipole moments, resulting in polarization selectivity between the two orbitals. This detailed structure of the excited state is only optically resolvable at cryogenic temperatures ($T < 20\,\mathrm{K}$) [33], above which Jahn-Teller distortions cause significant broadening of these levels [35]. The room temperature operation of the NV center is enabled by a phenomenon known as motional broadening, leading to an orbital singlet-like excited state with a spin triplet [36]. However, all experiments described in this thesis are done at cryogenic temperatures to exploit the excited state optical transitions.

To resolve these levels at cryogenic temperatures, we use a tunable 637 nm laser to scan across the various transitions between the ground and excited states, measuring the emitted PL. Peaks appear when the laser is on resonance with such a transition, in a measurement known as photoluminescence excitation (PLE) (Fig. 1.10). Broadening of these peaks can be due to laser power broadening but also to spectral diffusion. Charge instabilities around the NV center can reset during certain types of photoexcitation, causing a slightly different electric field to be seen by the NV center resulting in shifts of the transition energies. Over a series of measurements with repeated re-initializations by a 532 nm laser, this leads

to a spectrally-broadened peak [35].

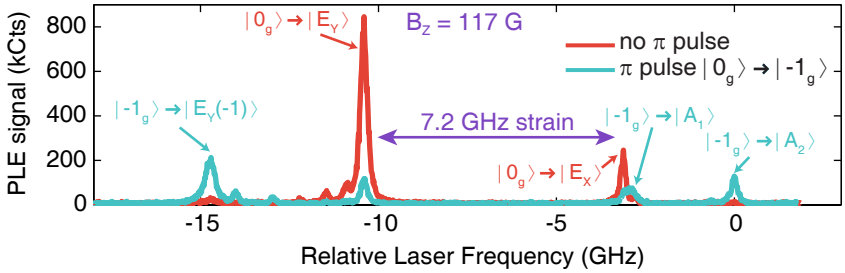

Figure 1.10: Photoluminescence excitation (PLE) measurement An example photoluminescence excitation (PLE) measurement for a single NV center in electronic grade diamond. This NV center had a strain splitting of 7.2 GHz and an applied magnetic field of 117 G along the NV center axis. Transitions between the ground and excited states are resolved by tuning the frequency of the driving laser. Transitions between the $m_S = 0$ ground state and the excited states are shown in red, while transitions between the $m_S = -1$ ground state and the excited states are shown in teal. The levels, E_Y, E_X, A_1, and A_2 are easily resolvable.

1.6.2 The NV center as a solid-state quantum optical testbed

Due to the rich structure of the NV center excited state and its optical addressability, the NV center has become an excellent testbed for a number of quantum optical protocols aimed at the development of photonic networks and quantum repeaters for quantum information processing [37]. Rather than relying on the off-resonant excitation provided by 532 nm and the intersystem crossing to initialize and readout the spin, specific spin-dependent transitions can instead be resonantly excited. Significant im-

provements in readout fidelity can be realized through resonant excitation along spin-dependent transitions coupled with a solid immersion lens to enhance the collection efficiency of the emitted PL, leading to single-shot readout [38]. Likewise, by optically pumping the spin from one spinstate to another, it is possible to initialize the spin state of the NV center with 99.7% fidelity [38]. In addition, resonant excitation allows for the observation of optical Rabi oscillations between the ground and excited spin states, providing a way to fully populate the excited state of the NV center [39].

In addition, the NV center was used in one of the first demonstrations of spin-photon entanglement in the solid state, as the $|A_2\rangle$ excited state couples to two ground spin states through different circular polarizations of light, such that the polarization of the emitted photon is entangled with the spin state [40]. Likewise, a photon absorbed by the NV center through excitation to this $|A_2\rangle$ excited state may also becomes entangled with the spin state [41]. The coherences between the spin and photons can be probed through the Faraday effect, a non-destructive measurement of the spin state based on light polarizations [42]. By expanding similar protocols to include two NV centers, interference between an emitted zero-phonon line photon from each has been demonstrated [43, 44]. However, every NV center has slightly different orbital transition energies due to the local electrostatic environment. The DC Stark effect is a method that allows

us to tune transitions from separate NV centers to degeneracy needed for two-photon intereference and is explored in Ch. 2 of this thesis [45].

Many of these developments laid the foundation for the demonstration of photonic entanglement of two NV centers separated by 3 meters [46]. Combined with efforts in developing nuclear spin registries, this was further expanded to photonically teleport the nuclear spin state of one NV center onto the electronic spin state of another NV center [47]. Tests of quantum mechanics have also been demonstrated with NV centers using these techniques, including the three-quantum box problem [48], as a loophole-free test of Bell's inequality [49].

Additionally, the development of photonic crystals and cavities in diamond to couple to individual NV centers is an important research focus. Such developments aim to improve the optical interface to the NV center, as only 3% of the emission is in the zero-phonon line due to strong phonon coupling. While diamond is a challenging material to fabricate, numerous structures have been implemented recently [50], including microring resonators [51], photonic crystals [52], nanowires [53], and nanobeams [54].

Another route to investigate the NV center quantum optical interface is to develop methods to actively and fully control the spin with light, a research path of particular focus for our group. Such control occurs within a smaller footprint than previous microwave techniques, down to the spot size of a diffraction-limited laser, enabling integration into photonic networks

or spin arrays. Additionally, these types of techniques should be adaptable to a variety of different solid-state systems. In the NV center, the AC Stark effect provides a way of rotating the NV center ground-state spin about the energy eigenbasis axis (a Z-axis rotation on the Bloch sphere) [42]. In this thesis, I will describe several experiments looking further into fully controlling the spin state of the NV center with light. Harnessing Λ systems in the NV center provide a way to develop complete control over the spin using just light. In Ch.3, we demonstrate a method to initialize, rotate, and readout the NV center spin within any arbitrarily chosen dark state basis [55]. In Ch. 4, we extend this technique to adiabatically evolve the dark state enclosing loops in the Bloch sphere parameter space, accumulating a quantum phase that is dependent only on the geometry of the path, not the energetics of the interaction [56]. In Ch. 5, we develop an alternative procedure to optically control the spin by harnessing evolution within the excited state [34].

These advances push toward the development of a photonic network of defects linked and controlled by light for the purposes of quantum information processing. They also act as a series of protocols that can be implemented in a variety of solid-state qubits, including other color centers, transition metal or rare-earth ions, as well as quantum dots.

1.6.3 The organization of this thesis

The following chapters describe our efforts in using the NV center as a quantum optical testbed to develop techniques to facilitate the development of solid-state photonic networks. Ch. 2 describes our efforts to tune NV center optical transitions to degeneracy aided by a photoinduced rectified electric field. Chapters 3-5 describe approaches to all-optically control the NV center spin state. Chapters 3 and 4 in particular focus on Λ system interactions that control the spin dissipatively (CPT), dispersively (SRT), and geometrically (STIRAP). Chapter 5 provides an alternative approach that relies on probing the excited state spin dynamics. The thesis then follows with a conclusion and outlook in Chapter 6, and a series of appendices describing the confocal microscopy setups used to study NV centers (Appendix A), as well as supplemental and supporting data for the experiments presented in Chapter 3 (Appendix B), and Chapter 4 (Appendix C) and a brief discussion on a few unanswered questions encountered during some of these experiments (Appendix D).

Chapter 2

Photo-enhanced electrical tuning of NV center orbital transitions

The following chapter is adapted from previously published work [45], and was a joint effort between our two cryogenic confocal experimental setups, which I worked on with Lee Bassett, F. Joseph Heremans, and Bob Buckley. Further details from this experiment can be found in F. J. Heremans' thesis [57], and the supplementary material for Ref. [45] available online.

2.1 Introduction

As solid-state 'trapped atoms,' NV centers are sensitive to their local environment. While this sensitivity has enabled nanoscale magnetic [58, 59, 60] and electric [61] metrology, it also exposes individual NV centers to sample inhomogeneities, leading to a distribution of zero-phonon line (ZPL)

frequencies within a diamond [33]. The ability to tune these frequencies is crucial for photonic applications, for instance to utilize the selection rules at the C_{3v} symmetry point for spin-photon entanglement [40] or to coherently couple distant NV centers to indistinguishable photons. Through the DC Stark effect, applied electric fields perturb both the ground-state spin [61, 62] and excited-state orbitals [63, 64], providing the means to control the optical transitions.

2.2 Tuning orbitals with the DC Stark effect

2.2.1 Experimental setup

Here we use micron-scale devices to manipulate electric fields in three dimensions, to compensate the intrinsic local strain and electrostatic fields of individual NV centers and achieve full control of the orbital Hamiltonian. Furthermore, by analyzing the Stark shifts as a function of applied voltages, we infer a surprising amplification and rectification of the local electric field, consistent with electrostatic contributions from photoionized charge traps within the diamond. By harnessing this reproducible effect, we can tune the NV-center Hamiltonian to arbitrary points across a range comparable to the inhomogeneous ZPL distribution.

The electronic structure of the negatively-charged NV center is deter-

mined by symmetry, through its point group C_{3v} [33, 27, 28]. The spin-triplet ground (GS, symmetry $^3\mathrm{A}_2$) and excited states (ES, symmetry $^3\mathrm{E}$), are connected by ZPL transitions around 637.2 nm (1.946 eV). Our experiments are performed at zero magnetic field, where the spin-triplet basis states are $\{|S_x\rangle, |S_y\rangle, |S_z\rangle\}$. A 532 nm (2.3 eV) 'repump' beam pulsed at ≈300 kHz in a confocal geometry maintains a spin-polarized population in $|S_z\rangle$. Between repump cycles, we count photoluminescence excitation (PLE) photons emitted by the NV center into the red-shifted phonon sideband (see Fig. 2.1a) after absorption from a narrow-line red laser tunable across the ZPL transitions. As we scan the red laser frequency, we typically measure two peaks in the PLE spectrum as shown in Fig. 2.1b; these correspond to spin-conserving transitions from the GS orbital singlet $|\mathrm{A}_2, S_z\rangle$ to the two ES orbital eigenstates $\{|\mathrm{E}_1, S_z\rangle, |\mathrm{E}_2, S_z\rangle\}$. In a crystal environment with perfect C_{3v} symmetry and zero electric and magnetic fields these ES orbital states would be degenerate, but the symmetry is generally broken by local crystal strain and by nonuniform electrostatic charge distributions that generate local electric fields.

2.2.2 The DC Stark perturbation on the NV center orbitals

The DC Stark perturbation to the Hamiltonian, $\hat{H}_{\mathrm{Stark}} = -\hat{\boldsymbol{\mu}} \cdot \mathbf{F}$, describes the interaction between the local electric field $\mathbf{F}$ and the electric dipole op-

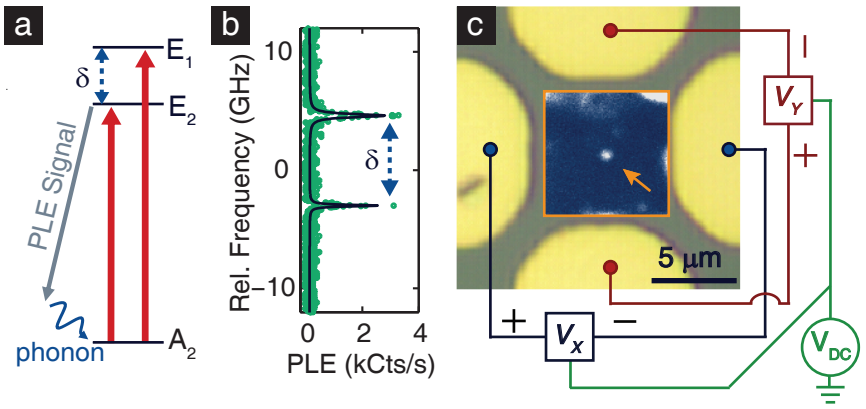

Figure 2.1: Implementing electric field control a) Simplified energy-level diagram (not to scale) showing only the $|S_z\rangle$ levels of the NV-center ground and excited states, with resonant excitation (red arrows) and red-shifted emission (gray arrow) marked. **b)** PLE spectrum (points) with no applied bias, marked by dashed line in Fig. 2.2, with a two-Lorentzian fit (solid curve). **c)** Micrograph and photoluminescence image (center) of device A, with electrical connections marked.

erator $\hat{\boldsymbol{\mu}}$. For fixed stress, the strain perturbation can be cast into the same form by isolating components which transform as the irreducible representations of C_{3v} [27, 28]. The combined perturbation has the form $V_{\mathrm{A}_1}\hat{O}_{\mathrm{A}_1} + V_{\mathrm{E}_x}\hat{O}_{\mathrm{E}_x} + V_{\mathrm{E}_y}\hat{O}_{\mathrm{E}_y}$, where $\hat{O}_{\Gamma_a}$ is an orbital operator transforming as the basis state $|\Gamma_a\rangle$ and

$$\begin{cases} V_{\mathrm{A}_1} = S_{\mathrm{A}_1} - \mu_{\parallel} F_z \\ V_{\mathrm{E}_x} = S_{\mathrm{E}_x} - \mu_{\perp} F_x \\ V_{\mathrm{E}_y} = S_{\mathrm{E}_y} - \mu_{\perp} F_y \end{cases} \tag{2.1}$$

are the symmetrized field strengths, in terms of fixed strain components S_{Γ_a}, projections of the local electric field F_i, and the reduced matrix elements of the electric dipole operator $\{\mu_{\parallel}, \mu_{\perp}\}$. We choose orbital basis

states $\{|\mathrm{E}_x\rangle, |\mathrm{E}_y\rangle\}$ for the ES which transform like vectors $\{x, y\}$ in the NV-center coordinate system [1], and we ignore the small (≈100 MHz) spin-spin coupling between ES spin states $|S_z\rangle$ and $\{|S_x\rangle, |S_y\rangle\}$ [2]. By defining $\hat{H}\,|\mathrm{A}_2, S_z\rangle \equiv 0$, the Hamiltonian in the $\{|\mathrm{E}_x, S_z\rangle, |\mathrm{E}_y, S_z\rangle\}$ basis can be written as

$$H = (\hbar\omega_0 + \Delta\mu_\parallel F_z)\mathbf{I} + \frac{1}{\sqrt{2}} \begin{pmatrix} V_{\mathrm{E}_x} & -V_{\mathrm{E}_y} \\ -V_{\mathrm{E}_y} & -V_{\mathrm{E}_x} \end{pmatrix}, \tag{2.2}$$

where $\hbar\omega_0$ is the natural transition energy including fixed perturbations of A_1 symmetry, and $\Delta\mu_\parallel = \left(\mu_\parallel^{\mathrm{GS}} - \mu_\parallel^{\mathrm{ES}}\right)$, defined such that both $\Delta\mu_\parallel$ and $\mu_\perp$ are positive. The transition energy eigenvalues take the form $E_\pm = h\bar{\nu} \pm \frac{1}{2}h\delta$, where

$$h\bar{\nu} = \hbar\omega_0 + \Delta\mu_\parallel F_z, \tag{2.3a}$$

$$h\delta = \sqrt{2}\left(V_{\mathrm{E}_x}^2 + V_{\mathrm{E}_y}^2\right)^{1/2} \tag{2.3b}$$

are the longitudinal and transverse components due to fields of A_1 and E symmetry, respectively. From Eq. 2.1, it is clear that a local electric field can cancel the transverse components of intrinsic strain to restore C_{3v} symmetry to the system, and from Eq. 2.3a we see that an electric field

[1] The NV-center coordinate system is chosen such that $\hat{z}$ points along the N-V symmetry axis and $\hat{x}$ lies in a reflection plane.

[2] Note that while spin-spin coupling leads to mixed ES spin eigenstates in some regimes, it does not significantly affect the optical pumping mechanism which polarizes the spin into $|S_z\rangle$ in our experiments.

F_z applied along the NV-center symmetry axis shifts the energy of both transitions by the same amount.

2.2.3 Lateral electric fields

We first investigate these effects using device A, shown in Fig. 2.1c, consisting of four Ti/Pt/Au gates fabricated on the diamond surface. The sample is a 0.5 mm-thick single-crystal diamond grown by chemical vapor deposition with <5 ppb nitrogen content (ElementSix), irradiated with 2 MeV electrons (1.2×10^{14} cm^{-2}) and then annealed at 800 °C to create NV centers. Measurements are performed in a continuous-flow cryostat operating at ≈20 K. Symmetric biases V_X and V_Y applied as shown in Fig. 2.1c produce 'lateral' electric fields F_X and F_Y in the [110] and [$\bar{1}$10] crystal directions, respectively, while a common DC bias generates fields in the [001] out-of-plane (Z) direction. The sample (X, Y, Z) and NV-center (x, y, z) coordinate systems are uniquely related for a given NV-center projection from the $\langle 111 \rangle$ family [Supplemental of Ref. [45]].

Figure 2.2 contains a series of PLE spectra showing the optical resonances of the NV center marked in Fig. 2.1c, as a function of separate biases V_X and V_Y with $V_{\mathrm{DC}} = 0$ V. The lateral biases are applied as symmetrically-pulsed square waves at 1 kHz, with PLE photons binned according to polarity. While the response to static lateral bias is qualitatively similar, this technique separates slow photoinduced charging effects from

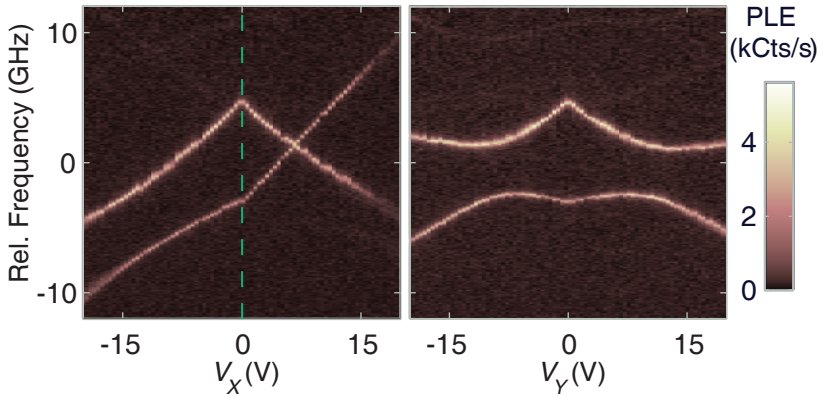

Figure 2.2: DC Stark shifts of orbital transitions PLE spectra of the 6 µm-deep NV center marked by an arrow in Fig. 2.1c as a function of lateral bias applied symmetrically to the X (left panel) or Y (right panel) gate pairs, with $V_{\mathrm{DC}} = 0\,\mathrm{V}$. In all PLE spectra, the origin of the relative frequency axis is arbitrary.

the dielectric response as discussed later in this chapter. Two features are evident in the data: first, we observe an unexpected 'kink' at zero bias, and second, the resonances cross at $V_X \approx 7\,\mathrm{V}$, demonstrating that we can indeed restore C_{3v} symmetry to the system. We explore both of these features with additional experiments.

2.3 The photo-induced electric field

2.3.1 Photoionization of charge traps

The kink at zero bias reflects an asymmetry in the local electric field vector as a function of polarity, i.e., $\mathbf{F}(+V) \neq -\mathbf{F}(-V)$. We argue that this asymmetry results from the photoionization of charge traps in the diamond host. Even in high-quality single-crystal synthetic diamonds, deep defects such

as vacancy complexes and substitutional nitrogen have important effects on the material's electronic properties [65]. In particular, substitutional nitrogen atoms form donor levels ≈1.7–2.2 eV below the conduction band edge [66, 67], and the timescale for charge transport through these levels is very long (on the order of hours) even in nitrogen-rich diamond at room temperature [68]. These traps are easily ionized by the 532 nm repump beam (≈100 μW) which is 4–5 orders of magnitude stronger than the red laser (≈1 nW). When voltages are applied, this leads to a long-lived non-equilibrium charge distribution in the illuminated volume of the sample, which can either amplify or screen the local electric field.

2.3.2 Vertical electric fields

As a simplified one-dimensional demonstration, we present in Fig. 2.3a the Stark-shift response of an NV center 13 μm below the surface of a second diamond sample irradiated and annealed under similar conditions, but patterned with a global top gate of the transparent conductor indium-tin-oxide (device B). As the top-gate bias is stepped in a loop over ≈160 min, we observe hysteresis in the response characteristic of ≈1 h charge-relaxation timescales. Furthermore, by comparing the magnitudes of the Stark shifts due to biases applied laterally across an 8 μm gap (Fig. 2.2) and vertically across the 0.5 mm sample thickness (Fig. 2.3a), we find that, when the top-gate bias is negative, the local electric field below the top gate appears

to be amplified by roughly an order of magnitude over dielectric predictions [Supplemental of Ref. [45]]; conversely, the field appears to be completely screened above a 'threshold bias,' where the response is flat. The response of an NV center in device A to variations of V_{DC} is qualitatively similar [Supplemental of Ref. [45]], and both are consistent with a picture in which positive charges in the illuminated volume below the NV center rectify the Z-component of the electric field.

2.3.3 Rectified component of the electric field

We can incorporate these charging effects into a phenomenological model capturing the essential features of our observations. As depicted in Fig. 2.3b, the local electric field for an NV center between two surface gates is composed of a dielectric component roughly parallel to the sample surface and a rectified component due to photoionized charge that is mainly out of plane. We model this field as

$$\mathbf{F} = \beta V \hat{\mathbf{v}} + \beta |V| \boldsymbol{\xi}, \tag{2.4}$$

where β accounts for geometric and dielectric factors that predict a local electric field in the direction $\hat{\mathbf{v}}$ in response to an applied voltage V, and $\boldsymbol{\xi}$ is a dimensionless vector giving the relative strength and direction of the rectified field, assumed to scale linearly with $|V|$. Due to the long charging timescale, the rectified field $\beta|V|\boldsymbol{\xi}$ does not change when we switch the bias polarity on millisecond timescales while the dielectric component

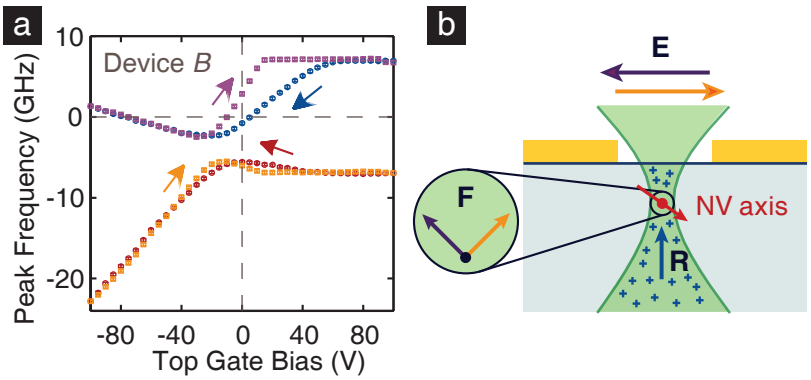

Figure 2.3: Rectifying photo-induced field a) Stark shift hysteresis loop for an NV center 13 μm below a transparent top gate, as a function of top-gate voltage. Points mark the transition frequencies from a two-Lorentzian fit to a PLE spectrum at the corresponding voltage and color-coded arrows indicate the sweep direction. **b)** Schematic of the local electric fields in a lateral geometry. Photoionized charge traps in the illuminated volume contribute a rectified field **R** predominantly in the $+Z$ direction, which adds to the dielectric field **E** to shift the direction of the local field **F**. Marker sizes slightly exceed measurement uncertainties.

$\beta V\hat{\mathbf{v}}$ changes sign, producing a polarity-asymmetric response. The assumption of a linear relationship between the rectified field strength and $|V|$ is motivated by the empirical observation that $\bar{\nu}$, proportional to F_z, varies linearly with applied bias in all our measurements. This amounts to an approximation that the spatial distribution of photoionized charge remains fixed, while the charge density varies linearly with $|V|$.

Figure 2.4 shows the mean ($\bar{\nu}$) and difference (δ) of the transition frequencies extracted from fits to the PLE spectra in Fig. 2.2. The NV-center symmetry axis ($[11\bar{1}]$ in this case) is uniquely determined by the sign of $\bar{\nu}$ in response to electric fields in different directions. By substituting Eq. 2.4 into Eq. 2.3 and applying the appropriate coordinate transformation,

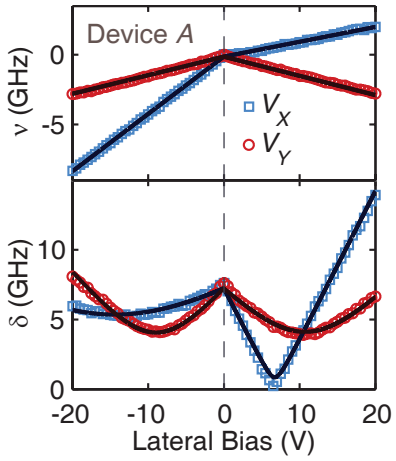

Figure 2.4: Phenomenological model for rectification DC Stark components $\bar{\nu}$ and δ (points) extracted from fits of the PLE spectra in Fig. 2.2, with a combined fit according to the model described in the text (solid curves).

we obtain a model that quantitatively agrees with our observations [Supplemental of Ref. [45]], as shown by the fits to the data in Fig. 2.4. Given that this is only a simplified phenomenological description of a complicated three-dimensional system, it matches our observations well.

2.3.4 Eliminating the photo-induced field

Finally, we present a control experiment in which we mitigate effects due to the 532 nm repump cycle. Occasional repump pulses are still required to compensate for photoionization of the NV^- charge state due to sequential two-photon absorption, but with weak (<1 nW) resonant light, the required repump period can be increased to several seconds [35], allowing time to apply bias, record a complete PLE spectrum, and re-zero the bias, all between repump pulses. Since weak spin-nonconserving optical

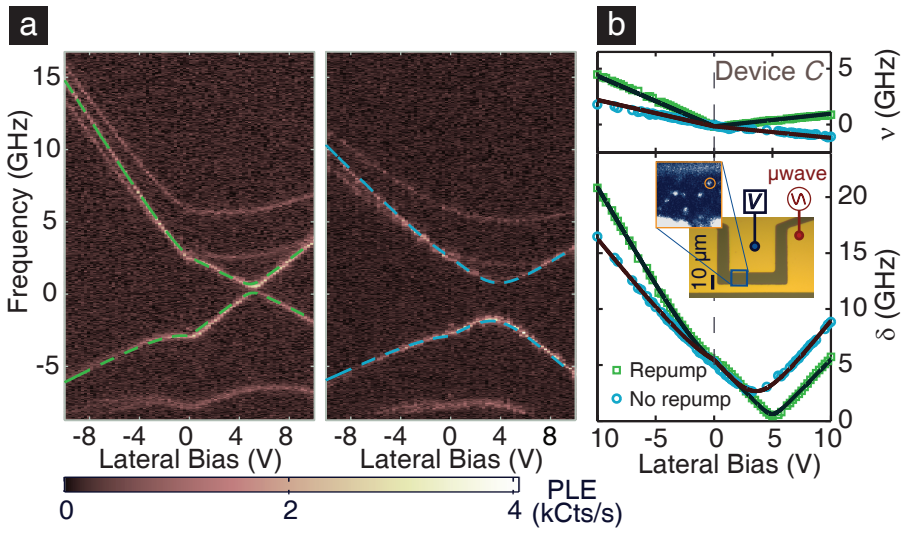

Figure 2.5: Eliminating the photo-induced field a) Orbital transitions as a function of gate voltage with (left) and without (right) 532 nm repump excitation. **b)** DC Stark components (points) and fits (solid curves) measured both with (green squares) and without (orange circles) the 532 nm repump excitation. Inset: Micrograph and photoluminescence image of device C, with electrical connections marked. The 7 μm-deep NV center measured in is circled. In all cases, marker sizes slightly exceed measurement uncertainties.

transitions quickly polarize the NV-center spin away from resonance in the absence of the repump cycle, we mix the spin population by applying a microwave magnetic field resonant with the GS spin transition. We use another device for this purpose (device C), shown in the inset of Fig. 2.5, which is fabricated on the same diamond as our four-gate lateral device. It consists of a short-terminated waveguide to generate microwave fields and serve as ground, and a gate that when biased produces lateral electric fields across an 8 μm gap.

For an NV center in device C, Fig. 2.5a shows the orbital transitions

as a function of gate voltage, while in Fig. 2.5b, the resulting $\bar{\nu}$ and δ are plotted. The NV center used is circled in the inset of Fig. 2.5b. Once again the bias polarity is switched at 1 kHz and the PLE photons are binned accordingly. A polarity asymmetry is clearly observed when the repump beam is present, particularly as a kink in $\bar{\nu}$, and it is significantly reduced when the biases are applied in the absence of the repump cycle. Fits to the data using our model [Supplemental of Ref. [45]] are shown as solid curves, from which we find that $|\boldsymbol{\xi}|$ is reduced from 0.71±0.02 with the standard repump cycle to 0.33±0.03 when the 532 nm beam is omitted.

2.4 Tuning NV centers to degeneracy

Based on this understanding, we can exploit the photoinduced charge to obtain greatly enhanced tunability in our four-gate geometry (device A). Since the rectified field points predominantly out of plane and has strength comparable to the dielectric component, we effectively obtain three-dimensional control of the local electric field vector. The application of a negative reference bias V_{DC} as shown in Fig. 2.1c increases the rectified component F_Z independently of (F_X, F_Y). As a demonstration of the flexibility of this technique, we present a tuning diagram in Fig. 2.6 in which we use (V_X, V_Y) to scan through the C_{3v} degeneracy point at different settings of V_{DC}.

Each crossing occurs at a different frequency, with the corresponding

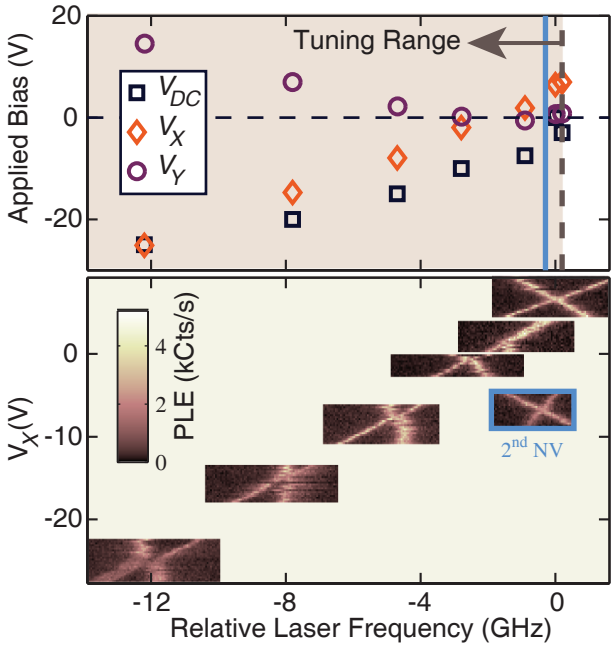

Figure 2.6: Tuning NV center orbital transitions to degeneracy Tuning diagram for the NV center marked in 2.1c. Degeneracy is achieved at different frequencies by setting the applied biases $(V_{\mathrm{DC}}, V_X, V_Y)$ as marked in the upper panel; in the lower panel we show PLE spectra as a function of V_X around each of these points for fixed V_{DC} (V_Y is also varied to keep the ratio V_X/V_Y constant). We can shift a second NV center to degeneracy within the tuning range of the first, as shown by the PLE spectra outlined in blue (lower panel) and the corresponding blue line (upper panel) marking the degenerate frequency.

bias point $(V_X, V_Y, V_{\mathrm{DC}})$ marked in the upper panel. Essentially, we are compensating the transverse components $(S_{\mathrm{E}_x}, S_{\mathrm{E}_y})$ of the intrinsic fields and tuning the longitudinal component of $\mathbf{F}$ to shift the frequency. Since the rectified field always points along $+Z$, we can only tune the frequency in one direction, but the effect is strong enough to produce a $>10\,\mathrm{GHz}$ shift in the degenerate frequency with practical applied voltages.

With this technique we can tune multiple NV centers to have the same

degenerate transition frequency. The PLE spectra outlined in blue in Fig. 2.6 were obtained from a second NV center in the same device at $V_{\mathrm{DC}} = 0$ V, and display C_{3v} degeneracy at a frequency within the tuning range of the first. If these two NV centers were in separately-controlled devices and tuned simultaneously to degeneracy at the same frequency, they would couple identically to indistinguishable photons.

In conclusion, we have used electric fields to tune the ZPL transitions of individual NV centers in micron-scale devices size-compatible with photonic structures. Through their DC Stark shifts, NV centers serve as nanoscale probes of their electrostatic environment, revealing strong signatures of charge accumulation due to photoionization of deep donor levels in the diamond. We have analyzed these effects with a phenomenological model and used the additional fields provided by photoionization to obtain three-dimensional control of the local electric field, in order to tune both the overall energy and orbital splitting of the excited-state Hamiltonian. In particular, we have demonstrated how to reach the C_{3v} symmetry point and then apply longitudinal perturbations to shift the degenerate photon energy. By coupling multiple NV centers to indistinguishable photons with this technique, photonic networks could provide a quantum bus to coherently couple distant NV centers, and entanglement swapping protocols [69, 70] could enable long-distance quantum key distribution.

Chapter 3

All-optical control of the NV center with coherent dark states

The following chapter is adapted from previously published work [55]. I worked on this experiment in close collaboration with Bob Buckley, along with theoretical assistance from Guido Burkard, and statistical analyses from David Christle. F. Joseph Heremans and Lee Bassett also provided valuable assistance in analysis and manuscript preparation. Further details from this experiment can be found in Appendix B.

3.1 Dark Resonances

To explore control of individual quantum states, our experiments exploit coherent dark resonances that occur in a basic quantum mechanical level configuration known as a lambda (Λ) system. This configuration, consist-

ing of two lower energy states coherently coupled to a single excited state, has been observed in a wide array of systems including atoms [12], trapped ions, diamond nitrogen-vacancy (NV) centers [15, 16], quantum dots [18], superconducting phase qubits [19], and optomechanical resonators [20]. In trapped ions, Λ systems can additionally be exploited to drive stimulated Raman transitions providing unitary rotations of the qubit state [71, 21]. This versatile structure also forms the framework for a variety of other important advances in quantum science such as electromagnetically induced transparency [72], slow light [73], atomic clocks [74], laser cooling [75], and spin-photon entanglement [40].

Here, we use time-resolved methods and quantum state tomography to explore the dynamics of various optically driven processes within a solid-state Λ system (Fig. 3.1a). This allows us to demonstrate three all-optical quantum control [21, 76, 77] protocols for a single NV center: initialization, unitary rotation, and readout of its spin state. Our Λ system consists of two ground state spin sublevels coupled to a spin-composite excited state sublevel formed by tuning the excited states to an avoided level crossing, or anticrossing. Driving transitions between the levels of our Λ system resonantly with appropriate coherent light fields (Fig. 3.1a) causes any initial mixed state to be purified [78], or trapped, into a well-defined but selectable quantum superposition. This superposition is called the "dark state" since destructive interference from the driving fields causes the system not to

be optically excited. This dissipative effect, known as coherent population trapping (CPT), allows us to initialize the precessing spin anywhere on the rotating-frame Bloch sphere, the geometric surface corresponding to all possible superposition states of the spin. Opposite the dark state on the Bloch sphere is a corresponding "bright state" which couples strongly to the optical fields. Together, these dark and bright states define a unique basis whose orientation within the rotating frame is a function of the relative phase and amplitude of the two driving optical fields (Fig. 3.1a). A complementary process allows us to read out the spin state within this selected basis because the resultant photoluminescence (PL) during the transient period of the CPT interaction is proportional to the spin's projection along the bright state. Furthermore, detuning the driving fields from resonance within the Λ system produces unitary rotations of the spin state about a chosen dark/bright-state axis, a dispersive technique that is a product of stimulated Raman transitions (SRT). Thus, this Λ system approach allows spin initialization, readout, and rotation schemes to all function within a fully mutable basis.

3.2 A Λ system in the NV center

We select the subspace spanned by two ground-state spin-triplet sublevels ($m_s = 0$ and $+1$) as our qubit states; the presence of the third sublevel ($m_s = -1$) causes only a small loss in fidelity (§B.4). We denote these

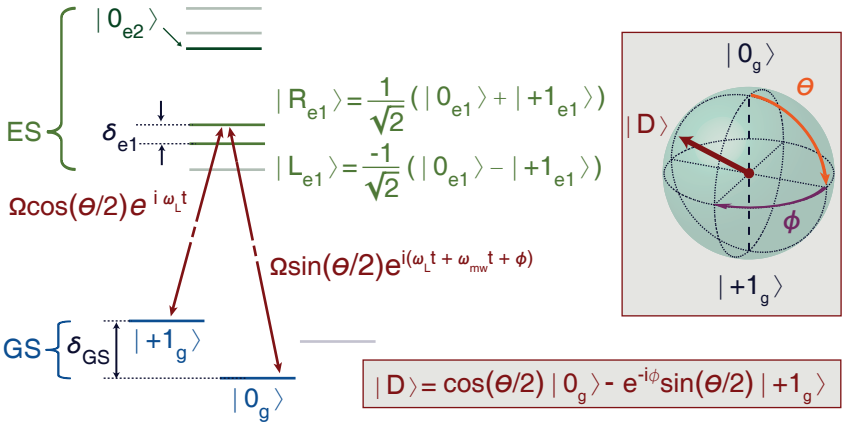

Figure 3.1: Λ configuration and the NV center, Λ configuration within the NV center level structure (left), depicting excitation with two optical driving fields from ground states (GS) to excited states (ES). At the center of the excited-state anticrossing, the two upper Λ states $|R_{e1}\rangle$ and $|L_{e1}\rangle$ (bolded green) are the orthogonal, equal superpositions of $|0_{e1}\rangle$ and $|+1_{e1}\rangle$. An example dark state, $|D\rangle$, from the $|R_{e1}\rangle$ Λ system, is plotted on the rotating-frame Bloch sphere (right), where its polar, θ, and azimuthal, ϕ, positions are a function of applied laser power and phase (equation).

states $|0_g\rangle$and $|+1_g\rangle$. To form the necessary excited state, we apply a magnetic field to reach a spin sublevel anticrossing, whose levels are a function of crystal strain, spin-spin, spin-orbit, and Zeeman interactions [27, 28] (§3.7.1). The anticrossing we use is between the $|0_{e1}\rangle$ and $|+1_{e1}\rangle$ spin sublevels within the lower-energy excited-state orbital branch[1] and results in two spin-composite levels (Fig. 3.2a) separated in energy by $\delta_{e1} \sim h{*}0.18\,\text{GHz}$. Either of these superposed levels, denoted $|R_{e1}\rangle$ and $|L_{e1}\rangle$, can act as the upper state of our Λ system (Fig. 3.1).

[1]In this chapter, we denote the lower branch of the excited state, E_Y, as "e1" and the upper branch, E_X, as "e2"

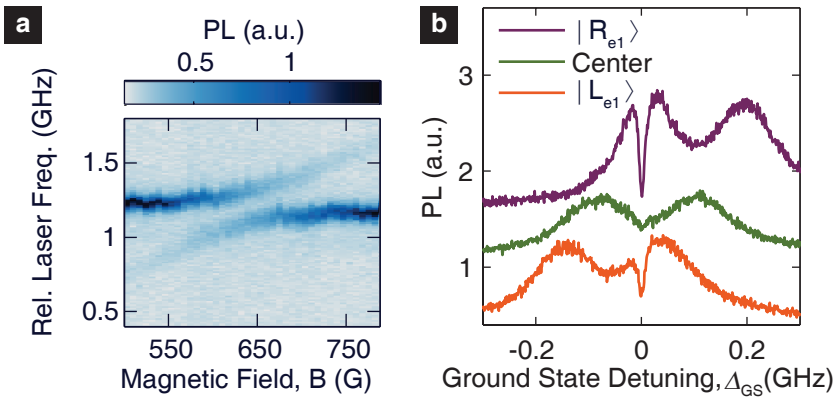

Figure 3.2: Excited state anticrossing a) PL from resonant excitation as a function of magnetic field and laser frequency illustrating the anticrossing between the $|0_{e1}\rangle$ and $|+1_{e1}\rangle$. **b)** PL from excitation with two optical fields as a function of the detuning of ω_{mw} from $\delta_{GS}/\hbar$, resonant with either $|R_{e1}\rangle$, $|L_{e1}\rangle$, or centered between both resonances.

In order to address the Λ-system transitions, we split light from a 637 nm ($\omega_L/(2\pi)$ ~470,000 GHz) laser tunable across the NV center's optical transitions into sidebands (multiples of $\omega_{mw}/(2\pi)$ ~4.6 GHz) with an electro-optic phase modulator. The relative phase (ϕ) between the two optical fields that are resonant with the Λ transitions determines the azimuthal position of the dark state on the Bloch sphere in the ω_{mw} rotating frame. Similarly, the relative amplitude of the two optical fields determines the dark state's polar angle, θ (Fig. 3.1). We first observe CPT spectroscopically [12, 15, 16, 17, 18, 19] by examining the PL under quasi-continuous photoexcitation that optically drives only one of the Λ systems. A sharp dip in PL is observed centered at $\omega_{mw} = \delta_{GS}/\hbar$ where δ_{GS} is the mean energy splitting between the spin eigenstates (Fig. 3.2b), indicating

that the spin is being coherently trapped in the dark state. Because the spin-composite excited states are orthogonal in the $|0_{e1}\rangle$ and $|+1_{e1}\rangle$ spin subspace, the dark states from each of the separate Λ systems have opposite azimuthal phases but the same polar position on the rotating-frame Bloch sphere for a given optical Λ-driving configuration. For this reason, when we tune the laser to equally excite both Λ systems ("center" curve in Fig. 3.2b), their competing dark states quench the PL dip. For subsequent studies, we set $\omega_{mw} = \delta_{GS}/\hbar$ unless otherwise noted.

3.3 Coherent population trapping for arbitrary-basis spin initialization

3.3.1 Tomographic reconstruction of coherent population trapping

We extend our investigation of the CPT interaction further by probing the time dynamics of the resultant spin state. We set the lasers resonant with the $|R_{e1}\rangle$ Λ system to produce a dark state near the Bloch sphere equator. After preparing the initial spin state in either $|0_g\rangle$ or $|+1_g\rangle$ with traditional off-resonant (532 nm laser) optical polarization and microwave electron-spin resonance (ESR) techniques [79], we engage the CPT interaction for a variable duration to polarize the spin toward the dark state. We then perform quantum state tomography (§3.7.3 and §B.2) by projecting the X,

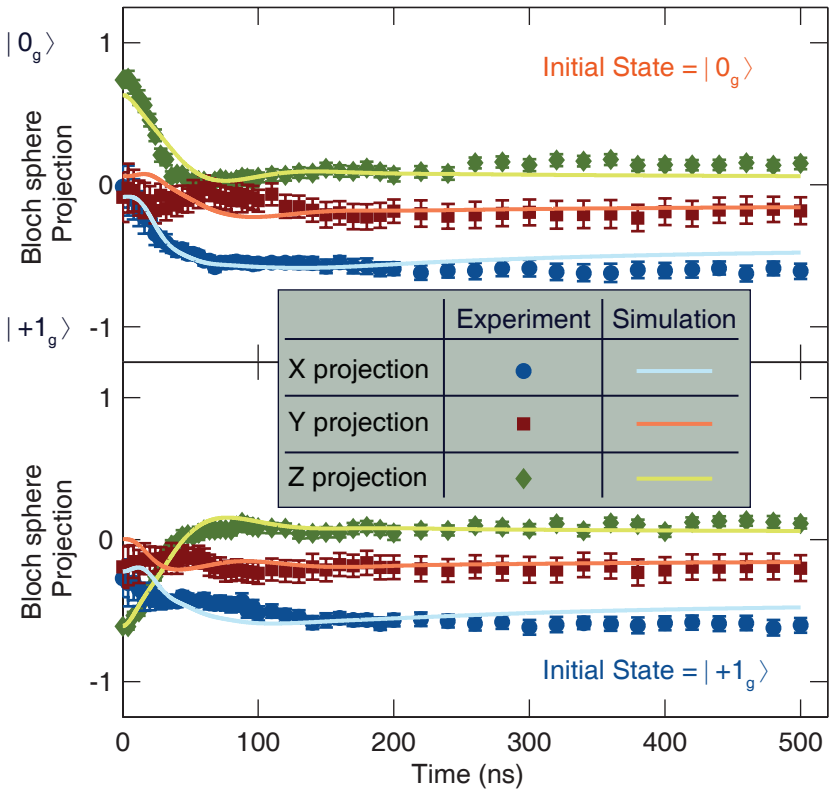

Figure 3.3: Quantum state tomography of coherent population trapping X, Y, and Z projections of the resultant spin state due to coherent population trapping as a function of interaction time for an initial state in $|0_g\rangle$ (top) and $|+1_g\rangle$ (bottom), plotted with a simulation of the time dynamics using a Lindblad master equation approach (see §3.7.4 and §B.3).

Y, and Z projections of the post-CPT spin state via microwave ESR pulses phase-matched to ω_{mw} onto the $|0_g\rangle/|+1_g\rangle$ measurement basis. Subsequent spin readout along this basis is accomplished via a second laser resonant with the $|0_g\rangle$ to $|0_{e2}\rangle$ cycling transition [38] (Fig. 3.1 and §3.7.2). These time-resolved projections are presented in Fig. 3.3, and are reconstructed on the Bloch sphere in Fig. 3.4a for both initial states.

The tomographic reconstructions (Fig. 3.4a) show that the spin state

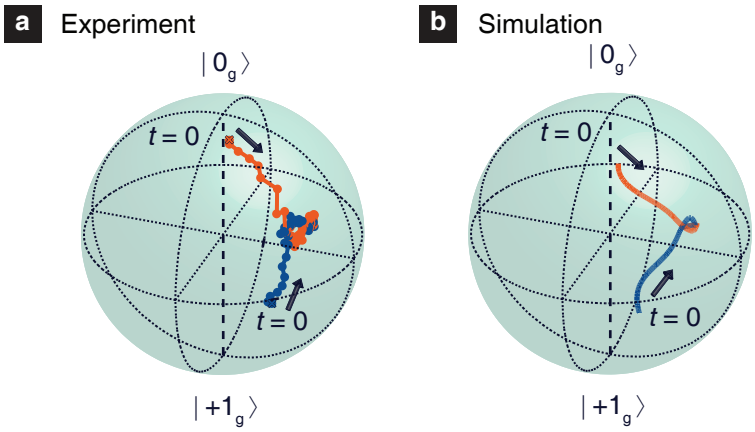

Figure 3.4: Time dynamics of coherent population trapping a) Bloch sphere representation of the spin state as a function of the CPT interaction time, on resonance with $|R_{e1}\rangle$. Beginning near either $|0_g\rangle$ (orange) or $|+1_g\rangle$ (blue), this process polarizes the spin towards $|D\rangle$ regardless of its initial state. Errors are ∼3x the point size, and are detailed in the §B.2 and §B.3. **b)** Model of the time dynamics using a Lindblad master equation approach (§B.3).

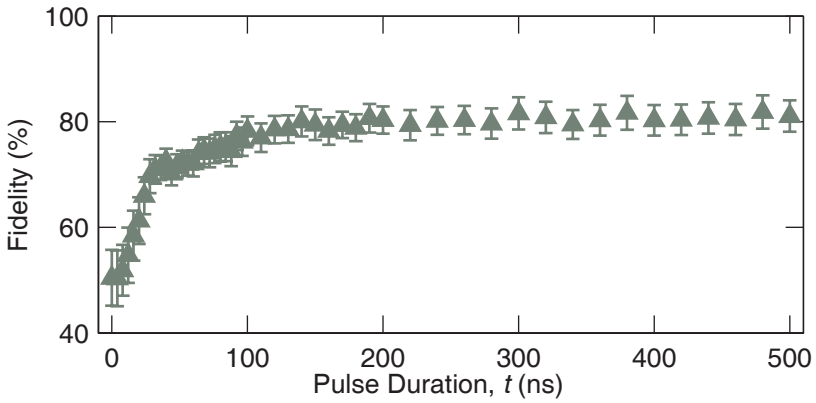

Figure 3.5: Fidelity of coherent population trapping Fidelity of initialized spin state as a function of pulse duration. Fidelity is compared to the pure state $|D\rangle$.

evolves towards the dark state regardless of its initial state, and a theoretical model, based on a Lindblad master equation approach, accounting

for both Λ systems (Fig. 3.4b) is in qualitative agreement with our data (§3.7.4 and §B.3). As a function of pulse duration, the initialization fidelity saturates at about 80% after 100 ns (Fig. 3.5). The fidelity is limited, in particular, by decoherence from optical coupling to the second nearby Λ system, as well as finite T_2^* spin coherence [80], spectral diffusion [35], and some pumping into the third spin state $|-1_g\rangle$ (§B.4).

3.3.2 Arbitrary spin-state initialization

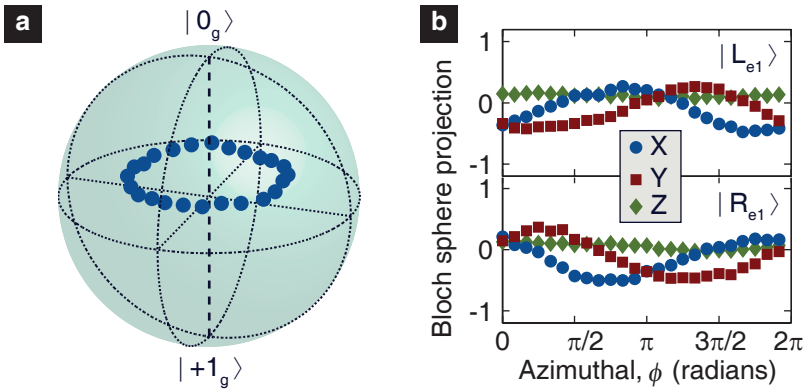

Figure 3.6: Arbitrary spin-state initialization: azimuthal a) Azimuthal initialization of spins via CPT on resonance with $|R_{e1}\rangle$. Varying the relative phase between the two optical fields (ϕ) changes the azimuthal location. **b)** X, Y, and Z projections of azimuthal initialization, on resonance with $|L_{e1}\rangle$ (top) vs. the orthogonal state $|R_{e1}\rangle$ (bottom). Error bars are within point size. Prior to CPT, the spin was polarized into $|+1_g\rangle$ (§B.2). The CPT pulse duration was 200 ns (a)) or 100 ns (b)). Errors are ∼2x the point size, and are detailed in §B.2.

The allure of this technique is the ability to initialize the spin arbitrarily on the Bloch sphere solely by varying the relative phase and amplitude of the two optical fields. In Fig. 3.6a, we demonstrate initialization along

different equatorial points of the Bloch sphere by changing the relative phase between the two driving optical fields resonant with $|R_{e1}\rangle$. Because $|R_{e1}\rangle$ and $|L_{e1}\rangle$ are orthogonal spin mixtures, tuning the lasers to $|L_{e1}\rangle$ instead is equivalent to shifting ϕ of the final state by π radians (Fig. 3.6b). Alternatively, by tuning the relative amplitudes of the two optical fields, we initialize the spin at various points along a meridian of the Bloch sphere (Fig. 3.7a). Finally, we combine polar and azimuthal control to demonstrate spin initialization at points along a great circle rotated $\pi/4$ radians from the polar axis (Fig. 3.7b).

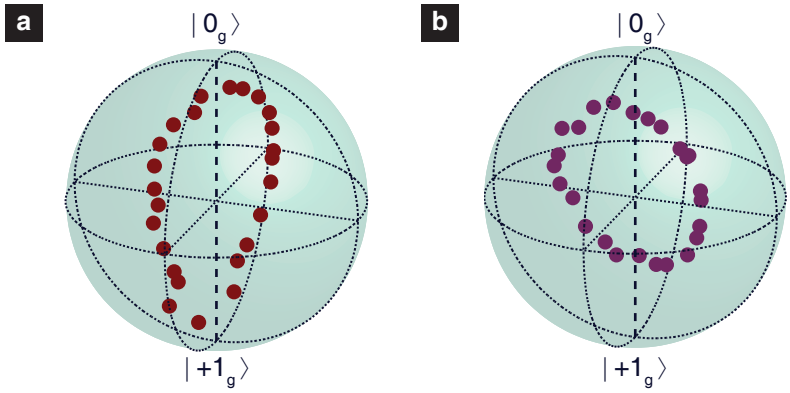

Figure 3.7: Arbitrary spin-state initialization: polar and great circle a) Polar initialization of spins, on resonance with $|R_{e1}\rangle$. Varying the relative amplitude between the two optical fields ($\tan(\theta/2)$) changes the polar location. **b)** Initialization of spins along a great circle canted $\pi/4$ off the polar axis, achieved through control of both the relative phase and amplitude of the two optical fields. Prior to CPT, the spin was polarized into $|+1_g\rangle$ (§B.2). The CPT pulse duration was 200 ns. Errors are ∼2x the point size, and are detailed in §B.2.

3.4 Arbitrary-basis spin readout via CPT photoexcitation

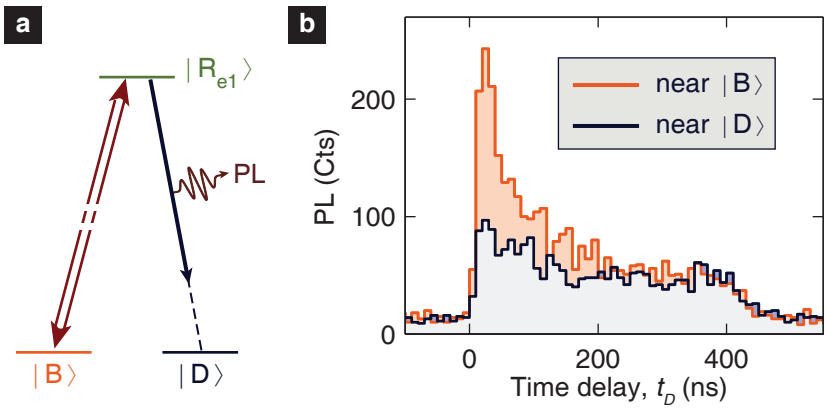

Figure 3.8: Dark/bright projection technique a) Λ configuration recast in terms of ground state orthogonal superpositions, the bright $|B\rangle$ and dark $|D\rangle$ states. The driving fields are similarly recast as an optical pump on the bright state transition. **b)** The emitted PL response of the NV center spin as it settles into the dark state, starting either near the bright or dark state. This trace is a sum of 2.3×10^6 iterations with the data binned into 10 ns time intervals.

Readout along an arbitrarily-chosen basis [81] is realized through a complementary process as the emitted PL during the CPT interaction with the two optical fields is proportional to the projection of the spin along the bright-state axis. This can be thought of as a recasting of the ground states of our Λ system in terms of the bright and dark states, orthogonal superpositions of the original spin eigenstates $|0_g\rangle$ and $|+1_g\rangle$. The two driving light fields are correspondingly recast as a single optical pump acting on the bright state transition (Fig. 3.8a), since they do not couple to the dark state from destructive interference of photoexcitation. During

the interaction, the spin evolves toward the dark state, and the emitted PL provides a measure of the spin state prior to the interaction (Fig. 3.8b). This technique, which we refer to as dark/bright-state projection (DBP), bears similarity to electromagnetically induced transparency [72], but we instead measure the transient optical response of the NV center rather than the amount of transmitted light.

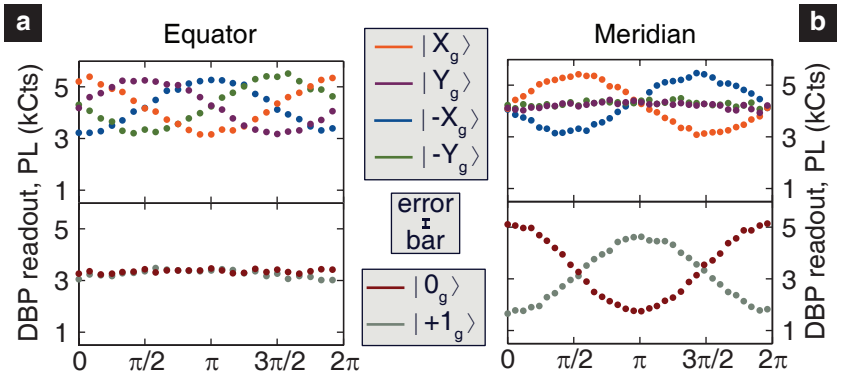

Figure 3.9: Arbitrary basis readout a) Spins initialized at points along the equator and read out through DBP. The DBP basis is chosen such that the corresponding bright state, indicated in the legend, is at one of four points on the equator (top panel) or one of the poles (bottom panel). **b)** Spins initialized at points along a meridian, mapping out Rabi oscillations, and read out via DBP in the same bases as in C. Error bars represent 1σ shot noise.

To demonstrate arbitrary-basis readout, we prepare the spin state with ESR pulses either along various positions on either the equator (Fig. 3.9a) or a meridian (Fig. 3.9b) of the Bloch sphere, and then use DBP to read out the spin state along six separate bases with bright states corresponding to the $\pm X$, $\pm Y$, and $\pm Z$ positions of the rotating frame Bloch sphere. The number of photons measured is in direct proportion to the projection of the

spin state along the chosen axis. The signal-to-noise of spin readout using DBP along polar bright states is comparable to traditional spin readout techniques via the intersystem crossing, while DBP spin readout along equatorial states requires roughly 3x more averaging (§B.5) to achieve a similar signal-to-noise ratio.

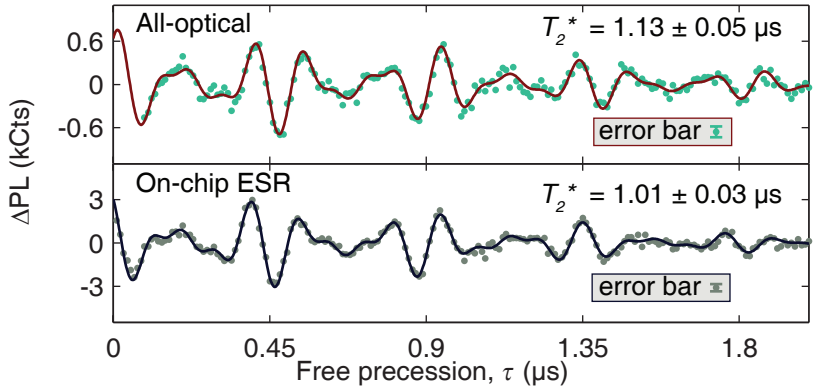

Figure 3.10: All-optical Ramsey measurement (top) All-optical Ramsey experiment, detuned such that $\omega_{mw} - \delta_{GS}/\hbar = 2\pi \cdot 7.5\,\text{MHz}$. The CPT initialization and DBP readout pulses are each 50 ns in duration. (bottom) Room-temperature Ramsey measurement using ESR pulses with similar detuning for comparison. All error bars represent 1σ shot noise.

By combining both CPT initialization and DBP readout, we perform an all-optical Ramsey measurement [82] by varying the delay between the CPT and DBP pulses in order to measure the transverse inhomogeneous spin coherence time, T_2^* (Fig. 3.10, top). Collapses and revivals in the signal are indicative of hyperfine coupling to the ^{14}N spin. The all-optical response is similar to Ramsey measurements taken at room temperature using ESR pulses and traditional intersystem crossing-based initialization

and readout (Fig. 3.10, bottom). Further details can be found in §B.6.

3.5 Arbitrary-axis spin rotations via stimulated Raman transitions

Within this same Λ system framework, we also demonstrate unitary spin rotations about any qubit axis via SRT. By detuning ω_L from resonance while keeping $\omega_{mw} = \delta_{GS}/\hbar$, driving the Λ system produces adiabatic energy shifts of the bright state during the laser pulse without modifying the dark state energy, generating unitary spin rotations [21, 42, 71, 77] along the dark/bright state Bloch sphere axis. In order to drive rotations about an equatorial axis, we tune the two equal-intensity ($\tan(\theta/2) = 1$) driving fields to be centered between the $|R_{e1}\rangle$ and $|L_{e1}\rangle$ resonances, such that SRT generated from both Λ systems add constructively while CPT effects from both reduce coherence but produce no net spin polarization due to competing dark states. In Fig. 3.11a, we present the dynamics of SRT spin rotations along two different equatorial rotation axes of the Bloch sphere ("σ_X" or "σ_Y"), corresponding to different relative phases (ϕ) of the two optical fields. We measure a 69% process fidelity for a "σ_X" or "σ_Y" π-rotation, limited largely by spontaneous decay. Rotations about non-equatorial axes, such as the polar axis [42] ("σ_Z"), are also achievable in this system (Fig. 3.11b) but require different configurations of the light fields (§B.3).

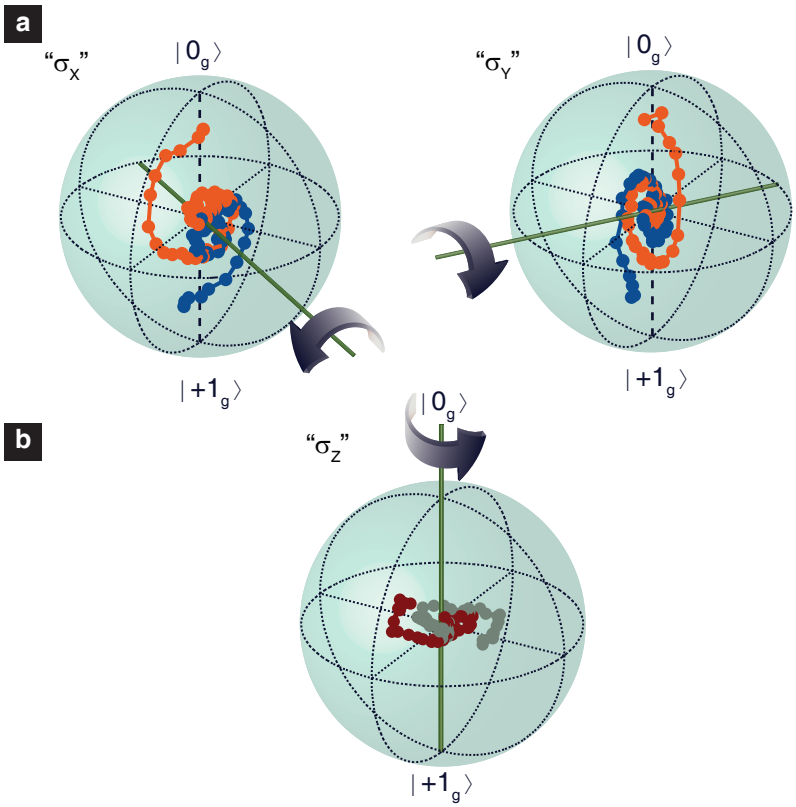

Figure 3.11: Arbitrary-axis rotations of the NV center spin a) Bloch sphere representation of "σ_X" and "σ_Y" coherent rotations at ∼10 MHz due to SRT. The two measurements correspond to different relative EOM driving phases (ϕ), separated by $\pi/2$ radians, and show the trajectory of a spin originating near $|0_g\rangle$. (orange) and $|+1_g\rangle$. (blue). The axes of rotation are added as guides to the eye. **b)** Bloch sphere representation of "σ_Z" coherent rotations due to SRT, showing spin trajectories originating near orthogonal points on the equator (maroon and grey). Errors are ∼2x the point size, and are detailed in §B.3.

Finally, to illustrate the full suite of these optical control protocols, we present an all-optical Hahn echo measurement of an NV center spin's homogeneous spin coherence time, T_2. This measurement consists of a CPT laser pulse for spin initialization along the Bloch equator, followed by a SRT laser pulse to flip the spin to produce an echo, and finally a DBP

readout pulse to measure the final spin state along an equatorial basis (§B.7). We determine T_2 ∼900 µs, corroborated by an ESR-based Hahn echo measurement at room temperature (Fig. 3.12).

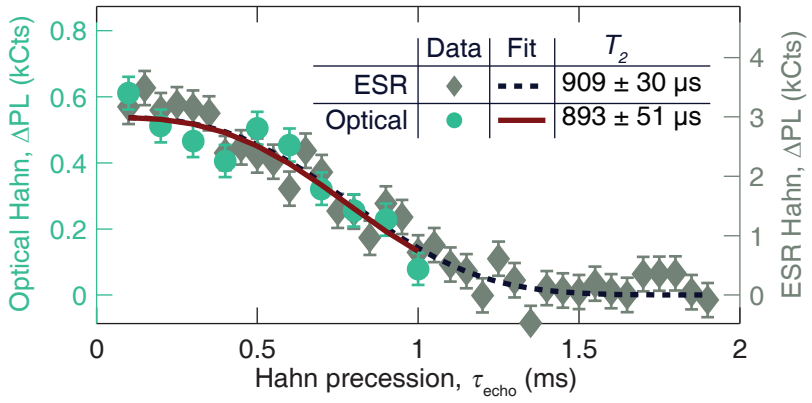

Figure 3.12: All-optical Hahn echo measurement All-optical Hahn echo measurement (green points) consisting of CPT spin initialization, a π spin rotation via SRT, and DBP spin readout fit according to the equation on the graph. Room temperature Hahn measurement via ESR pulses is also shown (grey points). Error bars are 1σ shot noise.

3.6 Conclusions and outlook

We demonstrate all-optical initialization, readout, and coherent unitary rotations of an individual NV-center spin, forming a triumvirate of protocols for single-spin control that can be performed along any arbitrarily-chosen basis. Using these protocols, we demonstrate two measurements of transverse spin coherence solely with optical pulses. The ability to select any basis allows for quantum operations to be implemented directly without the need for extra control steps to project onto or from the preferred en-

ergy eigenstate basis. This eliminates the need for ESR operations [79], enabling control of individual spins within a much smaller device footprint, with promise for large-scale implementations of spin arrays [83] or photonic networks [51, 52]. Perhaps most importantly, these methodologies mitigate the need for the NV center's intersystem crossing spin-selectivity and thus can be used to investigate and control a wide array of defects and other localized quantum states in solid-state materials, not just those with NV-like structures [29, 30]. As such, these techniques open the door to exploring quantum coherence and developing quantum information platforms in a broad range of semiconductors and nanostructures.

3.7 Methods

3.7.1 Sample

The sample was a $2 \times 2 \times 0.5$ mm electronic grade diamond purchased from Element Six, consisting of < 5 ppb nitrogen that was irradiated with a 1e14 electrons/cm^2, 2 MeV dose and subsequently annealed at 850 °C for two hours. Ti/Pt/Au devices, consisting of DC pads and a short-terminated waveguide, were deposited on the sample using standard photolithographic techniques. All experiments were performed in a confocal microscopy setup (§B.1) with a liquid helium flow cryostat held at 8 K. The sample was thermally sunk to the cryostat and the waveguide was wirebonded to a microwave line in the cryostat for on-chip ESR. The stud-

ied NV center excited state orbital strain splitting between $m_s = 0$ spin sublevels varied from 4.6 GHz to 5.8 GHz between cryostat cooldowns as thermal cycling modified the crystal strain. As a result, the DC-applied magnetic field at which the lower-branch excited state spin anticrossing occurred varied ($550 - 750$ G) which led to variations in the ground state spin splitting between $|0_g\rangle$ and $|+1_g\rangle$ ($\delta_{GS}/h \sim$4.3 to 5.0 GHz).

3.7.2 Experimental techniques

Our confocal microscopy setup consists of a 100 mW 532 nm non-resonant excitation laser used for the standard NV center intersystem crossing spin initialization and readout protocol [84], and two tunable 637 nm lasers resonant with various NV center optical transitions. The light field from one of the resonant lasers was fiber-coupled to an EOM in order to split the optical field, at ω_L, into different frequency sidebands, separated by ω_{mw}, to optically drive the Λ system. For the CPT and SRT measurements, a second resonant laser functioned as a one-color spin-state readout laser along the S_Z basis by being resonant with the $|0_g\rangle$ to $|0_{e2}\rangle$. transition [38] (Fig. 3.1a) resulting in higher collected PL when the spin was in $|0_g\rangle$. In Fig. 3.11b only, the light field from this second resonant laser was instead fiber-coupled to a second EOM, where the first laser was used to perform CPT and DBP and the second laser was used to perform SRT for this Hahn echo pulse sequence. All three lasers were gated using separate acousto-

optic modulators (AOMs) for pulse timing control. They were subsequently passed through a variety of polarization optics, combined with beamsplitters, and focused onto the sample with a 0.85 numerical aperture 100× microscope objective that is aberration-corrected for the cryostat window. PL from the NV's red-shifted phonon sideband was collected back through the objective, filtered by dichroic beamsplitters, and focused onto a silicon avalanche photodiode (APD).

Microwaves to drive the EOM(s) and for on-chip microwave ESR driving [79] originated from the same signal generator at frequency $\omega_{mw}/(2\pi)$, which varied from $4.3 - 5.0\,\mathrm{GHz}$ due to variations in δ_{GS}/h from changes in NV center strain. The microwaves going to the EOMs and to the sample for ESR passed through IQ modulators for phase control between the various CPT, SRT, DBP, and ESR pulses. These microwave signals were also gated in time and amplitude-controlled using microwave modulators and switches. Timing for the microwave switches, AOMs, and IQ modulators were controlled by an arbitrary waveform generator, a PulseBlaster card, and a pulse-pattern generator. Pulse sequences used for these experiments consisted of a traditional initialization pulse at 532 nm as a spin reset, followed by a sequence consisting of a number of the following techniques: on-chip microwave ESR pulses as well as techniques utilizing the 637 nm tunable lasers, including CPT spin-state initialization, DBP spin-state readout, $|0_{e2}\rangle$ spin-state readout, and/or SRT coherent spin rotation.

Details for each pulse sequence are discussed throughout Appendix B. A magnetic field was applied along the NV center axis with a permanent magnet on a motorized stage and was adjusted to tune to the anticrossing used.

3.7.3 Quantum state tomography

To perform quantum state tomography on our CPT spin-state initialization and SRT coherent rotation, we read out the X, Y, and Z projections of the post-interaction state. All projections were mapped onto the S_Z basis using ESR pulses and then read out with the laser resonant with $|0_{e2}\rangle$. We applied a Bayesian approach to the tomographical reconstruction of the spin state [85], detailed in §B.2, that takes into account finite readout contrast, laser drift, and axial/length imperfections in the microwave rotations used to project the different spin components.

3.7.4 Theoretical modeling

To describe the dynamics of the NV center spin under optical excitation in the Λ level configuration [13], we include five energy levels: two out of the three ground-state levels $|0_g\rangle$, $|+1_g\rangle$, the two mixed excited states $|L_{e1}\rangle$ and $|R_{e1}\rangle$ as the upper state of each Λ system, as well as the intermediate singlet $|S\rangle$ which here plays a role for unintentional intersystem crossings. The Hamiltonian, in the rotating frame, for the subspace spanned by these

five basis states can be expressed as

$$H = \sum_{\alpha} \epsilon_{\alpha} |\alpha\rangle\langle\alpha| + \sum_{G=0,1} \sum_{E=R,L} \Big(\Omega_{GE} |E_{e1}\rangle\langle G_g| + h.c. \Big), \tag{3.1}$$

where the first sum runs over all states $\alpha = 0_g, +1_g, L_{e1}, R_{e1}, S$ with corresponding energies $\epsilon_{0_g} = \epsilon_{+1_g} = \Delta_L$ (where Δ_L is detuning of ω_L from resonance to a Λ system), $\epsilon_{R_{e1}} = 0$, $\epsilon_{L_{e1}} = -\delta_{e1}$, and ϵ_S. The laser excitation from one of the lower states $G = 0, 1$ to one of the upper states $E = L, R$ is described by the Rabi frequencies in the rotating frame,

$$\Omega_{1E} = \Omega \cos(\theta/2) \tag{3.2}$$

$$\Omega_{0E} = \pm\Omega \sin(\theta/2) e^{i\phi} \tag{3.3}$$

where the upper (lower) sign holds for $E = R$ ($E = L$).

We studied the time evolution of the system by numerically solving the Lindblad master equation [86, 87] for the density matrix of the NV center in the rotating frame. In addition to coherent processes such as excitation from the two driving fields, the master equation also accounts for spontaneous decays of charge and spin with some rates known from independent experiments. In the idealized, long-time limit case, with only one excited level included, the resulting eigenvector with eigenvalue 0 corresponds to the dark state:

$$|D\rangle = \cos(\theta/2)|0_g\rangle \mp e^{-i\phi} \sin(\theta/2)|+1_g\rangle \tag{3.4}$$

where the upper (lower) sign holds for the single excited state level being $E = R(E = L)$. In actuality, the steady state is described by a mixed state which can deviate slightly from $|D\rangle\langle D|$. The simulated behavior of the NV spin during CPT and SRT is in good qualitative agreement with the experimental data (Fig. 3.4 and Fig. B.6-B.9). Further details can be found in §B.3.

Chapter 4

Optical accumulation of Berry phase in the NV center

The following chapter is adapted from a recently submitted manuscript [56]. I worked on this experiment in a joint effort with F. Joseph Heremans and Brian Zhou. Theoretical modelling was developed by Adrian Auer and Guido Burkard. Further details from this experiment can be found in Appendix C.

4.1 Geometric phases

When a quantum mechanical system evolves slowly along a closed loop in its parameter space, a given eigenstate may acquire a phase consisting of both a dynamic and geometric contribution. First proposed by S. Pancharatnam [88] in his study of cyclic rotations of the polarization of light, and later generalized by M. V. Berry [89], this adiabatic geometric phase

is determined solely by the geometry of the traversed loop, in contrast to the dynamic phase that accumulates from the energetics and travel time of the intervening state evolution. Since the Berry phase is proportional to the area enclosed by the path in parameter space, it is intrinsically resilient to noise that causes deviations to the path but conserve the total enclosed area [90, 91]. Geometric control thus represents a promising avenue for constructing fault-tolerant quantum logic gates [92, 93].

Control over geometric phases, occurring both when the cyclic evolution is traversed adiabatically [89] and non-adiabatically [94], has been demonstrated in a variety of physical platforms, including liquid nuclear magnetic resonance [95], trapped atoms [96], and more recently in the solid-state in superconducting qubits [97, 98] and defect spins [99, 100, 101]. However, current implementations of geometric phase control in solid-state systems have utilized microwaves that are difficult to localize and thus concede the ability to selectively address nearby qubits without crosstalk. Here, we manipulate the Berry phase in a solid-state qubit using diffraction-limited resonant laser fields. This opens the possibility for independent manipulation of single qubits in photonic networks [50] and spin arrays [83] through geometric principles where fine control over the energetics is inessential. While a similar optical protocol has been recently realized using trapped calcium ions [102], our realization in the solid state offers potential integration into photonic platforms and harnesses larger energy scales to enable

significantly faster adiabatic control.

The method we employ is based on proposals to accumulate geometric phases via stimulated Raman adiabatic passage (STIRAP) [103, 104]. In STIRAP, two laser fields couple two levels $|\alpha\rangle$ and $|\beta\rangle$ to a single excited level $|\varepsilon\rangle$ in a lambda (Λ) configuration (Fig. 4.1a). As discussed in Ch. 3 The amplitude and phase relation between the two laser fields define a new zero-energy eigenstate in the interaction picture, known as the dark state $|D\rangle$, a superposition of the $|\alpha\rangle$ and $|\beta\rangle$ states that does not couple to the light fields due to destructive interference. By adiabatically adjusting the amplitude and phase of the optical fields, any initial dark state can be connected to any other final dark state, thus transporting the state arbitrarily on the Bloch sphere spanned by $|\alpha\rangle$ and $|\beta\rangle$. Traditionally, STIRAP has been utilized in atomic [105, 14] and solid-state systems [22, 23] for highly efficient population transfer between the states $|\alpha\rangle$ and $|\beta\rangle$ bypassing the potentially lossy excited state $|\varepsilon\rangle$ (pole to pole evolution, shown by the red gradient curve in Fig 4.1b). However, when STIRAP is extended to a full loop (red and blue gradient curves together in Fig 4.1b), the dark state returns to itself and accumulates a Berry phase, γ_B, [102, 103, 104] proportional to the solid angle enclosed on the Bloch sphere. In this work, we demonstrate Berry phase control through the adiabatic passage of a dark state within a single negatively charged nitrogen-vacancy (NV) center in diamond.

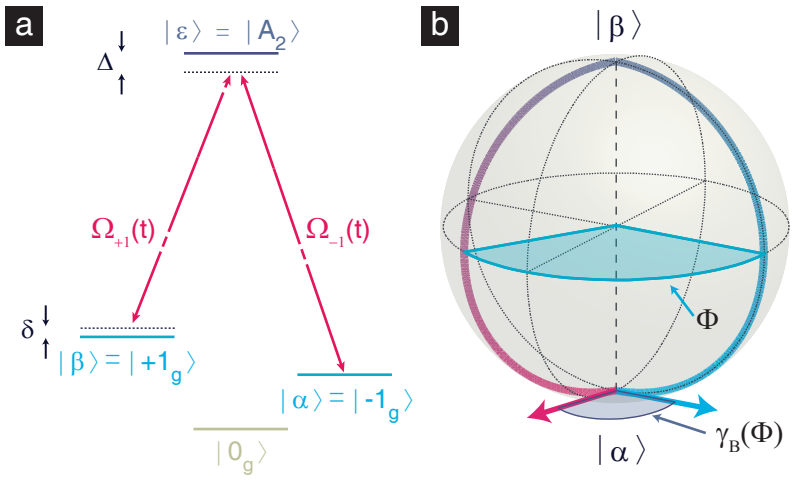

Figure 4.1: STIRAP to enclose Berry phase a) Λ system within the NV center level structure consisting of $|-1_g\rangle$ and $|+1_g\rangle$ coupled to the spin-orbit excited state $|A_2\rangle$ by two optical driving fields $\Omega_{+1}(t)$ and $\Omega_{-1}(t)$, with one-photon detuning, Δ, and two-photon detuning, δ. **b)** Time trace (red $\rightarrow$ blue gradient) of state transfer through STIRAP on the Bloch sphere. The gradient red trajectory indicates transfer from a dark state $|\alpha\rangle$ to a dark state $|\beta\rangle$. Returning the dark state to $|\alpha\rangle$ along a different longitude (gradient blue) encloses a wedge angle, Φ. Berry phase, γ_B, accumulates on $|\alpha\rangle$, proportional to Φ.

4.2 Understanding STIRAP in the NV Center

4.2.1 The A_2 Λ system in the NV center

We exploit a natural Λ system within the NV center level structure, at cryogenic temperatures ($T = 8\,\mathrm{K}$), formed by its ground state $m_S = -1$ and $+1$ spin states, or $|-1_g\rangle$ and $|+1_g\rangle$, coupled to the $|A_2\rangle$ spin-orbit excited state [23, 40, 41] (Fig. 4.1a). We tune this Λ system into a non-degenerate configuration using a 117 G external magnetic field along the

NV center axis to Zeeman split $|-1_g\rangle$ and $|+1_g\rangle$ by 655 MHz. On-chip microwave control [26] enables rotations between the third ground state $|0_g\rangle$ and either $|-1_g\rangle$ or $|+1_g\rangle$. These microwaves are used only for the preparation and tomographic projection of the spin state (described in detail in §C.3.2), but are not involved in the accumulation of the geometric phase. Instead, we address our Λ system using a narrow-line tunable 637 nm diode laser (470 THz) fiber coupled into an electro-optic modulator (EOM). Driving the EOM with a signal generator places frequency harmonics on the laser equivalent to the $|-1_g\rangle$ / $|+1_g\rangle$ splitting (655 MHz) (Fig. 4.2a). A phase quadrature modulator controlled by an arbitrary waveform generator governs the relative amplitude and phase relations among these harmonic sidebands on nanosecond timescales. From this, we achieve full Bloch sphere control over the resultant dark state, $|D\rangle$ [55].

4.2.2 'Tangerine slice' trajectories with STIRAP

In our experiment, the red-shifted first harmonic of the laser is tuned to the $|+1_g\rangle$ to $|A_2\rangle$ transition with Rabi coupling strength $\Omega_{+1}(t)$, and the zeroth harmonic is tuned to the $|-1_g\rangle$ to $|A_2\rangle$ transition with Rabi coupling strength $\Omega_{-1}(t)$ (Fig. 4.2a). The two laser fields are deliberately detuned from the one-photon resonance by a red shift $\Delta \approx 65 \pm 15$ MHz to limit unintended absorption during STIRAP, while detuning from the two-photon resonance by $|\delta| < 150$ kHz arises due to experimental uncertainty

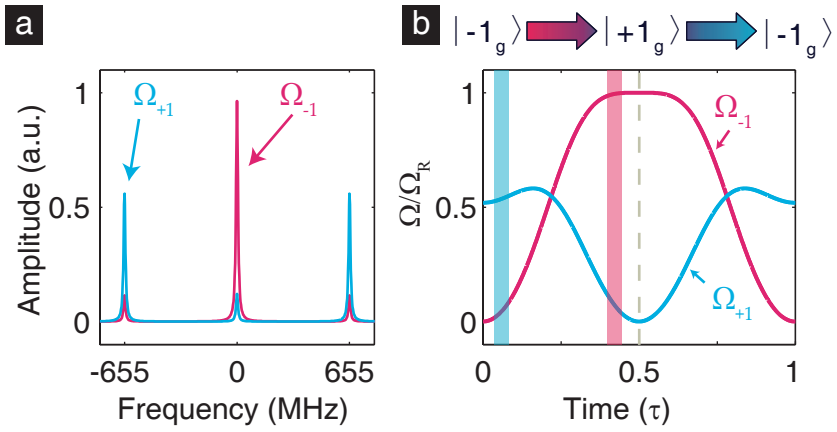

Figure 4.2: Time evolution of the optical fields a) Frequency harmonics of the electro-optic modulator split by 655 MHz, to drive both transitions in the Λ system. Assignment of harmonics to transitions is indicated. **b)** Example trace of the relative optical Rabi frequency of the driving fields, $\Omega_{+1}(t)$ (blue) and $\Omega_{-1}(t)$ (red), as a function of time showing the movement of the dark state from the $|-1_g\rangle$ pole ($t = 0$) to the $|+1_g\rangle$ pole ($t = \tau/2$) and back ($t = \tau$) during a STIRAP interaction. The pump amplitudes in a) correspond to the times highlighted by the red and blue linecuts in b).

(see §C.4.2). In our protocol, we begin by preparing the spin into $|-1_g\rangle$. We then apply only $\Omega_{+1}(t)$ which sets $|-1_g\rangle$ as the dark state. By adiabatically shifting the relative intensity from Ω_{+1} to Ω_{-1}, the dark state gradually moves on the surface of the Bloch sphere from $|-1_g\rangle$ to the opposite $|+1_g\rangle$ pole (Fig. 4.2b), with minimal absorption through the $|A_2\rangle$ excited state. The precise time evolution of the field amplitudes $\Omega_{+1}(t)$ and $\Omega_{-1}(t)$, displayed in Fig. 4.2b, is governed by the pulse shape applied to the EOM and the harmonic generation relation in an EOM (§C.3.1). A phase shift, Φ, between the optical fields at the opposite pole ($t = \tau/2$) and a reversal of the intensity shift returns the dark state to the $|-1_g\rangle$ pole along a different

longitude on the Bloch sphere completing a cyclic route in traversal time τ. This 'tangerine slice' trajectory with wedge angle, Φ, circumscribes a solid angle, 2Φ, and gives rise to an accumulated Berry phase. (Figs. 4.1b, 4.2b)

4.2.3 Tomography of the STIRAP trajectory

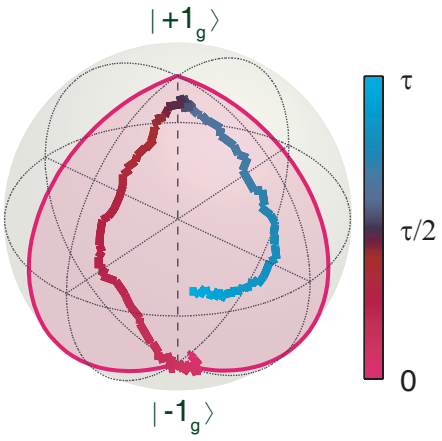

Figure 4.3: Tomography of the STIRAP 'tangerine slice' Tomographically reconstructed path of the spin on the $|-1_g\rangle$ / $|+1_g\rangle$ Bloch sphere during the STIRAP interaction moving from $|-1_g\rangle$ to $|+1_g\rangle$ and back enclosing $\Phi = 120°$ ($\tau = 1200$ ns). The shaded region shows the solid angle enclosed by the ideal trajectory.

Prior to investigating the Berry phase, we explore the mechanisms limiting STIRAP in the NV center by tomographically reconstructing the path of the spin on the $|-1_g\rangle$ to $|+1_g\rangle$ Bloch sphere (Fig. 4.3). In this particular instance, we demonstrate a trajectory with outbound (red) and inbound (blue) paths separated by $\Phi = 120°$ for an adiabatic cycle time of $\tau = 1200$ ns and a peak optical Rabi frequency $\Omega_R = 31 \pm 3$ MHz for the Ω_{-1} transition. From this time-resolved reconstruction, we observe that

the length of the dark state Bloch vector (Fig. 4.4a) decreases around the equator, revives near the opposite pole, and ultimately returns to the initial pole with 65% of its original magnitude.

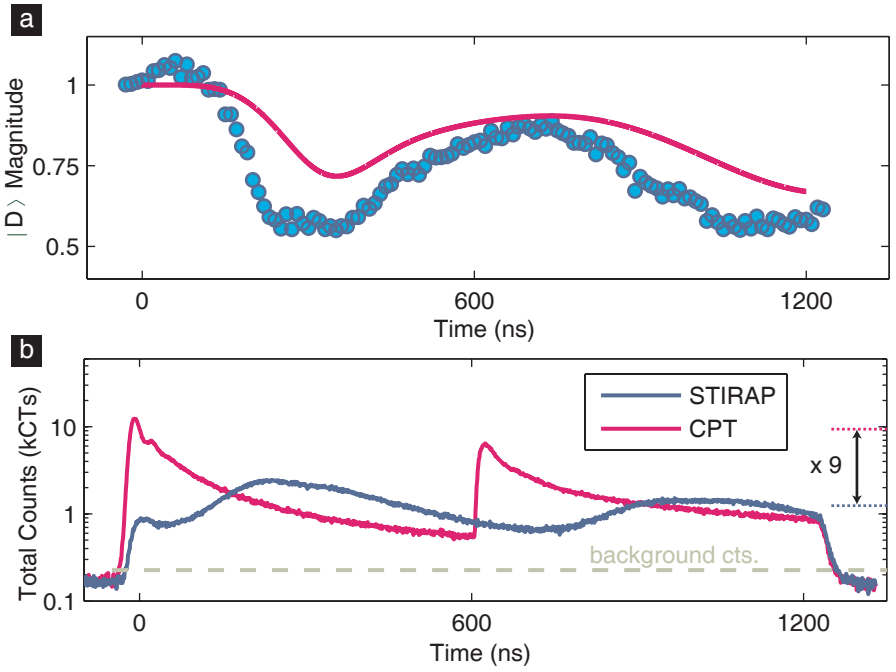

Figure 4.4: Evaluating STIRAP a) The magnitude of the dark state during the same STIRAP interaction shows a sharp decrease around the equator due to occupation of non-dark states from non-adiabatic transitions. The gradual decrease in the magnitude over time is attributed to loss out of the $|-1_g\rangle$ / $|+1_g\rangle$ subspace into $|0_g\rangle$. The red curve is calculated from the master equation simulation and is plotted for comparison. **b)** Time-resolved photoluminescence (PL) during an experimentally identical STIRAP interaction as in a), plotted against a non-adiabatic CPT interaction on a log scale. The relative darkness of the PL during STIRAP indicates that it is a largely adiabatic evolution. Comparing a) and b), we see the PL during STIRAP peak when the state is near the equator during both outbound and inbound trajectories, corresponding to excitation as a result of non-adiabatic following of the path velocity.

This decrease in the state magnitude along the traversal is due to a lag in the adiabatic following of the dark state. Increases in the velocity of the

trajectory can cause coupling strengths between the dark and non-dark eigenstates to exceed their energy gap, leading to non-adiabatic evolution. These gaps decrease with weaker driving fields, Ω_R. Non-adiabatic effects raise the likelihood of occupying non-dark states that include components of the excited state $|A_2\rangle$ [105]. Occupation of these states reduces the overall magnitude of the state vector, as these states point in different directions with respect to the intended dark state in the $|-1_g\rangle$ / $|+1_g\rangle$ Bloch sphere. Furthermore, as they contain components in $|A_2\rangle$, absorption can occur and lead to decay either into the intended dark state, causing recovery of the magnitude, or into $|0_g\rangle$, causing irreversible loss out of the subpace. For our STIRAP pulse shape, these effects manifest as sharp decreases in the magnitude where the velocity of trajectory is greatest (near the equator). These dips partially recover as the velocity of the path slows and the trapping rate into the recaptured dark state increases near the $|+1_g\rangle$ pole. Additionally, loss out of the subspace accumulates over the trajectory causing a gradual decrease in dark state magnitude. A four-state master equation capturing these effects is presented in §4.6 and §C.1 and reproduces the trajectory in Fig. 4.4a. Finally, we tomographically reconstruct other trajectories for paths enclosing $\Phi = 0^\circ$ to 330° in 30° increments, all revealing similar features. Plotted in Fig. 4.5 are the inbound trajectories of these paths demonstrating the ability to enclose any wedge angle Φ.

To further qualify the adiabaticity of the path, we measure the photolu-

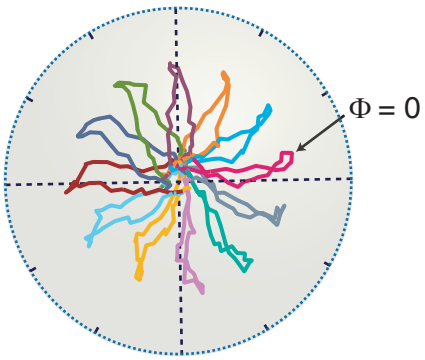

Figure 4.5: Inbound trajectories enclosing various Φ Inbound trajectories of STIRAP loops enclosing $\Phi = 0°$ to $330°$ in $30°$ steps indicating full Bloch sphere control over cyclic paths.

minescence (PL) during the STIRAP transition. Non-adiabatic evolution permits excitation to $|A_2\rangle$ and emitted photons, while adiabatic evolution remains dark. The time-resolved PL during STIRAP (Fig. 4.4b, blue) indicates that the interaction is dark when compared to a non-adiabatic interaction that optically pumps the spin from $|-1_g\rangle$ to $|+1_g\rangle$ and then pumps the spin back to $|-1_g\rangle$ midway through the interaction (Fig. 4.4b, red). This optical pumping is a form of coherent population trapping (CPT) [15, 55]. In fact, the average number of photons emitted during the STIRAP interaction is 9 times fewer than the number of photons emitted at the beginning of the CPT interaction when the population is maximally inverted, indicating that STIRAP is significantly more adiabatic than CPT. Notably, we observe that additional photon emission (Fig. 4.4b) coincides with a reduction in the dark state vector (Fig. 4.4a), both consequences

of the loss of adiabatic following.

4.3 Optical accumulation of Berry phase

4.3.1 Measuring Berry phase

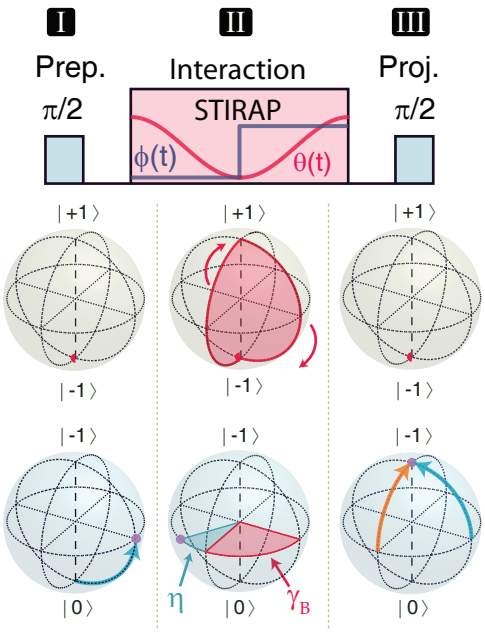

Figure 4.6: Sequence to measure Berry phase Pulse sequence to measure Berry phase accumulated during STIRAP interaction (red and indigo curves denote the $\theta(t)$ and $\phi(t)$ trajectories). I. Prepare spin in fixed $|0_g\rangle$ / $|-1_g\rangle$ superposition using microwave techniques. II. Loop the spin on the $|-1_g\rangle$ / $|+1_g\rangle$ Bloch sphere enclosing Φ. Phase will accumulate on $|0_g\rangle$ / $|-1_g\rangle$ Bloch sphere corresponding to a combination of a fixed dynamic phase, η, and a varying Berry phase, γ_B, which is a function of Φ (Eq. 4.1). III. A final projection pulse reads out the accumulated phase on $|0_g\rangle$ / $|-1_g\rangle$ Bloch sphere through state tomography.

With the ability to enclose loops of arbitrary wedge angle, Φ, on the $|-1_g\rangle$ / $|+1_g\rangle$ Bloch sphere, we extend this STIRAP technique to observe the Berry phase, γ_B, accumulated on $|-1_g\rangle$ after a cycle has completed. To

measure this phase, we exploit the triplet nature of the NV center ground state by using the third state $|0_g\rangle$ as a phase reference. We begin by placing the spin into a fixed $|0_g\rangle$ / $|-1_g\rangle$ superposition. We then use STIRAP to enclose a given Φ on the $|-1_g\rangle$ / $|+1_g\rangle$ subspace with $\tau = 1200\,\text{ns}$ and $\Omega_R = 31\,\text{MHz}$. Phase then accumulates on $|-1_g\rangle$ relative to $|0_g\rangle$, which is measured by performing state tomography (Fig. 4.6). This final state has an accumulated phase that is the sum of a dynamic phase, η, that is constant for all wedge angles and a Berry phase, γ_B, that scales with the wedge angle as (see §4.6.3):

$$\gamma_B = -\Phi. \tag{4.1}$$

In Fig. 4.7, top, we show the X and Y tomographic projections of the final spin state for positive wedge angles (positive loops) and in Fig. 4.7, bottom, we repeat the same trajectories in reverse to enclose negative wedge angles (negative loops). Fitting all these projections to a global model consisting of a fixed dynamic phase, we determine that the acquired phase indeed matches the expected relation of the Berry phase to the wedge angle (Eq. 4.1). The amplitude of the oscillations in the X and Y projections, defined as the visibility, acts as a measure of the percentage of loops where adiabaticity is preserved. This visibility is reduced from unity as any non-adiabatic transition during the interaction nullifies the intended Berry phase for a given cycle. In Fig. 4.7, the visibility is limited to $\sim 22\%$, which is lower than the final dark state magnitude of 65% (in Fig. 4.4)

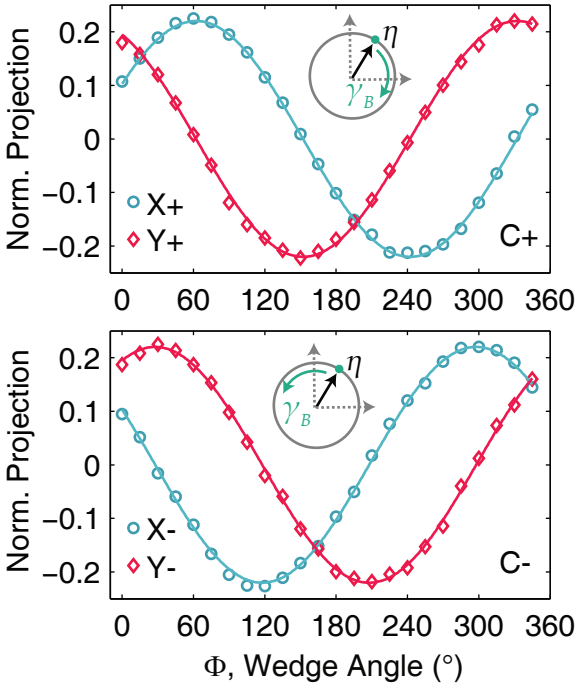

Figure 4.7: Optically accumulated Berry phase Resulting X and Y projections of the accumulated phase for a positive (top) and negative (bottom) loop. Projections fit to $X_\pm = A\cos(\eta \pm \gamma_B(\Phi))$ and $Y_\pm = A\sin(\eta \pm \gamma_B(\Phi))$ where A is the visibility and $\gamma_B(\Phi) = -\Phi$. Errors are approximately the size of the points.

as non-adiabatic transitions that nullify the Berry phase can nevertheless repopulate the dark state through absorption and decay. Unlike previous microwave demonstrations of Berry phase [91, 97, 101], the visibility of our Berry phase does not depend on the particular phase enclosed.

To confirm that the origin of the phase is purely geometric, we verify that the total acquired phase is additive when multiple loops are completed. For instance, when positive or negative loops are repeated (C_{++} /C_{--}), the net phase accumulation is proportional to the number of loops (Figs. 4.8, top and 4.9). Similarly, when we perform a positive loop followed directly

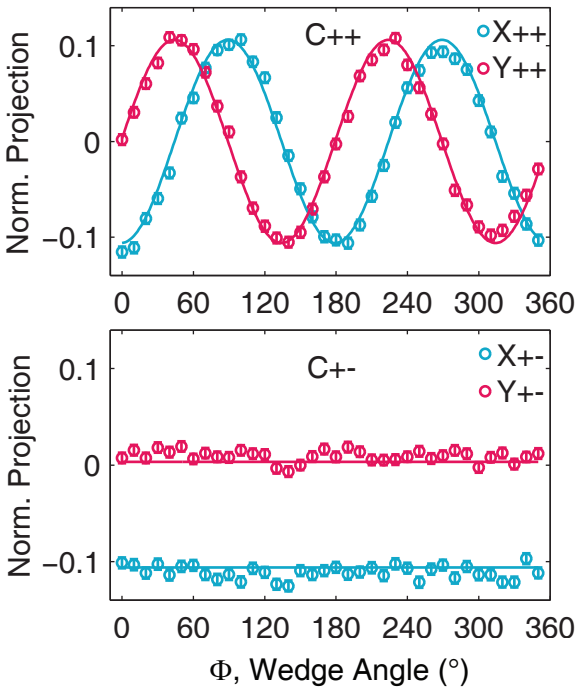

Figure 4.8: Double and cancelled accumulation of Berry phase (top) Resulting X and Y projections of the accumulated phase for a positive-positive loop. (bottom) Resulting X and Y projections of the accumulated phase for a positive-negative loop. All projections are fit to a model with common fit parameters: $X_{++} = A\cos(\eta + \gamma_B(2\Phi))$, $Y_{++} = A\sin(\eta + \gamma_B(2\Phi))$, $X_{+-} = A\cos(\eta + \gamma_B(0))$, and $Y_{+-} = A\sin(\eta + \gamma_B(0))$ where A is an amplitude, $\gamma_B(2\Phi) = -2\Phi$, and $\gamma_B(0) = 0$. Errors are approximately the size of the points.

by a negative loop (C_{+-}), the geometric phase is completely cancelled, leaving only the fixed dynamic phase (Fig. 4.8, bottom). The visibility decreases for multiple loop repetitions due to additional absorption over the increased interaction time.

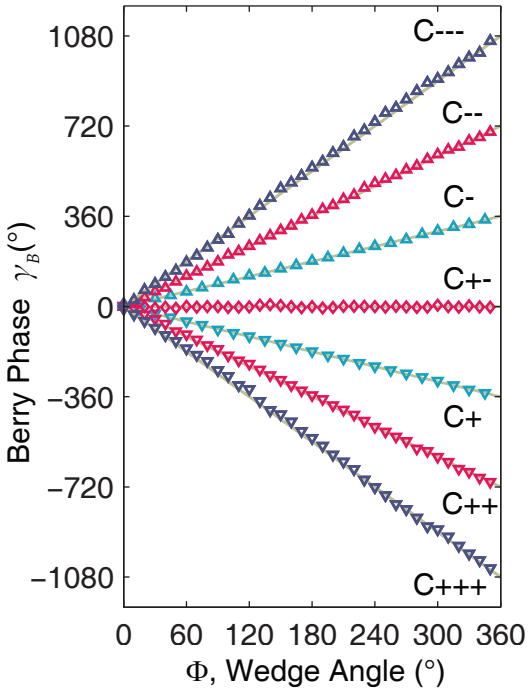

Figure 4.9: Additive nature of Berry phase Measured Berry phase when multiple loops of wedge angle Φ are traversed. Single loops (blue), double loops (red), and triple loops (indigo) indicate the expected additive behavior. A loop consisting of a positive loop followed by a negative loop of Φ (C_{+-}) indicates full cancellation of the Berry phase. The solid lines are guides to the eye ($\gamma_B = N\Phi$ for $N = -3, -2, , 3$). Errors are approximately the size of the points.

4.3.2 Origin of the dynamic phase

In addition to the Berry phase, the total phase measured also consists of a fixed dynamic contribution, η, that is sensitive to the traversal time and energetics of the interaction. During STIRAP, η results from an optical Stark effect [42] that shifts the energy of the dark state relative to the state $|0_g\rangle$, altering the spin's precession in the experimental rotating frame. At two-photon resonance where $\delta = 0$, the dark state does not couple to the

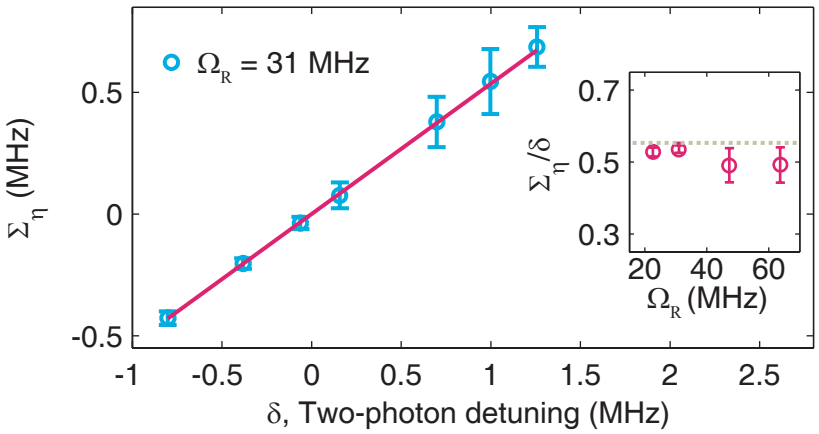

Figure 4.10: Dynamic phase resulting from the optical Stark effect The dark state energy shift, Σ_η, as a function of the two photon-detuning, δ, for a STIRAP interaction of maximum optical Rabi frequency, $\Omega_R = 31$ MHz. This energy shift multiplied by the traversal time τ determines the total dynamic phase accumulation. The inset displays the ratio of Σ_η/δ as a function of Ω_R. The dashed line indicates the expected behavior of $\Sigma_\eta/\delta = 0.55$ for small two-photon detuning. Errors represent 95% confidence intervals.

light fields and experiences no optical Stark shift; however, it is difficult to precisely set $\delta = 0$ a priori, and thus η arises from this imprecision. To determine the effect of η, we measure η and extract the optical Stark frequency shift, $\Sigma_\eta(\delta) = 1/(360°)\partial\eta(\tau,\delta)/\partial\tau$, isolating where $\Sigma_\eta = 0$ for $\delta = 0$ (§C.4.2). In Fig. 4.10 and its inset, we find that Σ_η scales linearly in δ, with a slope independent of the optical Rabi frequency, Ω_R. Perturbation theory in small δ reveals that Σ_η depends only on the ratio of the field amplitudes $\Omega_{-1}(t)/\Omega_{+1}(t)$, and yields an expected relation of $\Sigma_\eta = 0.55\delta$ given our pulse shape (Fig. 4.10, inset, dashed line), which matches well to the experimental result (§C.4.2). Unlike the dynamic phase, which requires

fine control of δ and τ, the Berry phase has no dependence on either of these parameters as long as STIRAP remains in the adiabatic regime.

4.4 Limits and robustness of Berry phase

To isolate the effects of adiabaticity and control noise on the Berry phase, we implement a Hahn echo sequence [97, 101] to cancel the dynamic phase. We begin with a positive loop that encloses $\gamma_{B,1} = -\Phi$ and accumulates a total phase $\xi_1 = \gamma_{B,1} + \eta$. A microwave π-pulse then flips the sign of the previously accumulated phase, after which we perform a negative loop that encloses $\gamma_{B,2} = \Phi$ and accumulates the same dynamic phase η, leading to an additional accumulation of $\xi_2 = \gamma_{B,2} + \eta$. This results in a total phase accumulation of $\xi = -\xi_1 + \xi_2 = 2\Phi$ with no contribution from the dynamic phase.

4.4.1 Decoherence and loss of adiabaticity

To understand where this geometric control breaks down, we examine the visibility of the echoed Berry phase as a function of the traversal time, τ, and the Rabi frequency, Ω_R (Fig. 4.11). For a given Ω_R, we find a sharp decrease in the visibility where adiabaticity is completely lost for short τ. Likewise, gradual reduction in the visibility for longer τ is due to decoherence that increases the probability of cycling through $|A_2\rangle$ for a given iteration, thus obfuscating the Berry phase. As we increase Ω_R to

64 MHz, we achieve visibilities as high as 51% and adiabatic interaction times as short as $\tau \sim 250\,\text{ns}$. Faster adiabatic evolution is enabled by increasing Ω_R as the energy gap between dark and non-dark states expands. Modelling of these general trends using our four-state master equation approach is presented in §C.1.2. This geometric control with STIRAP represents a 100-fold speedup over the previous atomic demonstration [102].

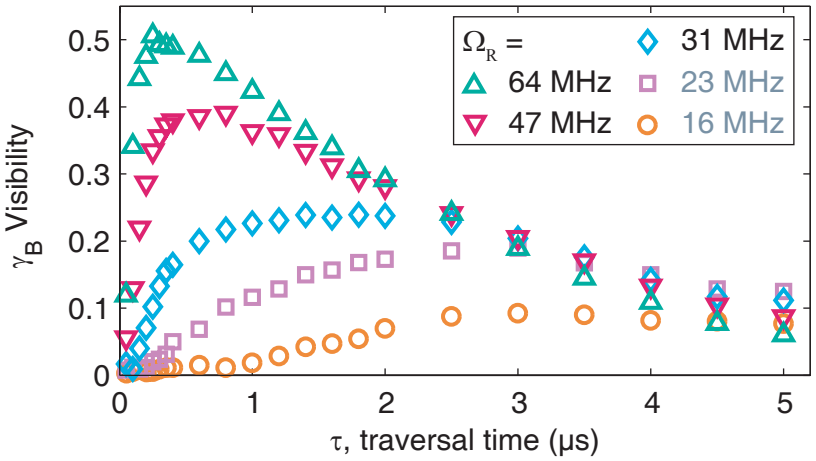

Figure 4.11: Berry phase visibility as a function of traversal time The visibility of the Berry phase, γ_B, as a function of traversal time, τ, for different Ω_R. A sharp turn-on for small τ indicates the adiabatic limit, while the gradual decrease in visibility for longer τ is due to accumulated excitation to $|A_2\rangle$. Errors are smaller than the point size.

4.4.2 Resilience of the Berry phase to noise

Furthermore, as the Berry phase arises from global geometric properties of the state evolution, it offers a degree of robustness to noises that act locally on the trajectory. To investigate, we introduce simulated noise

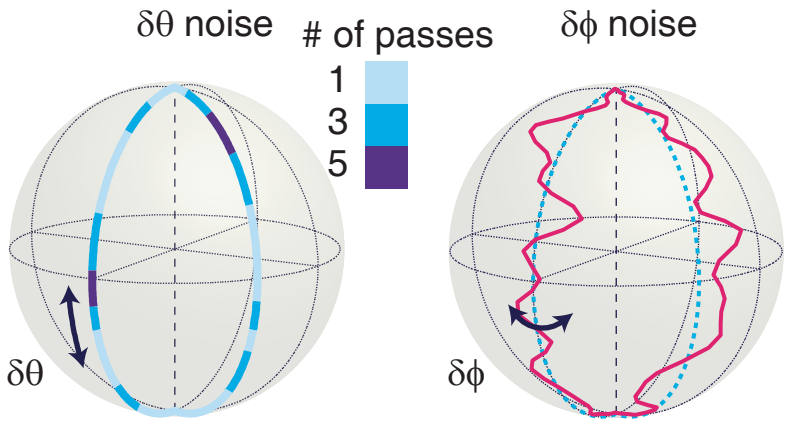

Figure 4.12: Types of simulated noise Illustration of $\delta\theta$ (left) and $\delta\phi$ (right) noise on Bloch sphere. $\delta\theta$ noise is parallel to the path and does not affect the enclosed solid angle, while $\delta\phi$ noise is perpendicular to the path and affects the enclosed solid angle.

onto the input parameters controlling the polar $\theta(t)$ and azimuthal $\phi(t)$ angles for our loops. The two types of noise, $\delta\phi(t)$, acting perpendicular to the ideal path, and $\delta\theta(t)$, acting parallel to the ideal path, physically correspond to fluctuations in the relative phase and amplitude, respectively, of the two laser fields controlling STIRAP (Fig. 4.12). We measure the standard deviation $\sigma_{\gamma B}$ of the distribution of Berry phases realized from 250 unique instances of noisy paths [91]. The noises conform to an Ornstein-Uhlenbeck process with a Lorentzian frequency bandwidth $\Delta\nu = 3\,\mathrm{MHz}$ and a Gaussian distribution of amplitudes with standard deviation s_i ($i = \theta, \phi$). In Fig. 4.13a, we plot the distributions (including broadening by photon collection statistics) arising from a noise amplitude of $s_\phi = 8°$ for ideal loops enclosing four disparate Berry phase angles. Likewise, in Fig. 4.13b, we plot the distributions arising from loops of the same intended

γ_B but with a noise amplitude of $s_\theta = 8°$. We find these distributions remain constant regardless of the intended Berry phase. This feature is conducive to practical protocols, as the sensitivity to noise fluctuations does not depend on the given Φ (§C.5.3), unlike other approaches [91, 97] where larger Berry phases are more susceptible to noise. This arises from the path-length preserving nature of our trajectories that are conveniently accessed by STIRAP.

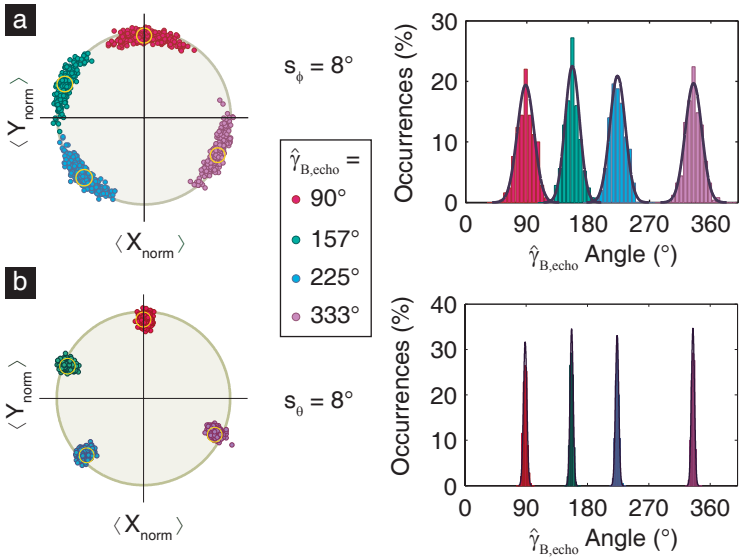

Figure 4.13: Berry phase distributions for different intended phases a) Angular distributions (broadened by photon collection statistics) of measured Berry phases for a specific noise amplitude, $s_\phi = 8°$, with intended phases: $\gamma_{B,echo} = 90°$ (red), 157° (green), 225° (blue), and 333° (purple), plotted on the equatorial slice of Bloch sphere (left) and binned into histograms with bin size of 6 (right). Projections are normalized by zero-noise case. **b)** Angular distributions of measured Berry phases for specific noise amplitude, $s_\theta = 8°$. Yellow circle, for a) and b), indicates the 95% confidence interval of photon collection shot noise about the intended γ_B. The width of the distributions is independent of the intended Berry phase.

In Fig. 4.14, we examine the impact of increasing the amplitude of the

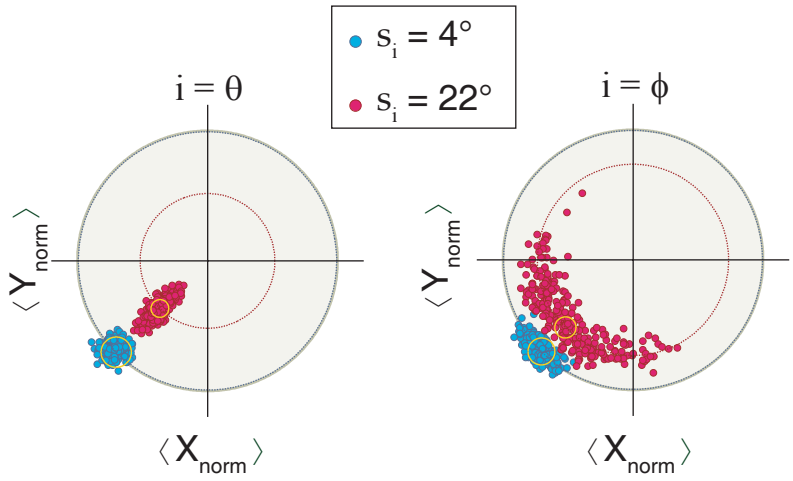

Figure 4.14: Effect of noise amplitude on Berry phase distributions Shot-noise broadened angular distributions of $\gamma_B = 225°$ for both $\delta\theta$ and $\delta\phi$ noise at noise amplitudes $s_i = 4°$ (blue) and 22° (red). Dashed circle indicates mean visibility, $\langle\sqrt{X^2 + Y^2}\rangle$, of the distribution for $s_i = 4°$ (blue) and 22° (red). The smaller magnitude of the visibility indicates fewer adiabatic loops are preserved.

two different types of noise. Consistent with the expectation that parallel noise does not change the enclosed solid angle, the Berry phase remains minimally dephased for increased $\delta\theta$ noise. However, larger noise amplitudes in $\delta\theta$ reduce the visibility as fewer adiabatic loops are preserved due to non-adiabatic changes introduced by the noise. In the case of perpendicular noise, $\delta\phi$, which modifies the enclosed solid angle, we see an enhanced effect on the distribution of Berry phases. Assuming the dark state adiabatically follows the noisy path, we derive an analytic relationship [90] between the variance in the Berry phase and the noise amplitude s_ϕ for

our specific trajectory (§C.5.3),

$$\sigma_{\gamma B}^2 = \frac{s_\phi^2}{2}\left(\frac{1-e^{-2\pi\Delta\nu\tau}}{(1+(\Delta\nu)^2)^2} + \frac{\pi\Delta\nu\tau}{1+(\Delta\nu)^2}\right). \tag{4.2}$$

This variance has no dependence on the wedge angle Φ, but only depends on the product $\Delta\nu\tau$, a measure of the number of noise oscillations per cycle. The same derivation predicts insensitivity to s_θ to first order. The intrinsic $\sigma_{\gamma B}$ can be estimated from the shot-noised broadened standard deviations $\hat{\sigma}_{\gamma B,echo}$ by subtracting the estimated photon collection shot noise contribution in quadrature and dividing by two to account for the two loops traversed in the echo measurement (§C.5.2). In Fig. 4.15a, we confirm that $\sigma_{\gamma B}$ is strongly robust to $\delta\theta$ noise, while its dependence on $\delta\phi$ noise matches well to the expected result $\sigma_{\gamma B} = 0.64 s_\phi$ from Eq. 4.2 (solid line) using the experimental parameters $\Delta\nu = 3\,\text{MHz}$ and $\tau = 1200\,\text{ns}$. In contrast to dynamic phase, adiabatic geometric phase becomes increasingly robust to noise as the traversal time increases, as can be seen in $\sigma_{\gamma B}^2 \to \frac{\pi s_\phi^2}{2\Delta\nu\tau}$ in the limit of $\Delta\nu \gg 1$. In Fig. 4.15b, we display the estimated $\sigma_{\gamma B}$ as a function the STIRAP traversal time τ for measurements at $\Delta\nu = 3\,\text{MHz}$ and constant noise amplitude $s_\phi = 14°$. These measurements clearly demonstrate the predicted $\sigma_{\gamma B} \sim \tau^{-1/2}$ scaling that is the hallmark of noise resiliency for geometric phases.

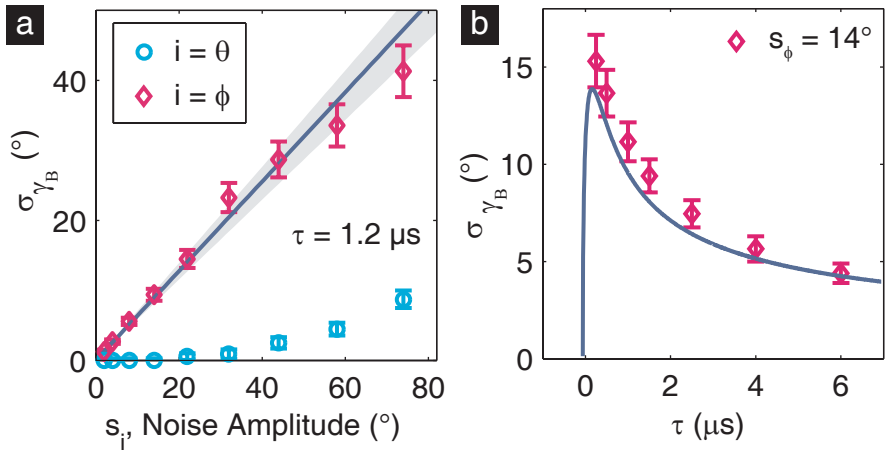

Figure 4.15: Relationship of the applied noise to the Berry phase distributions a) Estimated standard deviation, $\sigma_{\gamma B}$, of intrinsic distributions vs. noise amplitude s_i for both $\delta\theta$ (blue) and $\delta\phi$ (red). Grey shaded region is 95% confidence interval on the experimental slope. **b)** Estimated $\sigma_{\gamma B}$ showing a $\tau^{-1/2}$ decrease as the STIRAP traversal time, τ, increases for a constant noise amplitude $s_\phi = 14°$. Errors in a) and b) represent 95% confidence intervals. Indigo lines in a) and b) are the predicted behavior for $\sigma_{\gamma B}$ using experimental parameters and Eq. 4.2 of the main text.

4.5 Conclusions and discussion

We demonstrate an all-optical approach to accumulate Berry phase in a solid-state system that enables independent, geometric manipulatation of individual qubits with diffraction-limited spatial resolution. Using the $|A_2\rangle$ Λ system of the NV center in diamond, we control the adiabatic passage of a dark state, understand the mechanisms that limit the successful enclosure of Berry phase, and characterize the nature of its robustness to noise. Due to imperfect initialization and loss mechanisms, the experimental Berry phase visibilities peak at 51%, corresponding to an estimated peak state

fidelity of 73%; this fidelity could be improved in a more isolated Λ system allowing for higher optical driving powers (§C.1.4 and §C.1.5). Extensions to this technique could be realized by harnessing other solid-state Λ systems, such as in the silicon-vacancy (SiV) in diamond [106, 107] with its strong zero-phonon line emission, important for photonic applications [108]. Alternatively, adding another optical field to actively control the third ground state level (e.g. the reference level $|0_g\rangle$) in a solid-state tripod system provides an avenue for an all-optical set of universal geometric single qubit gates [93, 102, 103, 104]. The prevalence of Λ and tripod energy structures make these techniques extendable to a variety of solid-state qubits, including color centers [106, 107, 32, 109, 110], transition metal [111] or rare-earth ions [22, 112], and quantum dots [113], existing in materials [114] promising for a broad range of photonic technologies.

4.6 Methods

4.6.1 Experimental setup

The experiments in this work use an electronic grade diamond substrate purchased from Element Six, measuring $2 \times 2 \times 0.5$ mm. All NV centers present in the sample were naturally formed during the growth process. We lithographically patterned Ti:Au (10 nm Ti, 100 nm Au) short-terminated waveguides on the surface to provide on-chip microwave control of the NV centers. The sample is thermally sunk inside a liquid helium flow cryostat

held at 8 K. The short-terminated waveguide is wirebonded to a microwave line within the cryostat and connected to the signal generators via a coaxial port. The cryostat serves as the sample chamber for a confocal microscopy setup designed to study individual NV centers. The NV center studied had a natural optical linewidth of ≈ 100 MHz with an orbital strain splitting around 7.4 GHz. An applied external magnetic field of 117 G splits $|-1_g\rangle$ and $|+1_g\rangle$ by 655 MHz, and the combination of the natural strain and applied magnetic field split the $|A_2\rangle$ and $|A_1\rangle$ excited states by ≈ 2.9 GHz.

The confocal microscopy setup consists of a 532 nm laser to re-ionize the NV^- charge state and initialize to the $m_S = 0$ spin state, a tunable 637 nm laser tuned to the $|0_g\rangle \rightarrow |E_Y\rangle$ transition for readout of the spin state [38], and second tunable 637 nm laser fiber coupled to an electro-optic modulator tuned to the $|A_2\rangle$ transition for the STIRAP interaction. The electro-optic modulator is driven by a signal generator tuned to 655 MHz, the splitting of $|-1_g\rangle$ and $|+1_g\rangle$, creating sidebands on the laser to drive the Λ transitions. All lasers are controlled using acousto-optic modulators for nanosecond timescale pulsing. All three lasers pass through individual polarization optics, and are combined using beamsplitters and dichroic mirrors. The combined beam is eventually focused onto the sample using a 0.85 NA 100$\times$ objective that is aberration-corrected for the cryostat window. The red-shifted phonon sideband of the NV center's PL is spectrally filtered through a series of dichroic mirrors and bandpass filters and then

counted in a silicon avalanche photodiode. Those counts are binned via a series of logic switches, and then summed by either a time-correlated counting card (Fig. 4.4b) or a data acquisition card (all other figures).

In addition to the 655 MHz applied to the EOM, additional microwave frequencies are needed for characterization. For the Berry phase measurements (Figs. 4.7 - 4.15), a second signal generator provides on-chip microwaves tuned to 2.550 GHz, the splitting of the ground state $|0_g\rangle$ and $|-1_g\rangle$ levels. However, for the STIRAP path evaluation measurements (Figs. 4.3 - 4.5), three colors of microwaves are required. In this case, the second signal generator provides microwaves tuned to 3.205 GHz, the splitting of $|0_g\rangle$ and $|+1_g\rangle$, while a frequency mixer combines the two initial frequencies to provide the third frequency, 2.550 GHz, the $|0_g\rangle$ / $|-1_g\rangle$ splitting. To phase-control the microwaves, we use the internal IQ modulation functionality of both signal generators. All timing and pulse sequences (§C.3.2, §C.4.1, and §C.5.1) are controlled with a 1 GS/s arbitrary waveform generator.

4.6.2 Theoretical methods

The rotating frame Hamiltonian describing the Λ system and optical fields within the NV center level structure is:

$$H(t) = \frac{h}{2}\begin{pmatrix} 0 & 0 & 0 & 0 \\ 0 & 0 & 0 & \Omega_{-1}(t) \\ 0 & 0 & 2\delta & \Omega_{+1}(t)e^{i\phi(t)} \\ 0 & \Omega_{-1}(t) & \Omega_{+1}e^{-i\phi(t)} & 2\Delta \end{pmatrix}, \tag{4.3}$$

where the matrix representation is given in the basis $\{|0_g\rangle, |-1_g\rangle, |+1_g\rangle, |A_2\rangle\}$. The master equation in Lindblad form is given by:

$$\dot{\rho}(t) = -i[H(t), \rho(t)] + \sum_k \left(L_k \rho(t) L_k^\dagger - \frac{1}{2} L_k^\dagger L_k \rho(t) - \frac{1}{2} \rho(t) L_k^\dagger L_k \right). \tag{4.4}$$

where L_k denote the Lindblad operators descriping dissipative processes. These include experimentally estimated relaxation times from $|A_2\rangle$ to $|-1_g\rangle$ of ≈ 31 ns, $|A_2\rangle$ to $|+1_g\rangle$ of ≈ 24 ns, $|A_2\rangle$ to the reference state $|0_g\rangle$ of ≈ 104 ns, an orbital dephasing rate of 7 ns [34], and a fitted phenomenological spin dephasing rate of 2.25 µs. The optical fields in the simulation are described by $\Omega_R = 31$ MHz and $\Delta = 60$ MHz. See §C.1 and §C.2.2 for more details.

4.6.3 Berry phase

The dark state in our system is:

$$|D\rangle = \cos\left(\frac{\theta(t)}{2}\right)|-1_{\mathrm{g}}\rangle - \sin\left(\frac{\theta(t)}{2}\right) e^{i\phi(t)} |+1_{\mathrm{g}}\rangle \tag{4.5}$$

where $\theta(t) = 2\arctan(\frac{\Omega_{-1}(t)}{\Omega_{+1}(t)})$ and $\phi(t)$ is the phase relation between the driving fields. The total Berry phase accumulation over an adiabatic trajectory of a dark state is given by [104],

$$\gamma_B = i \int_{R_i}^{R_f} \langle D|\nabla_{\bar{R}}|D\rangle \cdot d\bar{R} \tag{4.6}$$

where the vector $\bar{R} = \binom{\theta}{\phi}$ describes the surface of the Bloch sphere. Substituting our dark state, the Berry phase simplifies to:

$$\gamma_B = -\oint \sin^2\left(\frac{\theta(t)}{2}\right) d\phi \tag{4.7}$$

where the integral is taken over the closed loop on the Bloch sphere. To determine the accumulation from our specific path, non-zero contributions to the integral only occur where the phase shift occurs, $\Delta\phi = \Phi$ at the $|+1_g\rangle$ pole, $\theta = 180°$, and $\Delta\phi = -\Phi$ at the $|-1_g\rangle$ pole, $\theta = 0°$. From this, we determine a Berry phase of:

$$\gamma_B = -\Phi \tag{4.8}$$

Chapter 5

Ultrafast optical probe of orbital and spin dynamics in the NV center

The following chapter is adapted from previously published work [34], and was largely the brainchild of Lee Bassett and F. Joseph Heremans. David Christle and I assisted in some experimental endeavors and analysis, and Guido Burkard provided the theoretical modelling. Further details can be found in the supplementary material to Ref. [34] online and F. J. Heremans' thesis [57]. These details are not reproduced in this thesis due to length considerations.

5.1 Ultrafast optical technique

Using the negatively charged diamond NV center as a model, we introduce a technique to probe the intrinsic structure of optically active spin systems

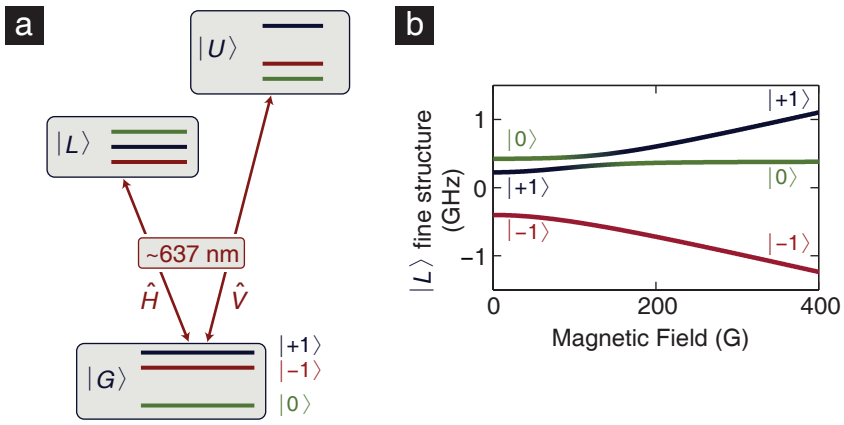

Figure 5.1: NV center optical transitions a) Schematic of the NV center's orbital and spin fine structure (B< 100 G). **b)** Spin sublevels in $|L\rangle$ calculated as a function of magnetic field applied along the NV-center's symmetry axis.

and control their dynamics using ultrafast optical pulses. Our scheme complements previous demonstrations of all-optical NV-center spin control using off-resonant laser fields [42, 55], but enables faster control by using picosecond optical pulses of light to resonantly excite the NV center. By combining time-domain control of these fast excitations with quantum tomography of the ground state (GS) spin, we demonstrate arbitrary, all-optical, coherent spin rotations and develop a technique to precisely map the excited state (ES) Hamiltonian, H_{ES}, through the coherent evolution it produces.

The spin-triplet/orbital-singlet GS of a negatively-charged diamond NV center is connected to a spin-triplet/orbital-doublet ES by dipole-allowed optical transitions that can be excited either resonantly (637 nm) or non-resonantly ($\approx 500 - 630$ nm). Crystal strain breaks the ES orbital de-

generacy, yielding two separated orbital branches ($|L\rangle$ and $|U\rangle$)[1] that are connected to the GS ($|G\rangle$) through orthogonal linear-polarization optical selection rules (Fig. 5.1a). Over multiple cool downs, we measured strain splittings between $|L\rangle$ and $|U\rangle$ in the range $\approx 10 - 20\,\mathrm{GHz}$. While phenomenological models successfully describe the NV center's overall electronic structure [27, 28], previous estimates of the parameters in the ES Hamiltonian H_{ES} based on spectroscopic measurements [33, 64] have limited precision (Table 5.1), and dynamical effects related to phonons, hyperfine coupling, and the ISC still lack a complete description.

We use a home-built confocal microscope to isolate single NV centers in an electronic-grade, synthetic diamond (ElementSix) that was irradiated with 2 MeV electrons ($10^{14}\,\mathrm{cm}^{-2}$) and annealed. A solid immersion lens milled using a focused ion beam [115] enhances the optical collection and excitation efficiencies, and nearby metal gates radiate microwave magnetic fields (Fig. 5.2). A frequency-doubled optical parametric oscillator pumped by a mode-locked Ti:Sapphire laser generates sub-picosecond optical pulses, a tunable diode laser ($\sim 637\,\mathrm{nm}$) enables resonant spin readout [38] and frequency-domain spectroscopy, and a 532 nm diode laser provides photoluminescence (PL) imaging and stabilizes the NV-center charge state [116].

[1]For the purposes of this chapter, the orbital branches $|E_Y\rangle$ and $|E_X\rangle$ are referred to as $|L\rangle$ and $|U\rangle$ for "lower" and "upper."

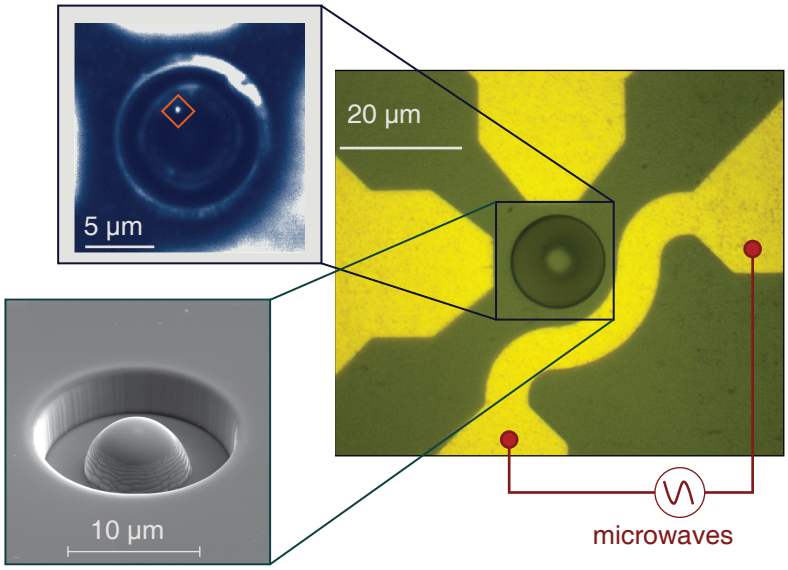

Figure 5.2: Solid immersion lens in diamond Optical micrograph (right) of our device consisting of metal surface gates used to generate microwave magnetic fields surrounding a solid immersion lens (SIL) milled from the diamond using a focused ion beam. Lower left: scanning electron micrograph of the SIL before gate fabrication. Upper left: Scanning confocal photoluminescence (PL) micrograph. The single NV center studied in this work is marked by a diamond.

We use ultrafast optical pulses to manipulate the NV center's orbital state in much the same way that microwave pulses rotate the GS spin. They affect only the orbital state directly, being effectively instantaneous from the perspective of the spin while preserving the spin coherence [117]. By tuning the polarization of the optical field, we can couple $|G\rangle$ to either ES orbital eigenstate, $|L\rangle$ or $|U\rangle$, or to a coherent superposition of the two [Supplemental of Ref. [34]]. We collect the PL in the red-shifted phonon side band (650-750 nm), which is proportional to the probability that the NV center was optically excited by a given operation. Figure 5.3 shows the

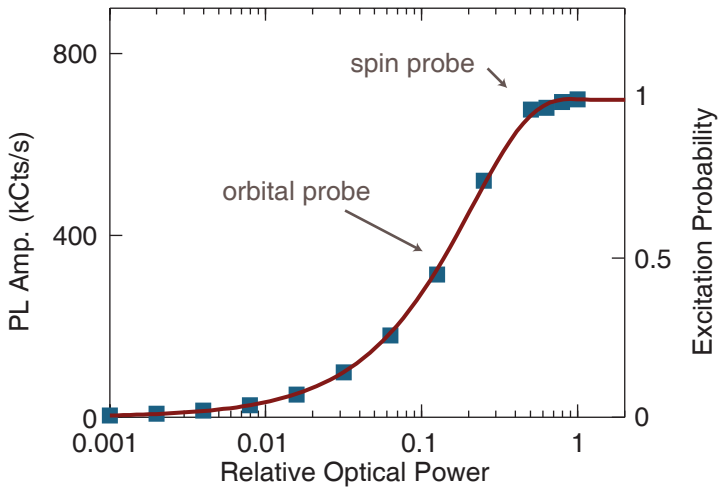

Figure 5.3: Optical excitation probability Spontaneous PL decay amplitude, and corresponding optical excitation probability of the NV center as a function of the power of a single ultrafast pulse (squares), and numerical simulations (16) using the measured pulse characteristics (red curve). Approximate settings used to probe orbital and spin coherence are marked by arrows.

measured excitation probability for individual pulses, P_{Ex}, as a function of the pulse energy, corrected for ionization effects (conversion of NV^{-1} to NV^{0}) that occur at higher pulse powers [Supplemental of Ref. [34]]. The excitation from $|G\rangle$ to the ES exhibits a coherent adiabatic passage behavior, manifested by saturation at P_{Ex}=1 at high powers, due to frequency chirp introduced by dispersive elements in the optical path. Numerical simulations of the orbital dynamics using the optical pulse waveform reconstructed through a nonlinear interferometric technique [118] confirm the observed power dependence [Supplemental of Ref. [34]].

5.2 Probing excited state orbital dynamics

In analogy with microwave spin resonance techniques, we probe orbital coherence using a two-pulse (Ramsey) scheme (Fig. 5.4a), where each pulse is tuned to excite the NV center with $P_{Ex} \approx 0.5$. A Mach-Zehnder interferometer splits each laser pulse into two identical copies, with a variable time delay set by an optical delay line in one leg [Supplemental of Ref. [34]]. The combination of a motorized stage for coarse positioning with a fine-control piezoelectric-mounted mirror provides variable delays between $0 - 4$ ns with sub-femtosecond precision, enabling the study of orbital coherence with timescales spanning six orders of magnitude.

Figure 5.4b shows sweeps of the femtosecond-scale relative delay ($\Delta\tau$) at two settings of absolute delay (τ) marked in Fig. 5.4c. The final excitation probability oscillates with a period of $\lambda/c = 2.1$ fs, where $\lambda = 637$ nm and c is the speed of light, reflecting the quantum coherence between the GS and ES orbitals. With the polarization tuned to couple $|G\rangle$ to a superposition of $|L\rangle$ and $|U\rangle$, we create a superposition state composed of all three orbital levels, and observe collapses and revivals in the Ramsey amplitude on picosecond scales indicative of coherent evolution within the ES orbital doublet manifold (Fig. 5.4c). These measurements are similar to quantum-beat spectroscopy techniques [119] used to probe ES molecular structure in gases, liquids, and solids.

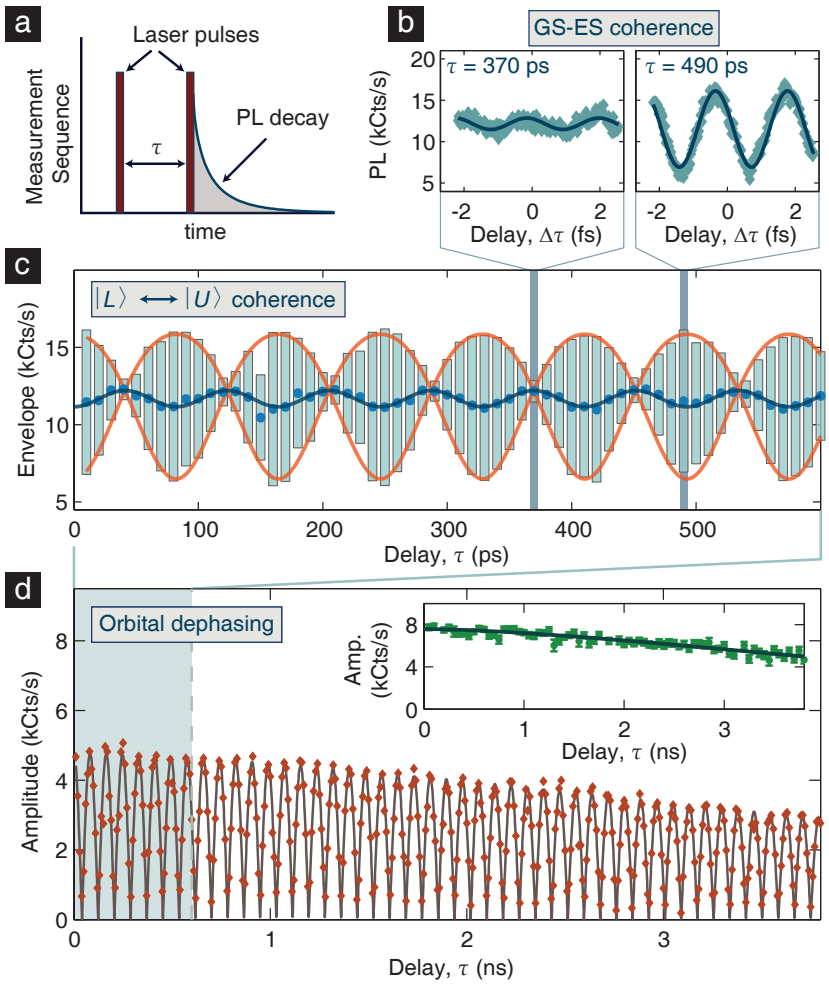

Figure 5.4: Orbital coherence measurements a) Schematic of optical pulse sequence used to probe orbital coherence. **b)** Optical excitation probability versus fs-scale relative delay ($\Delta\tau$) at the two points of absolute delay (τ) marked in c), with sinusoidal fits of the form $y_0 + Asin(\omega\Delta\tau + \phi)$, where $\omega/2\pi = 470$ THz is the optical frequency at 637 nm. **c)** Coherence envelopes from sinusoidal fits to individual $\Delta\tau$ scans as in c), when the excitation polarization couples equally to $|L\rangle$ and $|U\rangle$. Rectangles show the sinusoid extrema ($y_0 \pm A$), and blue points denote the offset y_0. Oscillations reflect coherent evolution within the ES orbital doublet. **d)** Coherence amplitude versus τ, extending the data in c) to nanosecond timescales (orange points), together with a corresponding measurement (inset) with the excitation polarization coupling only to $|L\rangle$ (green points). In both c) and d), solid curves show fits to functions described in (16).

Over nanosecond timescales (Fig. 5.4d), this approach enables orbital-selective, time-domain measurements of orbital dephasing and decoherence effects such as spectral diffusion and the dynamic Jahn-Teller effect [35]. For example, we measure different orbital dephasing times, $T_{orbital} = 7.1 \pm 0.3$ ns and 5.8 ± 0.4 ns for a two-component state,$\alpha|G\rangle + \beta|L\rangle$, and a three-component state,$\alpha|G\rangle + \beta(|L\rangle + |U\rangle)$, respectively [Supplemental of Ref. [34]], where α and β are complex amplitudes. This difference is not fully understood and needs to be explored further. The demonstration of time-domain orbital control also suggests extensions to multi-pulse dynamical decoupling sequences, potentially to improve the coherence of emitted photons to link distant NV centers [46].

5.3 Excited state spin dynamics for qubit control

The ability to coherently manipulate the NV center's orbital state on picosecond timescales provides new opportunities to control its electronic spin. Due to interactions (e.g., spin-orbit, spin-spin, strain) that depend on the electron's orbital wave function, the spin eigenstates of H_{ES} differ from those in the GS. Because the eigenstates set the basis for free evolution, ultrafast pulses can serve as gates to control the spin dynamics by coherently driving the system into different orbitals and abruptly changing the spin Hamiltonian. By fixing the length of time the spin evolves

within the ES manifold, we can produce a controlled spin rotation without microwaves.

5.3.1 Time domain quantum tomography

To demonstrate this effect, we first consider a qubit constructed from the GS subspace $\{|G,0\rangle, |G,+1\rangle\}$, optically excited to the ES subspace $\{|L,0\rangle, |L,+1\rangle\}$ for a short duration via optical pulses with polarization $\hat{H}$. Here, $|\epsilon, m_s\rangle$ denotes the $m_s \in \{0,+1,-1\}$ spin sublevel in the $\epsilon \in \{G,L,U\}$ orbital branch. Due to an ES level avoided crossing, or anti-crossing, between $|L,0\rangle$ and $|L,+1\rangle$ mediated by the spin-spin interaction (Fig. 5.1b), the ES spin eigenstates vary dramatically as a function of axial magnetic field, changing from "GS-like" S_Z eigenstates$\{|0\rangle,|+1\rangle\}$ far from the anticrossing to equal superposition states of $|0\rangle$ and $|+1\rangle$ at the center of the crossing. In a Bloch sphere representation of the qubit, the ES basis makes an angle θ_{ES} relative to the GS basis (Z axis), defining the rotation axis for coherent evolution in the ES. We probe the ES dynamics by performing time-dependent quantum tomography (TDQT) on the GS qubit as a function of the delay between two ultrafast pulses that excite and subsequently de-excite the NV center. Using microwave spin resonance pulses that maintain a constant (unspecified) phase relationship with the timing of the ultrafast pulses [Supplemental of Ref. [34]], we successively initialize the GS qubit, drive it to the ES for variable time, τ, and then

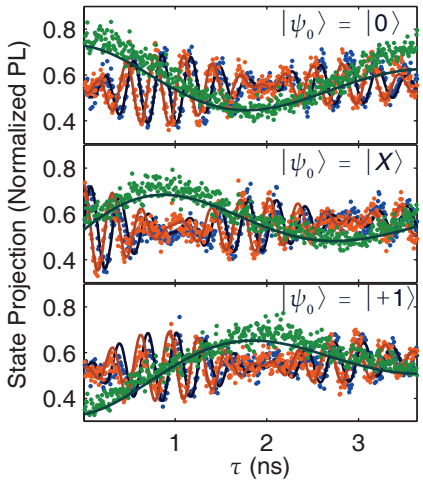

Figure 5.5: Time domain quantum tomography TDQT of the $|m_s\rangle = \{|0\rangle, |1\rangle\}$ GS qubit subspace as a function of the delay between two optical pulses coupling $|G\rangle$ to $|L\rangle$ near the anticrossing at B=110 G. Each panel shows the final $\langle X\rangle$, $\langle Y\rangle$, and $\langle Z\rangle$ projections (orange, blue, and green points, respectively) for a different initial state $|_0\rangle$ along with fits to our analytical qubit model as corresponding curves.

project it in one of three orthogonal axes on the Bloch sphere.

Figure 5.5 contains a few examples of TDQT measurements recorded at B = 110G, near the center of the anticrossing, where we expect $\theta_{ES} \approx \pi/2$. Indeed, the projection $\langle Z\rangle$ oscillates at a frequency $\approx$ 260 MHz, in agreement with the minimum frequency separation observed in optical frequency-domain spectroscopy (Fig. 5.6a). The fast oscillations observed in $\langle X\rangle$ and $\langle Y\rangle$ result from phase accumulation relative to the rotating frame of the microwave carrier resonant with the GS frequency at $f_{GS} = 3.18$ GHz. These data are quantitatively described by an analytic model based on a master-equation approach [Supplemental of Ref. [34]] that includes coherent ES spin evolution at frequency f_{ES} about a tilted

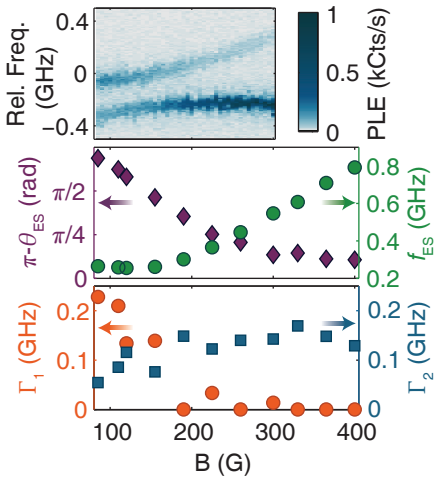

Figure 5.6: Tuning through the anticrossing a) Frequency-domain excitation spectroscopy versus B (same axis as **c**), showing the anticrossing between $|L,0\rangle$ and $|L,+\rangle$ around 110 G. **b)** Best-fit ES free evolution precession frequency (f_{ES}) and polar angle (θ_{ES}) from measurements at varied B. **c)** Best-fit decoherence rates ($_1$, $_2$) corresponding to population (T_1-type, orange triangles) and coherence (T_2-type, blue squares) relaxation in the ES, respectively. Uncertainties in b) and c) are similar to the symbol sizes.

axis with polar (azimuthal) angle θ_{ES} (ϕ_{ES}) together with decoherence effects due to incomplete optical inversion, spontaneous photon emission, the ISC, and both longitudinal (T_1-type) and transverse (T_2-type) relaxation processes in the ES, with rates $\Gamma_i = 1/T_i$. Best-fit curves are plotted with the corresponding data in Fig. 5.5.

5.3.2 Variable axis spin rotations

The best-fit parameters (f_{ES},θ_{ES}) and (Γ_1,Γ_2) from a global fit to eleven sets of TDQT data at different magnetic field values are shown in Figs. 5.6b and 5.6c, respectively. Within each set, ϕ_{ES} (not shown) depends

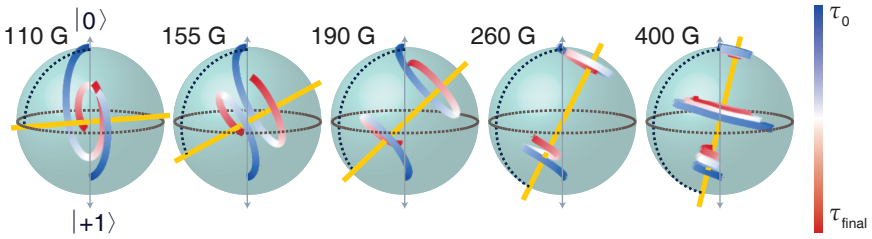

Figure 5.7: Unwound spin trajectories Best-fit trajectories in the lab-frame qubit Bloch sphere corresponding to TDQT measurements at different magnetic field values. The yellow axis in each plot shows the orientation of the ES eigenvectors relative to the GS, and θ_{ES} is indicated by dotted black lines.

on the unknown relative phase between the microwave carrier and the timing of the optical pulses. To clarify the dynamics, we "unwind" the phase accumulation from the GS rotating frame using the best-fit simulated density matrix, recovering the lab-frame trajectories of the qubit state as a function of evolution time in the ES. Several lab-frame trajectories are shown in Fig. 5.7 along with the rotation axes corresponding to the inferred ES eigenstates.

In principle, universal qubit control is possible with this scheme as long as $\theta_{ES} \neq 0$, in which case noncollinear rotation axes can be selected by varying ϕ_{ES} via the timing of optical pulse pairs. At the center of the anti-crossing the available rotation axes span the Bloch-sphere equator, enabling arbitrary single-qubit operations using a single pair of pulses. Here, the anticrossing coupling strength of 260 MHz generates an equatorial π-rotation in only 1.9 ns, approaching the fastest operation times demonstrated for

NV centers with microwave spin-resonance techniques [120]. The process fidelity [121] of this equatorial π rotation is 0.59, while the fidelity of a π rotation about a nearly polar axis at $B = 400$G (requiring only 160 ps in the GS rotating frame) is 0.77 [Supplemental of Ref. [34]]. The fidelities are limited by dephasing in the ES, the inter-system crossing, spontaneous photon emission, and incomplete optical inversion ($P_{Ex} \approx 0.9$ in our TDQT experiments). Given complete inversion, we calculate improved fidelities of 0.69 (equatorial) and 0.92 (polar), and further improvements should be possible by tuning f_{ES} and θ_{ES} through external magnetic, electric [45] or strain [33] fields. In principle, a tradeoff exists between direct excitation of the ES, which enables faster control, and off-resonant techniques [42, 55], which reduce sensitivity to ES dissipation mechanisms, but in practice, the reported fidelities are remarkably similar in both cases.

5.4 Mapping the excited state Hamiltonian

Besides demonstrating all-optical spin control, the technique presented in Fig. 5.7 provides a powerful approach to characterize the optically excited states of systems like the diamond NV center - namely, the ability to directly map H_{ES}, in this case specified by $(f_{ES}, \theta_{ES}, \phi_{ES})$, through TDQT measurements. In addition to H_{ES}, the time-domain approach also provides detailed information about dissipative dynamics typically obscured in frequency-domain spectroscopy, such as the decoherence rates Γ_1 and

Γ_2, which point to interactions with additional degrees of freedom. For example, the apparent increase in Γ_1 at low B in Fig. 5.6c actually results from coherent mixing with the third triplet state, $|L,-1\rangle$, outside our qubit model.

We can extend the TDQT technique to the full spin-triplet Hilbert space in order to map H_{ES} completely. Using phase-locked multicolor microwaves to address both the $|G,0\rangle \leftrightarrow |G,-1\rangle$ and $|G,0\rangle \leftrightarrow |G,+1\rangle$ transitions, we perform state tomography on the final spin triplet for a selection of prepared inputs states. Figure 5.8 shows a few example TDQT traces, detailing the evolution of the spin populations $\{|0\rangle, |+1\rangle, |-1\rangle\}$ for an initial state $|G,+1\rangle$ that is excited to $|L\rangle$ or $|U\rangle$, respectively, at B = 110G. By fitting these data to a numerical model, we extract the symmetry-allowed reduced matrix elements of H_{ES}, including intrinsic spin-spin/spin-orbit terms and perturbations due to external electric, strain, and magnetic fields [27, 28]. The model also includes spectral diffusion and phonon relaxation within the ES orbitals, ES spin dephasing, and a detailed description of the ISC, each parameterized by corresponding rates. The global fit to 54 TDQT time traces contains 31 free parameters, all of which are well constrained by the data. A full discussion of this model and fit can be found in the Supplemental of Ref. [34].

5.4.1 Extracting Hamiltonian parameters

Table 5.1 provides best-fit values for several intrinsic parameters in H_{ES} together with previous estimates based on frequency-domain spectroscopy [33, 64]. We find general agreement and improved precision, particularly for the spin-spin parameter Δ_2, whose value is confounded in frequency-domain measurements by strain perturbations. In contrast to frequency-domain techniques, TDQT distinguishes individual contributions from both intrinsic (spin-orbit/spin-spin) and external perturbations by their phases and amplitudes throughout H_{ES}. Essentially, we directly probe the ES eigenstates as well as the eigenvalues and can therefore fully map H_{ES} without varying any external fields. Furthermore, TDQT yields quantitative information about dissipative effects; for example, we resolve the ISC decay rates of individual ES basis states from other dephasing and decoherence processes.

Table 5.1: Excited state Hamiltonian parameters Intrinsic parameters of H_{ES} inferred from fitting our numerical model to TDQT measurements and comparisons with values from previous frequency-domain measurements. See appendices for parameter definitions.

Parameter	**Best-fit value**	**Literature value**	**Ref.**
Axial Spin-orbit (λ)	5.33 ± 0.03 GHz	5.3 GHz	[33]
Axial "ZZ" spin-spin (D_{ES})	1.44 ± 0.02 GHz	1.42 GHz	[33]
"XY" spin-spin (Δ_1)	1.541 ± 0.005 GHz	1.55 GHz	[33]
"XZ" spin-spin (Δ_2)	154 ± 13 MHz	200 MHz	[64]
Axial Landé g-factor ($g_{ES}^{\parallel}$)	2.15 ± 0.04	N/A	N/A

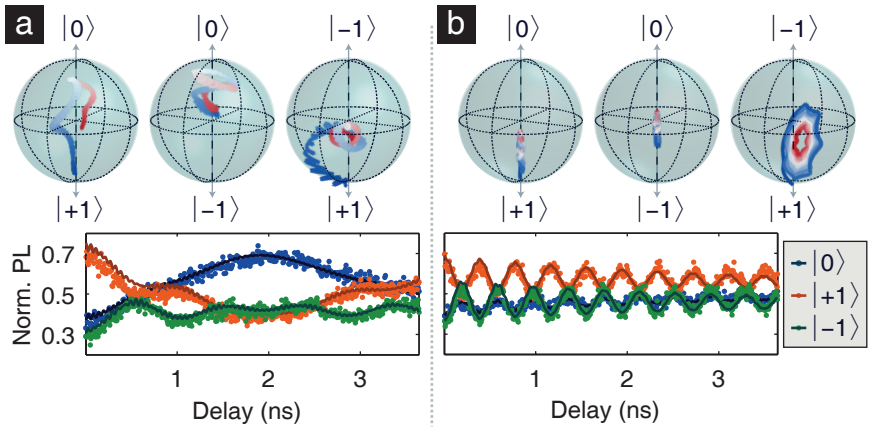

Figure 5.8: Mapping the excited state Hamiltonian a) Evolution of the GS spin initialized in $|G, +1\rangle$ and coupled to the $|L\rangle$ orbital branch by a pair of ultrafast pulses. Lower panel: measurements of the GS populations in $\{|0\rangle, |+1\rangle, |-1\rangle\}$ (blue, orange, and green points, respectively) as a function of the delay of the second pulse. Curves of corresponding colors result from a global fit to 54 different initialization/projection pairs, of which these three are a subset. Upper panel: Bloch spheres showing the best-fit lab-frame trajectories in three qubit subspaces. **b)** Same as a) but with the optical pulses coupling $|G\rangle$ to $|U\rangle$. All measurements were at B=110 G, near the anticrossing between the product states $|L, 0\rangle$ and $|L, +1\rangle$.

5.4.2 Spin triplet evolution

To visualize the spin evolution in triplet space, we use a set of Bloch spheres that span three qubit subspaces as shown in Fig. 5.8. As before, the best-fit trajectories are "unwound" from their corresponding rotating frames to reveal the ES dynamics in the lab frame. Due to spin-orbit effects, the spin evolution in $|L\rangle$ and $|U\rangle$ proceeds in different bases. The anticrossing in $|L\rangle$ drives oscillations between $|L, 0\rangle$ and $|L, +1\rangle$, while the states $|U, +1\rangle$ and $|U, -1\rangle$ are strongly mixed by spin-spin interactions. By direct extension of the qubit-control scheme developed above, this enables all-optical coherent

control spanning the full GS triplet, through the control of both the timings and polarizations of optical pulses.

5.5 Outlook

An alternative to the optical approaches presented in Chapters 3 and 4, this technique could similarly be used to address spins individually in spin arrays [83] or large-scale photonic networks [122]. By engineering appropriate orbital-dependent coupling between defects through, for example, optical, electrical, or mechanical interactions, the scheme could be extended to multi-qubit entangling gates, similar to ultrafast gate proposals for trapped ions [123, 124] and superconducting qubits [125]. Likewise, the TDQT technique can be applied to a broad range of atomic, molecular, and solid-state quantum systems, offering a powerful tool to characterize and control both new and established systems for future quantum technologies.

Chapter 6

Conclusion

In conclusion, we have demonstrated several approaches to couple and control individual solid-state spins using light. These demonstrations facilitate the development of a solid-state photonic network of qubits. In a photonic network of solid-state qubits, the photons act as flying qubits transferring quantum information from one stationary node, the NV center spin, to another. As such, harnessing and understanding the quantum optical interface between the spin and the light lays the foundation for the development of quantum repeaters and photonic networks of spins.

6.1 Linking spins with light

To begin, we demonstrated the ability to shift NV center optical transitions through the application of electric fields providing the opportunity to tune two separate NV center's transitions to degeneracy (Chapter 2). This experiment also revealed the surprising role that charge traps, such as sub-

stitutional nitrogens, play rectifying electric fields within the sample under photoexcitation. This procedure to tune NV center orbital transitions has been utilized in a number of other recent experiments linking NV center spins with light. One approach demonstrated dynamical stabilization and locking of NV center transitions on the timescale of several minutes [126]. Likewise, the ability to tune separate NV center optical transitions to degeneracy is a crucial element to interfere indistinguishable photons from separate NV centers' zero-phonon lines [43, 44]. The interference of indistinguishable photons from separate NV centers aided in the demonstration of heralded entanglement of two NV center spins separated by three meters [46], and furthermore, the teleportation of the electronic spin state of one NV center to the nuclear spin state of a distant NV center [47]. Such developments have been at the forefront of quantum information science over the past couple years, and show promise for the development of a quantum repeater and network.

6.2 Controlling spins with light

In addition to these developments aimed at the linking of NV centers through light, we have demonstrated several approaches to controlling the NV center electronic spin entirely with light. Typically, the NV center spin

is controlled through a combination of off-resonant optical[1] and microwave techniques to initialize, rotate, and read out the spin state. A fully optical approach obviates the use of microwaves and provides a smaller footprint of control, localized to a diffraction limit laser spot. With this smaller control field, individual qubits can be addressed within a photonic network [50] or spin array [83] without mutual interference of other qubits.

In this thesis, I described three different approaches to optical control. Two of the methods involve a Λ energy configuration and its resulting eigenstate, the dark state (Chapters 3 and 4), while the third approach derives control from the excited state dynamics (Chapter 5). The Λ system protocols develop and exploit the ability of the light fields to 'program' a particular dark state anywhere on the surface of the Bloch sphere. In Ch. 3, we demonstrated the ability to dictate any dark state basis of our choosing, leading to the ability to initialize, rotate, and readout within that basis. As a generalizable approach, elements of this technique have been extended and applied to other solid-state systems recently. Initialization into a coherent dark state through coherent population trapping has also been seen in individual silicon-vacancy centers in diamond [106, 107], ensembles of divacancies in silicon carbide [127], and a single cerium ion in yttrium aluminum garnet [112]. An extension of full Bloch sphere con-

[1]That is exploiting the spin-dependent polarization that results from cycling through the intersystem crossing.

trol of the dark state superposition was recently realized to demonstrate entangled absorption of a photon with the resulting NV center spin state [41]. In addition, readout along a bright/dark basis was recently performed in quantum dots [113]. Furthermore, the regime between stimulated Raman transitions (SRT) and stimulated Raman adiabatic passage (STIRAP) was recently explored in an NV center [23]. As a Λ system is a relatively abundant energy structure that can be found in a number of solid-state systems, these optical techniques provide a general approach to exploring qubit control in the solid state.

In Ch. 4, we demonstrated the adiabatic passage of a dark state (STIRAP) to accumulate a geometric phase, or Berry phase. As geometric phases rely only on the path in parameter space, and not on the energetics or time of the interaction, they offer a degree of robustness to noise that make them promising for fault-tolerant quantum information processing. As such, the Berry phases that we measure in the NV center may lead to the development of optical geometric gates in the solid state. Once again, these protocols, much like those in Ch. 3, rely only on the existence of a Λ system, and could be implemented in a wide array of potential systems. One potential extension of this demonstration is the addition of a third optical field to control another ground state, defined as a tripod system. This allows for geometric phases to accumulate not only between one level and a reference level (i.e. a Z-rotation on the Bloch sphere), but now be-

tween any chosen dark state and its complimentary bright state (i.e. any arbitrary axis on the Bloch sphere) [103, 104].

In Ch. 5, we demonstrated an alternative approach to optical control that exploited dynamics within the excited state manifold of the NV center. This approach not only demonstrated the ability to arbitrarily rotate the spin based on the eigenbasis of the excited state, but also provided an approach to probe the excited-state Hamiltonian through time-domain spectroscopy. This technique could be used to both characterize potential qubit systems, and aid in the development of techniques to control them.

6.3 Future directions

While these demonstrations have all been performed on one particular solid-state qubit, the NV center in diamond, they are not limited to just this one species of qubit. Relying on generalizable approaches, these optical control protocols anticipate future directions utilizing qubits perhaps more suited to photonic applications than the NV center. These include the negatively charged silicon-vacancy center in diamond, a spin-1/2 center whose emission is far more confined to its zero-phonon line ($\sim 80\%$) than the NV center ($\sim 3\%$) [128, 129]. As such, it has recently been used in demonstrations of coherent population trapping [106, 107], coupling to photonic crystals [108], and interference of indistinguishable photons [130].

Looking beyond diamond reveals a wide array of defects that may be

admirable qubits. Using the negatively charged NV center as a model, in combination with density functional theory, a series of criteria have been identified to find similar defects in other materials [29]. The divacancy in silicon carbide is one such defect as it is similar in structure to the NV center in diamond and can be coherently controlled [30]. As silicon carbide exists in many different forms, or polytypes, the divacancy can exhibit different characteristics based upon its particular host polytype including the ability to exist at inequivalent lattice sites within the same crystal allowing for coupling between inequivalent ensembles [31]. Ensembles of these divacancies can be electrically driven [131], mechanically tuned [132], coherently prepared through CPT [127], and coupled to photonic crystals [133]. Recently, individual instances of divacancies have been isolated and coherently controlled exhibiting millisecond-long coherence times [32], opening up a wide array of possibilities for their use as qubits. Likewise, another defect in silicon carbide, the silicon-vacancy center, has similarly been isolated [109]. Another promising material for defects similar to the NV center is zinc oxide, in which single defects have also been identified [110].

Transition metal and rare-earth ions represent another pathway to developing single solid-state qubits for photonic networks. In particular, a variety of rare-earth ions in crystals have been used to demonstrate a number of important protocols for quantum information processing. Nuclear

spins of europium ions in yttrium orthosilicate exhibit coherence times as long as six hours [134], while entanglement between a photon and an atomic excitation of neodymium in yttrium orthosilicate has been demonstrated [135]. Additionally, as mentioned above, CPT has been used to prepare a dark state superposition of the spin sublevels within an individual cerium ion in yttrium aluminum garnet [112]. Transition metals in crystals similarly are an enticing route, which along with rare-earth ions, may represent the existence of coherently addressable Λ systems in ambient conditions. In particular, coherent population trapping has been observed at room temperature in chromium ions in ruby [111].

Myriad possibilities abound to study light-matter interactions in crystal defects. As such, accessing this quantum optical interface to control a wide array of potential defect-based qubits anticipates a bright future for quantum information processing.

Appendix A

Confocal microscopy

A.1 Confocality and NV center excitation

To study NV centers, as well as other point defects in semiconductors, we use home-built laser scanning confocal microscopes. The advantage to confocal microscopy over conventional microscopy is the ability to isolate a much narrower focal plane than is found in a standard microscopy setup. This prevents any light (fluorescence, photoluminescence, etc.) from deeper or shallower planes from impacting the focal plane of interest by the addition of background light. To accomplish this, a "pinhole" is placed at the focus of the collection lens eliminating out of focus images. In our case, the pinhole is a narrow-core fiber that carries the NV center photoluminescence (PL) to a silicon avalanche photodiode (APD), which converts photon counts into voltage pulses. These pulses are then binned and counted by either a National Instruments Data Acquisition Card (DAQ), or a FAST

ComTec P7889 multiple event time digitizer.

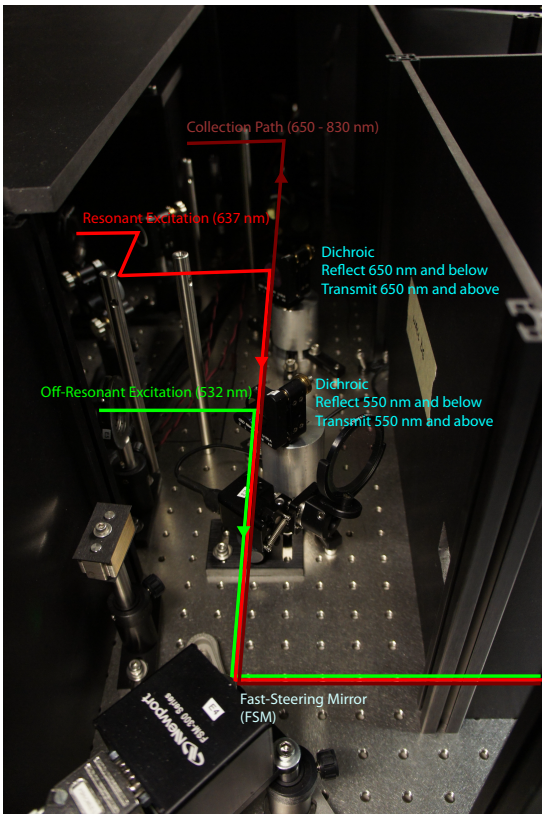

Figure A.1: Combining the excitation paths via dichroic mirrors A schematic of how the two excitation paths are combined through a series of dichroic mirrors. The resonant excitation (637 nm) is introduced into the combined excitation path by a dichroic that reflects 650 nm and below. The off-resonant excitation (532 nm) joins the combined path with another dichroic that reflects 550 nm and below. After the combined excitation excites the NV center, the photoluminescence from the NV center travels back through the combined path and the portion of the NV red-shifted phonon sideband above 650 nm passes through both dichroic mirrors and into the collection path.

In our experimental setups, we excite the NV center using both off-resonant 532 nm (green) laser light, as well as a 637 nm (red) laser tunable across the NV center optical transitions. The NV center then emits PL

in both its zero-phonon line (ZPL) and the red-shifted phonon-broadened sideband from $637 - 800$ nm. In order to separate the excitation wavelengths and the PL wavelengths, we use a series of dichroic mirrors. These mirrors transmit the PL of interest, while reflecting the excitation. To introduce the 637 nm resonant laser path, we first use a dichroic that reflects wavelengths lower than 650 nm, and passes wavelengths higher. We then use a second dichroic to combine the 532 nm excitation path with the resonant path, which passes wavelengths higher than 550 nm, and reflects those lower, allowing the green and red to be collinear when exciting the NV center, as seen in Fig. A.1.

A.2 Imaging the Diamond

The collinear path is then reflected off of a Newport fast-steering mirror (FSM), which introduces angular deflections into the path. These angular deflections are used to scan the surface of the sample, in order to generate a 2D plot at a certain depth within the diamond sample. However, to do so, these angular deflections need to remain on the back of the objective. We introduce an imaging pair of lenses between the fast-steering mirror and the back of the objective. Without this imaging pair between the FSM and the objective, small angular deflections result in large lateral deflections of the beam over any appreciable distance. Instead, the imaging pair creates an image of the FSM on the back of the objective (and vice versa, an image

of the back of the objective on the FSM). This allows for the small angular deflections to result in very small lateral shifts ($\sim$ 200 nm) of the beam when focused onto the sample by a 100x objective. By rastering the beam across the sample, we extract an image of the surface.

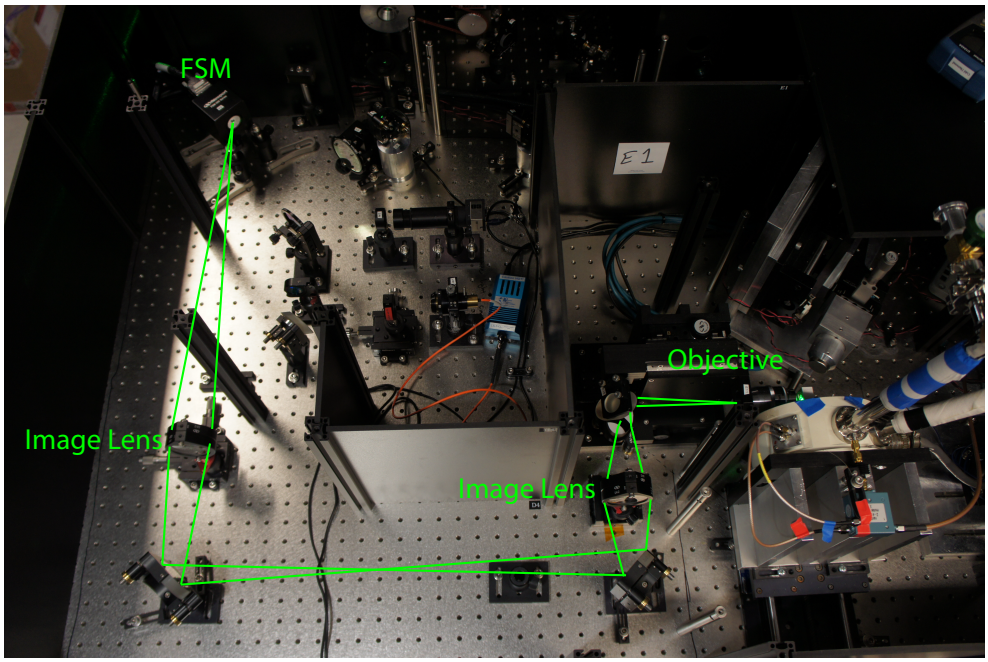

Figure A.2: The imaging path A schematic of the imaging lens to image the back of the objective on the fast-steering mirror, allowing for angular deflections of the mirror, and excitation path, to correspond to very small ($\sim$ 200 nm) on the surface of the diamond.

The imaging pair is separated by the sum of their focal lengths. If their foci, f_i are matched such that $f_1 = f_2 = f$, this corresponds a separation of $2f$, while the distance between the FSM and the objective should be $4f$, in order for the FSM and objective to image one another. A matched imaging pair can then be placed anywhere between the FSM and objective.

However, in the case of a non-matched pair, which is used to magnify the images, the placement of the imaging pair between the FSM is less trivial, requiring consideration of the ray optics. Note that this imaging pair should be achromatic, allowing for not only the excitation frequencies (532 nm and 637 nm), but also the NV center fluorescence ($650 - 800$ nm) to focus at similar points. The imaging path in the current version of the setup is shown in Fig. A.2.

The resulting PL from the NV center travels back through the path described, but now passes through the dichroics, only passing the PL that is 650 nm or longer in wavelength, and into the collection path. This means that we collect a significant portion of the phonon sideband emission, but not the ZPL, as we already excite along that transition for our resonant optical studies[1]. Here, the PL is focused through the collection lens into a narrow core fiber ($25 - 62$ μm), and measured by the APD.

The placement of the collection lens is sensitive, and if misplaced, can either cause collection of additional emission outside of the intended confocal plane, or overall reduced emission from the plane of interest. Typically, the lens is positioned on a motorized stage, and its position is set to optimize the signal-to-noise ratio of the PL from an individual NV center, such

[1]If we wanted to collect the ZPL, we would have to cross-polarize the resonant excitation with the collected ZPL. The dichroic would be replaced with a polarizing beam splitter, and additional polarization optics would be needed to fully extinguish any excitation light leaking into the collection path.

that the light from the proper focal plane is focused into the fiber. This lens also should be an achromatic doublet to prevent different frequencies of light having different focal lengths.

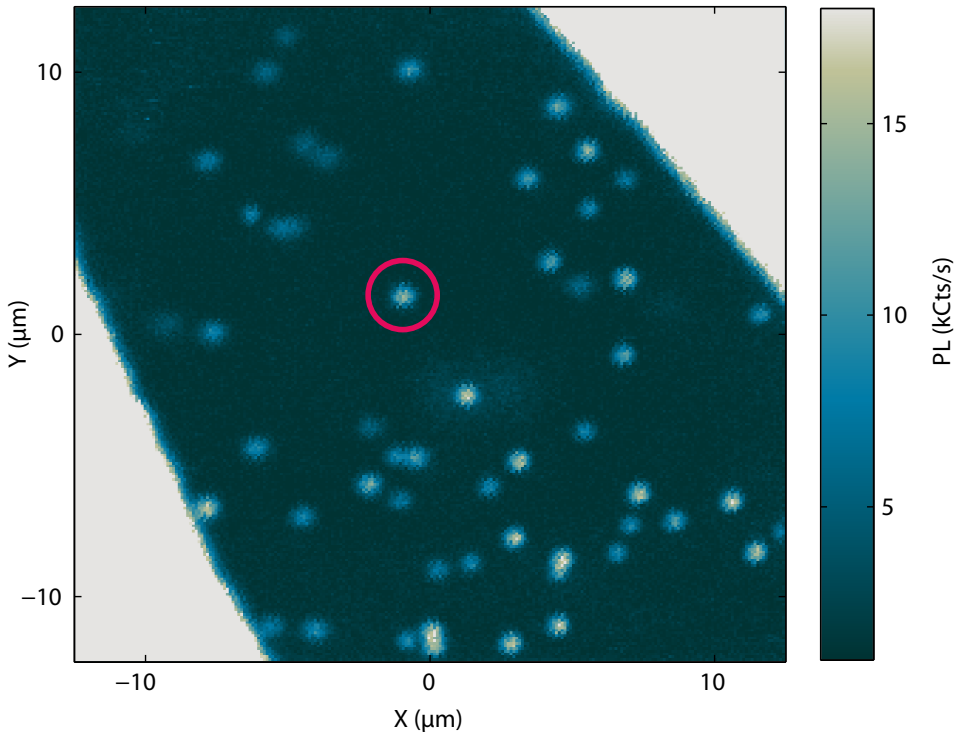

Figure A.3: A constellation of NV centers in an electronic grade diamond sample A rastered image of the surface of an electronic grade diamond sample. The bright spots correspond to PL emitted by individual NV centers. The PL spot circled in red is from the NV center used in Ch. 4

As we raster the FSM across the surface, and measure the resulting photoluminescence, we end up with plot similar to the one shown in Fig. A.4. This scan is from the diamond sample used in the Berry phase work. The bright spots correspond to the photoluminescence from a variety of individual NV centers roughly 5 µm below the surface. Circled in red is

the NV center used in the Berry phase work.

Appendix B

Supporting data for Chapter 3

B.1 Experimental details

A schematic of our confocal setup is provided in Fig. B.1 that incorporates a continuous wave (CW) green diode laser (532 nm), two CW tuneable red (637 nm) diode lasers with optional sideband wavelengths generated via electro-optic phase modulators (EOMs), NV center photoluminescence (PL) collection ($650 - 800$ nm) via an avalanche photodiode, and on-chip microwave electron spin resonance techniques (ESR) all gatable in time. All timing sequences used were programmed into an arbitrary waveform generator and are described later in this Appendix.

While the effects presented in Ch. 3 were observed in multiple NV centers, care was taken to select an NV center that had several desirable properties. We chose an NV center with a reasonable T_2^* time ($\sim$1 μs) due to the finite duration of the CPT/SRT/DBP pulses. Because the

energy separation between $|R_{e1}\rangle$ and $|L_{e1}\rangle$ Λ systems was quite small ($\delta_{e1}/h = 0.18$ GHz), it was desirable to choose an NV center with a narrow inhomogeneously-broadened optical linewidth (0.05 GHz FWHM for the NV center presented). We also chose an NV center that had a transverse strain splitting which varied between 4.6 GHz and 5.8 GHz as measured between the two orbital $m_s = 0$ spin sublevels. The variations in this NV center's strain occurred between cooldowns due to thermal cycling of the cryostat. The strain was in a range which allowed us to produce an avoided

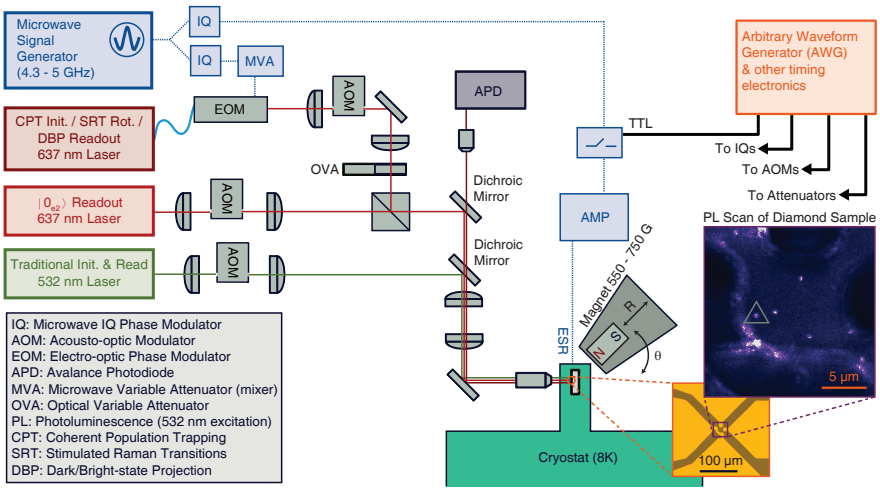

Figure B.1: Schematic of experimental setup Diagram detailing the optical excitation paths and photon collection path along with the microwave electronics, timing electronics, cryostat, and magnetic field as described in Methods. A PL scan of the region 6 μm below diamond surface, where the NV centre investigated is located (within the smoke-colored triangle). A short-terminated on-chip waveguide wire used to apply microwave ESR pulses for ground state spin manipulation is visible in the lower left. Deposited metallic pads on the right and top of the image are for applying dc voltages to the sample to affect the orbital splitting of NV center if necessary, but were not used in the present experiment.

level crossing (anticrossing) in the lower excited state orbital branch between the $m_s = 0$ and $m_s = +1$ spin sublevels with the application of an external magnetic field along the N-V axis, $(550 - 750$ Gauss). The resulting ground state spin splitting at these magnetic fields was relatively high ($\delta_{GS}/h = 4.3 - 5$ GHz) allowing for the EOM sidebands to be widely spaced, meaning the unused laser harmonics generated by the EOM were far from any NV center resonances.

It is also possible to generate an anticrossing in the upper excited state orbital branch but the resulting anticrossed eigenstates are much closer together in energy, making it prohibitively difficult to couple to an individual resonance. Off-axis magnetic fields could be used to increase the splitting between anticrossed levels, but they would also reduce the spin-selectivity of the intersystem crossing (ISC) used for comparison to the CPT-based readout.

In order to fully control the phase and amplitude of the CPT laser system, we adjust properties of the microwaves driving the EOM. To adjust the dynamic phase between the two used light fields, we control the phase of the ω_{mw} microwaves driving the EOM with an IQ modulator, which moves the dark state azimuthally about the rotating-frame Bloch sphere. We adjust the relative amplitude of the two used laser driving fields by varying the microwave power driving the EOM using a mixer, allowing us to adjust the polar position of the dark state on the Bloch sphere. While

the relative amplitude of the two resonant optical fields adjusts as expected, the summed amplitude of the two Λ-resonant sidebands also changes. This is because the EOM splits light at ω_L into several harmonics (of which we only select two) separated by ω_{mw}, with amplitudes of the harmonics being a function of the amplitude of EOM microwave driving power in the form of a Bessel function. To correct for this, we use an optical variable attenuator to compensate for this overall amplitude variance to within an order of magnitude in an attempt to keep Ω (Fig. 3.1) fixed. In addition, the overall frequency of the tunable laser, ω_L, would drift with respect to the Λ transitions, and due to the small separation in the anticrossing between $|R_{e1}\rangle$ and $|L_{e1}\rangle$, $\delta_{e1}/h = 0.18\,\text{GHz}$, we needed to occasionally recenter the laser frequency to the appropriate tuning on the order of every 10 minutes with 0.02 GHz laser frequency resolution.

B.2 Quantum state tomography of arbitrary initialization and rotation

In order to analyze our initialization and control protocols, we performed Bayesian quantum state tomography to characterize the various process output states and compute the corresponding fidelities found in Ch. 3. This approach allows for an accurate statistical inversion of repeated projective measurements that are subject to both stochastic and systematic error. In contrast to maximum likelihood estimation, this approach always yields

both point estimates and corresponding error bars that are physical for states near the boundaries of the allowed state space; moreover, it relaxes the assumption of asymptotic normality, achieving consistent estimates in the face of a finite number of measurements [85].

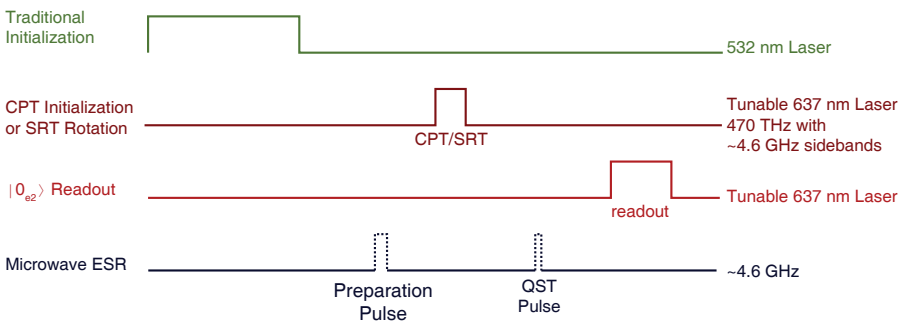

Figure B.2: Pulse sequence for arbitrary initialization and rotation The above pulse sequence was used for the data presented in Figs. 3.3, 3.4, 3.5, 3.6, 3.7, and 3.11. All experiments investigating these protocols consisted of $\sim 10^6$ iterations of this pulse sequence to achieve a sufficient signal-to-noise ratio.

To individually study CPT or SRT, the NV center spin state is first prepared using non-resonant 532 nm laser light to both mitigate photoionization and polarize the NV center ground state spin into $m_s = 0$ via ISC decay with roughly 75-80% fidelity [39, 136]. The state is then prepared on various places of the Bloch sphere with an ESR "preparation pulse" before either a CPT or SRT red laser pulse polarizes or rotates the spin, respectively. After the red laser, an additional ESR "QST" pulse is applied to rotate the X, Y, or Z spin projection onto the $|0_g\rangle/|+1_g\rangle$ readout measurement basis, phase-synced with the microwaves driving the EOM.

The timing of this QST pulse is chosen to coincide with the constructive rephasing of the three ^{14}N hyperfine Larmor frequencies, corresponding to a delay of 450 ns. Alternatively, a π-pulse can be added before the QST pulse to induce an echo of the spin coherence rather than use this rephasing. Finally, the spin state is read out along this basis by measuring PL intensity during a single-color red laser resonant with the $|0_g\rangle/|0_{e2}\rangle$ cycling optical transition [38].

As a normalization, the state is more fully initialized into $|0_g\rangle$ (or $|+1_g\rangle$) after 532 nm excitation by subjecting the spin to 637 nm laser light for 1 µs resonant with the opposite $|+1_g\rangle$ (or $|0_g\rangle$) spin state and one of the Λ systems. This scheme depletes the aforementioned optically-driven sublevel in the ground state and populates its counterpart $|0_g\rangle$ (or $|+1_g\rangle$). The readout contrast, $\mathcal{C}$, between the $|0_g\rangle$ and $|+1_g\rangle$ sublevels increases from about 62% from ISC spin polarization alone to about 84% after this purification. Because none of the CPT (or SRT) interactions appeared in practice to polarize the state beyond this level, this purified contrast serves as a consistent normalization for each state reconstruction and fidelity.

To begin our analysis, in terms of the density matrix, $\hat{\rho}$, the expecta-

tions are

$$\langle \mathrm{X} \rangle = \mathrm{Tr}\left(\sigma_z U_{\mathrm{Y}_{-\frac{\pi}{2}}} \hat{\rho} U^{\dagger}_{\mathrm{Y}_{-\frac{\pi}{2}}}\right)$$
$$\langle \mathrm{Y} \rangle = \mathrm{Tr}\left(\sigma_z U_{\mathrm{X}_{\frac{\pi}{2}}} \rho U^{\dagger}_{\mathrm{X}_{\frac{\pi}{2}}}\right)$$
$$\langle \mathrm{Z} \rangle = \mathrm{Tr}\left(\sigma_z \rho\right),$$

while the expected fluorescence levels (in photon counts) are defined by the resonant laser normalizations,

$$\langle \mathcal{F}_{\langle \mathrm{X} \rangle} \rangle = \mathcal{F}_{|0_g\rangle}\left(1 - \frac{\mathcal{C}}{2}\right) + \mathcal{F}_{|0_g\rangle}\frac{\mathcal{C}}{2}\langle \mathrm{X} \rangle$$
$$\langle \mathcal{F}_{\langle \mathrm{Y} \rangle} \rangle = \mathcal{F}_{|0_g\rangle}\left(1 - \frac{\mathcal{C}}{2}\right) + \mathcal{F}_{|0_g\rangle}\frac{\mathcal{C}}{2}\langle \mathrm{Y} \rangle$$
$$\langle \mathcal{F}_{\langle \mathrm{Z} \rangle} \rangle = \mathcal{F}_{|0_g\rangle}\left(1 - \frac{\mathcal{C}}{2}\right) + \mathcal{F}_{|0_g\rangle}\frac{\mathcal{C}}{2}\langle \mathrm{Z} \rangle.$$

We treat each of the data, D_k, as subject to normal error σ_k from the model prediction $\langle F \rangle_k$ whose other parameters ($\mathcal{F}_{|0_g\rangle}$, $\mathcal{C}$, and those described below) are contained in a vector $\mathbf{X}$ such that

$$\mathrm{prob}\left(\mathbf{D}|\hat{\rho}, \sigma_k, \mathbf{X}\right) = \prod_k \frac{1}{\sqrt{2\pi}\sigma_k} \exp\left(-\frac{\left(D_k - \langle F \rangle_k\right)^2}{2\sigma_k^2}\right). \tag{B.1}$$

Because of shot noise, the lower limit to σ_k is about $\sqrt{\langle F \rangle_k}$ but due to both the drift of the laser and stage mechanics, σ_k was about a factor of two to five larger in practice. To capture this uncertainty in the expected mismatch, we set

$$\mathrm{prob}\left(\sigma_k|\overline{\sigma}_k\right) = \frac{2\overline{\sigma}_k}{\sqrt{\pi}\sigma_k^2} \exp\left(-\frac{\overline{\sigma}_k^2}{\sigma_k^2}\right), \tag{B.2}$$

so that we marginalize each σ_k around a region of order $\overline{\sigma}_k$, expressing that σ_k should be on the order of, but not necessarily equal to, $\overline{\sigma}_k$; this

sort of construction makes our estimation statistically robust against data of unusually large drift (outliers). After performing the integration over all positive σ_k, we have that

$$\text{prob}\left(\mathbf{D}|\hat{\rho},\bar{\sigma}_k,\mathbf{X}\right) = \left(\sqrt{2}\pi\overline{\sigma}_k\left(1+\frac{\left(D_k-\langle F\rangle_k\right)^2}{2\overline{\sigma}_k^2}\right)\right)^{-1}. \tag{B.3}$$

In our analysis, we set $\bar{\sigma}_k = 2\sqrt{\langle F\rangle_k}$. This likelihood is also used for normalization parameters $\mathcal{F}_{|0_g\rangle}$ and $\mathcal{C}$ in the posterior probability density to infer them simultaneously with the axial projections and systematic errors.

In addition to the random noise of the experiment, the microwave pulses used to rotate the X and Y components to the Z axis for readout suffer from small systematic errors in their relative phase, which creates an offset from the proper rotation axis, and also in their duration, which creates an offset from the proper rotation length. The unitary operators above thus deviate from the ideal case and can be redefined, following Dobrovitski *et al.* [137], by

$$\begin{aligned} U_{\mathrm{X}_{\frac{\pi}{2}}} &= \exp\left(-i\left(\vec{n}_{\mathrm{X}}\cdot\vec{\sigma}\right)\left(\frac{\pi}{2}+2\phi\right)\right) \\ U_{\mathrm{Y}_{-\frac{\pi}{2}}} &= \exp\left(-i\left(\vec{n}_{\mathrm{Y}}\cdot\vec{\sigma}\right)\left(-\frac{\pi}{2}+2\theta\right)\right), \end{aligned}$$

where $\vec{n}_{\mathrm{X}} = (1,\epsilon_y,\epsilon_z)\,/\left(1+\epsilon_y^2+\epsilon_z^2\right)^{1/2}$, $\vec{n}_{\mathrm{Y}} = (v_x,1,v_z)\,/\left(1+v_x^2+v_z^2\right)^{1/2}$, and $\vec{\sigma}$ is a vector composed of the Pauli matrices. Here, the ϵ and v terms are the axial offsets and ϕ and θ are the length offsets, all of which are measured in units of angle. From calibration of the IQ modulator and

the discrete nature of the delay generator that governs the length of the pulses, we estimate that these factors are at most 5° in angular error and somewhat conservatively set the prior densities for each of these terms as a normal density of mean zero and standard deviation of 5°. The effect of this correction is most noticeable from the fact that the X and Y axis projection estimates almost always have larger uncertainties than the Z axis estimate.

Lastly, we use the non-informative reference prior [138] for the density matrix,

$$\text{prob}\,(\hat{\rho}) = 0.00513299\left(1-r^2\right)^{-1/2}\left(\log\left[\frac{(1-r)}{(1+r)}\right]\right)^2 \sin\theta, \qquad \text{(B.4)}$$

where r and θ are the standard spherical coordinates for the Bloch vector used to parameterize $\hat{\rho}$. As expected, given the large quantity of data collected, the choice of prior had no discernable effect on our inferences.

To obtain the marginal densities used for the point estimates and error bars of the projections and fidelities found in the main text, we use MT$-$DREAM$_{\text{ZS}}$, a Markov Chain Monte Carlo technique, to sample from the 11-dimensional posterior probability density [139]. This technique uses multiple random walk chains of a multiple-try Metropolis-Hastings rule [140] applied to an adaptive proposal distribution generated from past samples to generate new samples in accordance with the posterior probability density. We found the chains to have fast convergence and good mixing properties, and the corresponding sampler output to have low au-

tocorrelation using four independent chains and a multiple-try parameter of seven. The fidelities for experimental data are obtained by calculating the fidelity between the Bloch vectors from the random walk sampler and an ideal vector of unit length pointing along the same axis as the corresponding random walk sample. In this way, the fidelity is computed with respect to a perfect rotation of the state generated from the resonant laser pumping scheme described above. The point estimates of the projections and fidelities are the mean of the respective marginal densities while the error bars are the highest posterior density 68.2% credible intervals [141].

In Figs. B.3, B.4, and B.5, we present the corresponding X, Y, and Z projections for the rotating-frame Bloch spheres describing arbitrary initialization via CPT presented in Ch. 3, as well as some additional sets of projections and Bloch spheres not presented. As described in Ch. 3, all of these qubit Bloch spheres are within the $\omega_{mw} = \delta_{GS}/\hbar$ rotating frame. This is because our standard qubit states $|0_g\rangle$ and $|+1_g\rangle$ are separated in energy by δ_{GS}, and so each spin state precesses at the Larmor precession frequency of $\delta_{GS}/\hbar$. By reading out the X, Y, and Z projections with ESR pulses phase-matched relative to the same $\omega_{mw} = \delta_{GS}/\hbar$ angular frequency, we capture a snapshot of a fixed point on this rotating-frame sphere. Conversely, in a system where the qubit states are not energy split, the Bloch sphere would not be precessing. A CPT initialization laser pulse length of 200 ns is used for Figs. B.3, B.4, and B.5. In some instances, noted below,

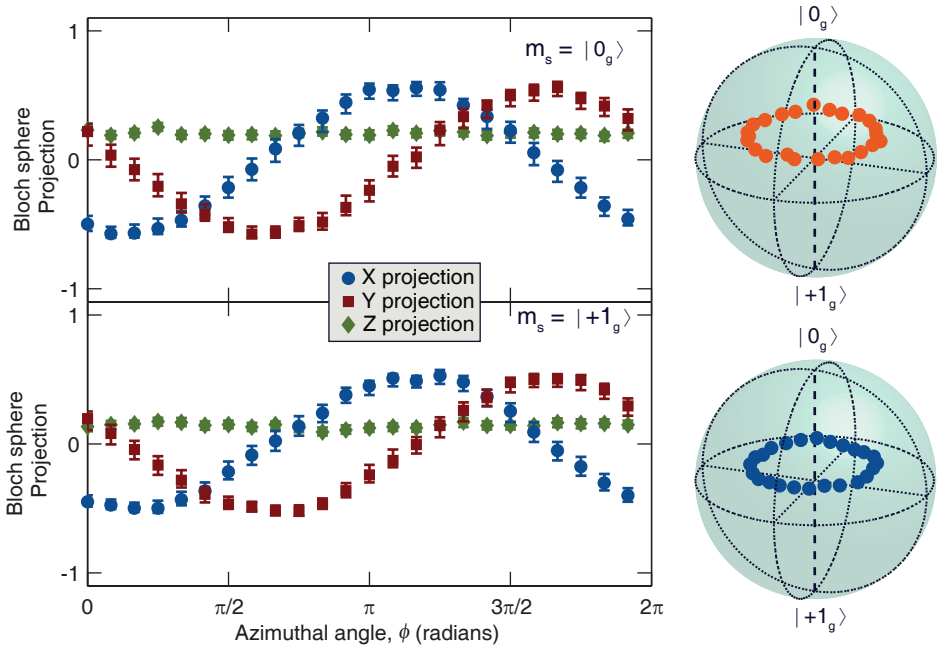

Figure B.3: Projections for azimuthal initialization of spins The azimuthal location of the polarized spin state is rotated along the equatorial plane by varying the relative phase between the two colors. X, Y, and Z projections are plotted on the left, and reconstructed Bloch spheres are plotted on the right. Top: Prior to the CPT interaction, the state was $|0_g\rangle$. Bottom: Prior to the CPT interaction, the state was in $|+1_g\rangle$; this data is presented in Fig. 3.6a in Bloch sphere form. Error bars on projections are the 68.2% highest posterior density credible intervals from the Bayesian analysis.

this is not long enough to fully polarize the spin.

Note that in Fig. B.4, there is an asymmetry between the Z projection of the dark state near the poles depending on whether the state was prepared in $|0_g\rangle$ or $|+1_g\rangle$. This is partly due to the fact that a longer initialization pulse would be required to fully move the state to the opposite pole. In addition, some of this imbalance could also be due to differential spin coupling of the ISC and its resultant decay before readout occurs.

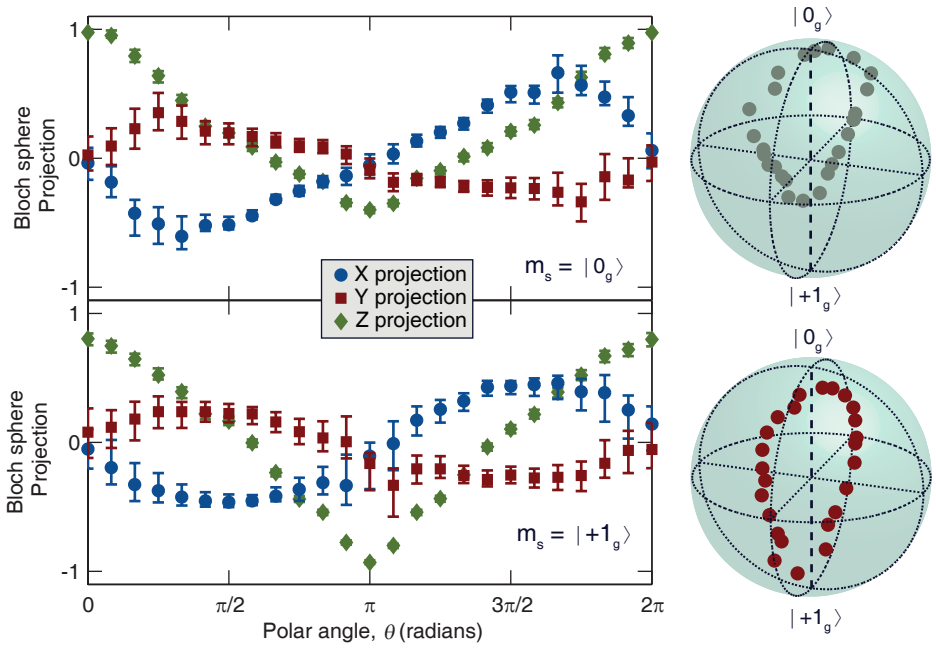

Figure B.4: Projections for polar initialization of spins We vary the polar location of the polarized spin state by varying the relative amplitude between the two colors. X, Y, and Z projections are plotted on the left, while the same points in a Bloch sphere representation are plotted on the right. Top: Prior to the CPT interaction, the state was in $|0_g\rangle$. Bottom: Prior to the CPT interaction, the state was in $|+1_g\rangle$; these data are also presented in Fig. 3.7a in Bloch sphere form. Error bars on projections are the 68.2% highest posterior density credible intervals from the Bayesian analysis.

This effect can also be seen in the Fig. B.5 data, where we combine phase and amplitude control of the light fields in order to initialize points along a great circle rotated $\pi/4$ off the equator.

Finally, we should also note that the collection of Bloch sphere representations in Ch. 3 and in this Appendix are not all viewed from the same vantage point, some were rotated to better show the results. However, within a single figure the angle of view is fixed. One angle of view is used

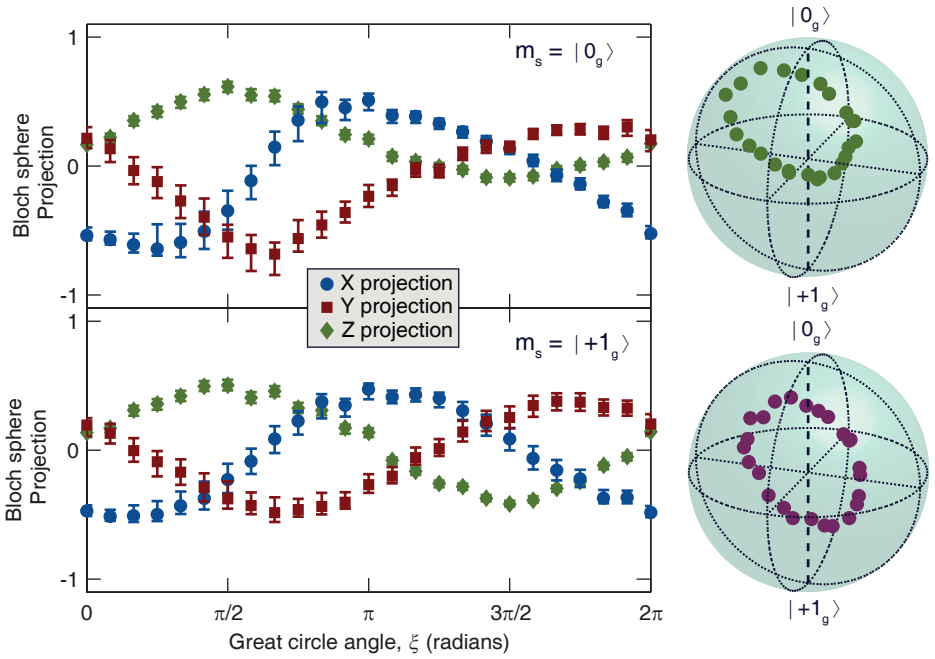

Figure B.5: Projections for initialization of spins along an off-axis great circle Here we vary both the relative amplitude and phase between the two colors to place the spins at points along a great circle, tilted $\pi/4$ off of the equator. Top: Prior to the CPT interaction, the state was in $|0_g\rangle$. Bottom: Prior to the CPT interaction, the state was in $|+1_g\rangle$, this data is presented in Fig. 3.7b. Error bars on projections are the 68.2% highest posterior density credible intervals from the Bayesian analysis.

for the Bloch spheres in Fig. 3.4 and Fig. B.6 (understanding the time dynamics of CPT initialization). A second angle of view is used for the Bloch spheres in Figs. 3.6, 3.7, B.3, B.4, and B.5 (the ability to arbitrarily initialize the spin state). A third angle of view is used for the Bloch spheres in Figs. 3.11, B.7, B.8, and B.9 (the ability to arbitrarily rotate the spin state).

B.3 Model of arbitrary initialization and rotation

The Hamiltonian describing our system (Equation 3.1) is presented below in matrix form,

$$H = h \begin{pmatrix} \Delta_L & 0 & \Omega\cos(\theta/2) & \Omega\cos(\theta/2) & 0 \\ 0 & \Delta_L & \Omega\sin(\theta/2)e^{i\phi} & -\Omega\sin(\theta/2)e^{i\phi} & 0 \\ \Omega\cos(\theta/2) & \Omega\sin(\theta/2)e^{-i\phi} & 0 & 0 & 0 \\ \Omega\cos(\theta/2) & -\Omega\sin(\theta/2)e^{-i\phi} & 0 & -\delta_{e1}/h & 0 \\ 0 & 0 & 0 & 0 & \epsilon_S/h \end{pmatrix} \tag{B.5}$$

where the order of the states in the matrix is: $\{|+1_g\rangle, |0_g\rangle, |R_{e1}\rangle, |L_{e1}\rangle, |S\rangle\}$, Δ_L is the detuning of the laser frequency ($\omega_L/2\pi$) from resonance to the $|R_{e1}\rangle$ Λ system, δ_{e1} is the separation of the excited state levels, Ω is the optical Rabi frequency, ϕ is the relative phase between the two coherent light fields, and $\tan(\theta/2)$ is the relative amplitude between the driving fields. As such, ϕ and θ will describe the azimuthal and polar angle, respectively, of the resultant dark state.

The time evolution of the system is described by the Lindblad master equation [86, 87],

$$\dot{\rho} = i\left[\rho, H\right] + \sum_{\alpha,\alpha'} \Gamma_{\alpha\alpha'} \left(\sigma_{\alpha'\alpha}\rho\sigma_{\alpha\alpha'} - \frac{1}{2}\sigma_{\alpha\alpha}\rho - \frac{1}{2}\rho\sigma_{\alpha\alpha} \right) \equiv W\rho, \tag{B.6}$$

with Lindblad operators $\sigma_{\alpha\alpha} = |\alpha\rangle\langle\alpha| = \sigma^{\dagger}_{\alpha'\alpha}\sigma_{\alpha'\alpha}$ and $\sigma_{\alpha'\alpha} = \sigma^{\dagger}_{\alpha\alpha'} = |\alpha'\rangle\langle\alpha|$.

For $n = 5$ levels, the density matrix ρ is a Hermitian 5x5 matrix and can thus be described by $n^2 = 25$ real parameters ($n^2 - 1 = 24$ including the normalization condition $\mathrm{Tr}\,(\rho) = 1$). The superoperator W can thus be viewed as a 25x25 matrix with rank 24. We denote the decay rate from the excited states ($E = L, R$) to the ground states ($G = 0, 1$) with $\Gamma = \Gamma_{E_{e1},G_g}$, the rate for inter-system crossing from the excited states to the singlet $\Gamma_i = \Gamma_{E_{e1},S}$, and the inverse intersystem crossing rate from $|S\rangle$ to one of the ground state levels as $\Gamma_i' = \Gamma_{S,G_g}$. The spin relaxation rate in the ground state is $\Gamma_1 = 1/T_1 = \Gamma_{+1_g,0_g}$ and at sufficiently low temperature $\Gamma_{0_g,+1_g} \approx 0$. The pure dephasing between the two ground state levels is denoted $\gamma = 1/T_2 = \Gamma_{0_g,0_g}$. All other rates are set to zero.

The state of the system after optical excitation during time t is obtained as

$$\rho(t) = e^{Wt}\rho(0), \tag{B.7}$$

where we choose one of the ground states as the initial state, $\rho(0) = |0_g\rangle\langle 0_g|$ or $\rho(0) = |+1_g\rangle\langle +1_g|$. We typically determine $\rho(t)$ by performing the exponentiation Eq. (B.7) numerically. The resulting Bloch vector in the ground state subspace can be obtained from

$$\mathbf{b}(t) = \mathrm{Tr}\,(\boldsymbol{\sigma}\rho(t))\,, \tag{B.8}$$

where the components of $\boldsymbol{\sigma}$ are the Pauli matrices in the ground-state

subspace,

$$\sigma_{\mathrm{x}} = |+1_g\rangle\langle 0_g| + |0_g\rangle\langle +1_g|, \tag{B.9}$$

$$\sigma_{\mathrm{y}} = i(|+1_g\rangle\langle 0_g| - |0_g\rangle\langle +1_g|), \tag{B.10}$$

$$\sigma_{\mathrm{z}} = |0_g\rangle\langle 0_g| - |+1_g\rangle\langle +1_g|. \tag{B.11}$$

In the idealized case $\Gamma_1 = \gamma = \Gamma_i = 0$, and with only one of the excited levels included, the stationary state $\bar{\rho}$ in the long-time limit $t \gg 1/\Gamma$ obtained from $\dot{\rho} = 0$ as the eigenvector of W with eigenvalue 0 is the dark state:

$$|D\rangle = \cos(\theta/2)|0_g\rangle \mp \exp(-i\phi)\sin(\theta/2)|+1_g\rangle \tag{B.12}$$

where the upper (lower) sign holds for the single excited state level being $E = R$ ($E = L$). The fidelity of the state after a finite pumping time t with realistic parameters is then

$$F(t) = \langle D|\rho(t)|D\rangle. \tag{B.13}$$

The experimentally obtained fidelity is shown in Fig. 3.5.

We use this model to simulate the time evolution of the Bloch vector $\mathbf{b}(t)$ during 500 ns of CPT initialization plotted in Figs. 3.3 and 3.4 and the 200 ns of SRT rotation in Fig. 3.11 (Figs. B.7 - B.9). We fix the excited state splitting $\delta_{e1}/h = 180$ MHz, and Γ_i' using the known lower singlet lifetime of 371 ns [39]. We also fix the rate for both the $|R_{e1}\rangle$ and $|L_{e1}\rangle$ states into the singlet, Γ_i, as one half of the known ISC rate of $m_s = \pm 1$

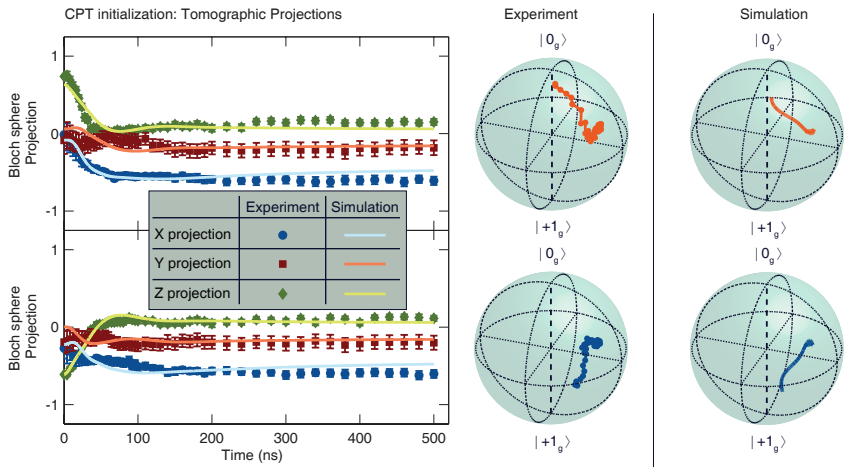

Figure B.6: Time dynamics of arbitrary initialization: theory vs. experiment As a function of CPT initialization pulse duration, tomographic reconstructions of the spin state are plotted alongside a simulation of the resultant state using the model. Top: Prior to the CPT interaction, the state was $|0_g\rangle$. Bottom: Prior to the CPT interaction, the state was in $|+1_g\rangle$. Error bars on projections are the 68.2% highest posterior density credible intervals from the Bayesian analysis. Parameters to simulate spin-state initialization are found in Table B.1.

spin states to the singlet of $\approx 74\,\mathrm{MHz}$, since $|R_{e1}\rangle$ and $|L_{e1}\rangle$ are composed of equal mixtures of $m_s = 0$ and $m_s = +1$ states. The detuning of the optical fields relative to $|R_{e1}\rangle$, Δ_L, is fixed to the experimentally measured detuning for each operation (CPT initialization, SRT σ_x rotation, SRT σ_y rotation, SRT σ_z rotation). Using a weighted least squares approach, we fit the overall driving amplitude, Ω, relative amplitude, $\tan(\theta/2)$, relative phase of the driving fields, ϕ, and the decay rates Γ, Γ_1, and γ, described above. All simulations show qualitative agreement with the experiment, however certain traces appear to have out-of-phase behavior of individual

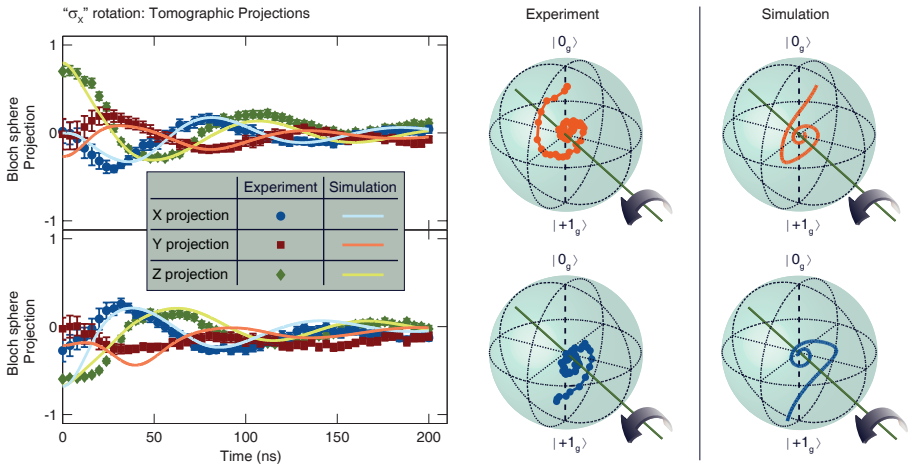

Figure B.7: Time dynamics of arbitrary coherent σ_X rotation: theory vs. experiment As a function of the duration of a SRT σ_X rotation pulse duration, projections of the resultant spin state are plotted alongside a simulation of the resultant state using the model. Top: Prior to the SRT interaction, the state was $|0_g\rangle$. Bottom: Prior to the SRT interaction, the state was in $|+1_g\rangle$. Error bars on projections are the 68.2% highest posterior density credible intervals from the Bayesian analysis. Parameters to simulate the σ_X rotation are found in Table B.1.

projections, marginal agreement with the initial state, or other disagreements. It appears that the model captures the essential physics but cannot fully account for certain ill-defined nuances such as the transients during the turn-on/off of the optical fields and effects related to the hyperfine spectrum and T_2^*. Therefore, the fitted values for the decay parameters are skewed by effects not considered in the model. A full set of fixed and fit parameters is found in Table B.1.

As mentioned in the main text, it may be possible to rotate about any arbitrary axis, but there are a few considerations to be made. SRT are

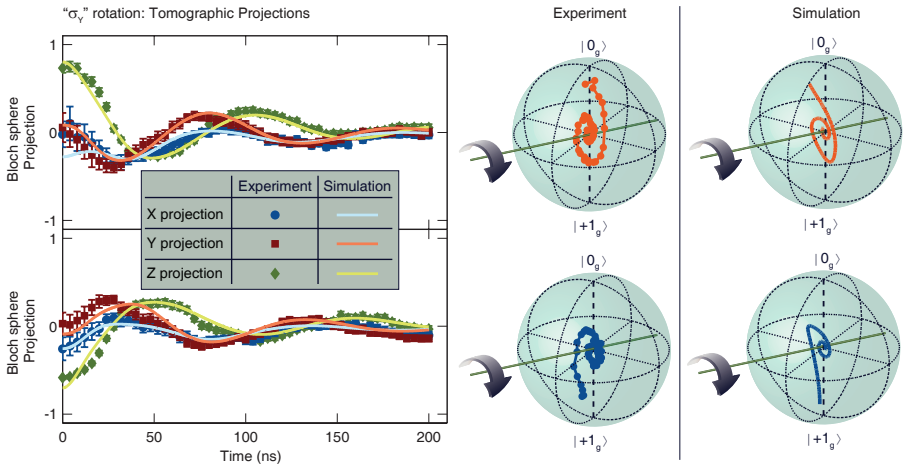

Figure B.8: Time dynamics of arbitrary coherent σ_Y rotation: theory vs. experiment As a function of the duration of a SRT σ_Y rotation pulse duration, projections of the resultant spin state are plotted alongside a simulation of the resultant state using the model. Top: Prior to the SRT interaction, the state was $|0_g\rangle$. Bottom: Prior to the SRT interaction, the state was in $|+1_g\rangle$. Error bars on projections are the 68.2% highest posterior density credible intervals from the Bayesian analysis. Parameters to simulate the σ_Y rotation are found in Table B.1.

a dispersive interaction whose strength is proportional to $1/\Delta_L$, whereas CPT is an absorptive process whose interaction strength is proportional to $1/\Delta_L^2$. To take advantage of SRT, sufficient detuning is necessary to diminish absorptive effects that are non-unitary and cause the spin to polarize along the dark state rather than rotate. In the case of rotations about an equatorial axis, we take advantage of the two competing Λ systems by tuning ω_L exactly between $|R_{e1}\rangle$ and $|L_{e1}\rangle$ resonances. These Λ systems have opposite equatorial bright states and we detune from both in opposite directions, essentially causing SRT effects to add constructively

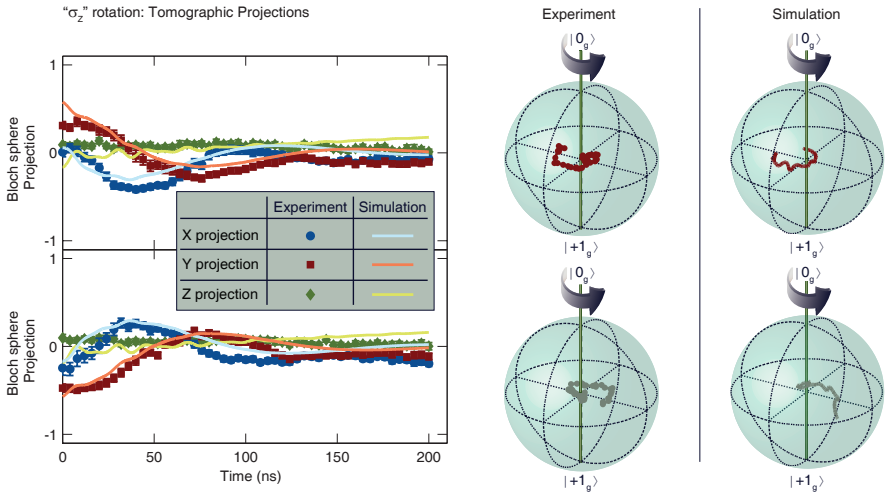

Figure B.9: Time dynamics of arbitrary coherent σ_Z rotation: theory vs. experiment As a function of the duration of a SRT σ_Z rotation pulse duration, projections of the resultant spin state are plotted alongside a simulation of the resultant state using the model. Top: Prior to the SRT interaction, the state was $|X_g\rangle$. Bottom: Prior to the SRT interaction, the state was in $|-X_g\rangle$. Error bars on projections are the 68.2% highest posterior density credible intervals from the Bayesian analysis. Parameters to simulate the σ_Z rotation are found in Table B.1.

and the CPT effects to add destructively. In order to rotate about an axis off of the equator, care must be taken to couple more strongly to one of the Λ systems than the other because their corresponding bright states are no longer orthogonal, as the bright states for each Λ system will have orthogonal azimuthal phases but the same polar component. As discussed above, a more widely spaced anticrossing to decrease the competition between the two upper states would aid in ensuring unitary non-equatorial axial rotations. The special case of rotation about the polar axis, which we demonstrate in Fig. 3.11b, was also shown in Buckley *et al.*[11, 42] but not

Table B.1: Driven Λ system simulation parameters Simulation parameters for CPT initialization, σ_{X}, σ_{Y}, and σ_{Z}. In the case of CPT initialization, σ_{X}, and σ_{Y}, the initial state parameters state A refers to $|0_{\mathsf{g}}\rangle$ and state B refers to $|+1_{\mathsf{g}}\rangle$. For σ_{Z}, state A corresponds to $|\mathsf{X}_{\mathsf{g}}\rangle$ and state B corresponds to $|-\mathsf{X}_{\mathsf{g}}\rangle$.

	Param.	CPT init.	σ_{X}	σ_{Y}	σ_{Z}
Fixed Level	δ_{e1}/h	180 MHz	180 MHz	180 MHz	180 MHz
Parameters	Δ_L	−0.684 MHz	−90 MHz	−90 MHz	−450 MHz
Optical	Ω	46.507 MHz	62.021 MHz	62.756 MHz	84.104 MHz
Driving Field	θ	1.708 rad	4.774 rad	1.763 rad	π rad
Parameters	ϕ	0.395 rad	4.152 rad	2.683 rad	0.424 rad
Decay	Γ	35.114 MHz	17.115 MHz	19.719 MHz	0
Parameters	Γ_i	37 MHz	37 MHz	37 MHz	37 MHz
	Γ'_i	2.701 MHz	2.701 MHz	2.701 MHz	2.701 MHz
	Γ_1	0.373 MHz	0	0	0
	γ	0	0	0	28.459 MHz
Initial State	r_A	0.640	0.839	0.852	0.602
Parameters	θ_A	0.164 rad	0.327 rad	0.347 rad	1.844 rad
	ϕ_A	2.526 rad	4.705 rad	2.850 rad	1.471 rad
	r_B	0.649	0.977	0.752	0.621
	θ_B	2.788 rad	2.325 rad	2.774 rad	1.870 rad
	ϕ_B	3.122 rad	3.450 rad	3.472 rad	4.425 rad

in the context of a Λ system. In our case, we sufficiently detune ∼450 MHz from the $|R_{e1}\rangle$ such that any effects from CPT are greatly diminished.

B.4 Sources of decoherence

The closeness in energy of the two anticrossed eigenstates, $|R_{e1}\rangle$ and $|L_{e1}\rangle$, causes a loss in fidelity. This is because even when resonantly tuned to a single eigenstate, there is still off-resonant coupling to the other Λ system. As the phases of these two dark states are orthogonal, the overall length of the vector pointing to the final state within the Bloch sphere is reduced. The model shows good qualitative agreement to our presented data, revealing a similarly mixed state as a result of the competing Λ systems. Therefore, this competition is one of the most significant sources of decoherence in our measurement. Finding a more widely spaced anticrossing would help alleviate this issue by decreasing the coupling to the other state; within the model, a purer final state (higher fidelity) results with increasing separation of the two excited states. Experimentally, one method to achieving more widely spaced anticrossing would be to slightly misalign the field because off-axis fields will increase the separation in any anticrossing. However, it should be noted that a misalignment of the field will also change the eigenstates, possibly producing more transitions from spin-mixing into the $|-1_g\rangle$ spin sublevel, which also causes a loss in fidelity.

Further sources of decoherence include the transverse inhomogeneous spin coherence time $T_2^* \sim 1\,\mu$s as well as the fact that our spin sublevels are further split into three nuclear hyperfine states due to the ^{14}N in our

NV center, with each transition split by $\sim$2 MHz. Since our measurements are averages over $\sim 10^6$ replications of the same experiment, any individual replication has an equal probability of being in any of the three hyperfine states, causing our selected ω_{mw} to be $\sim \pm 2$ MHz detuned from the actual ground state splitting two thirds of the time. We note that no nuclear polarization was observed at this excited state anticrossing at cryogenic temperatures. This hyperfine spectrum and finite T_2^* effectively set limits on how long our Λ interaction remains phase coherent with the spin, reducing transverse coherence of the interaction. The resultant steady state is a balance between the strength of the interaction and these decoherence mechanisms (along with the other mechanisms mentioned in this section). As such, an echo sequence would not eliminate these effects while the interaction is taking place, but only during the rest of the measurement sequence. In addition, as the NV center is a solid-state defect, spectral diffusion causes a broadening of the natural linewidth of the resonances[35], which will also contribute to a lower fidelity.

Finally, since we are examining a Λ system contained within a more complex level structure, the spin will end up outside of our qubit subspace a fraction of the time. First of all, the spin can end up passing through the long-lived ISC, which is accounted for in the model as a singlet level, and does manifest as a decoherence mechanism. Secondly, since our qubit states, $|0_g\rangle$ and $|+1_g\rangle$, are a subspace of a spin-triplet ground state, the spin

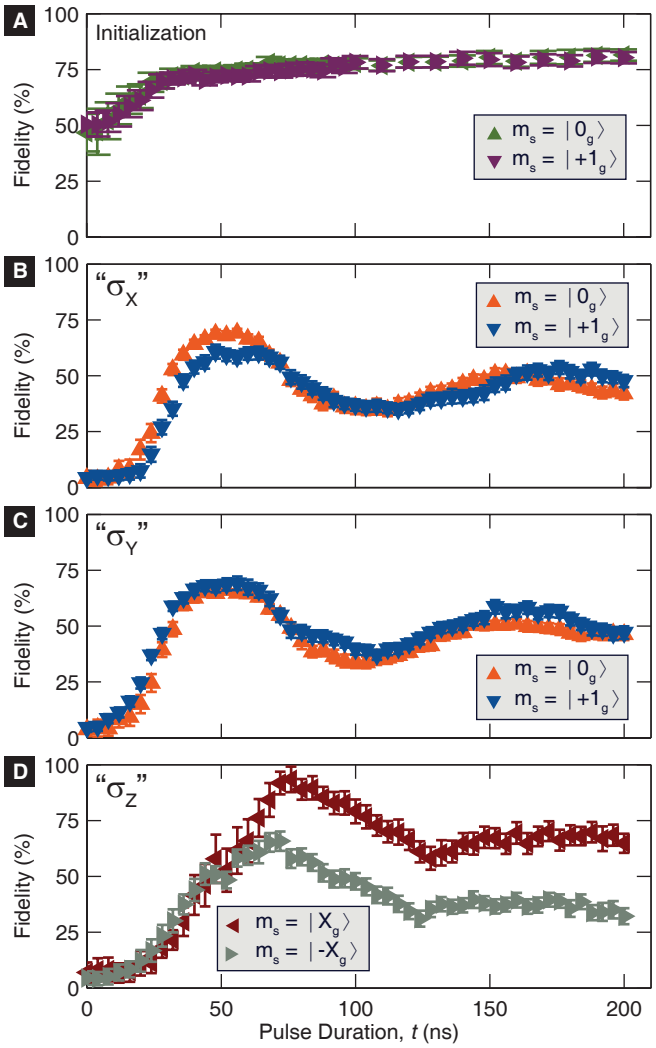

Figure B.10: Fidelities of initialization and rotation A, Fidelity of initialization as a function of pulse duration for an initial state $|0_g\rangle$ and $|+1_g\rangle$. **B**, Process fidelity of σ_X rotation compared to a perfect π rotation, as a function of pulse duration for an initial state $|0_g\rangle$ and $|+1_g\rangle$. **C**, Process fidelity of σ_Y rotation as compared to a perfect π rotation, as a function of pulse duration for an initial state $|0_g\rangle$ and $|+1_g\rangle$. **D**, Process fidelity of σ_Z rotation as compared to a perfect π rotation, as a function of pulse duration for an initial state $|X_g\rangle$ and $|-X_g\rangle$. For all process fidelities, we compare the resultant state, as a function of pulse duration, to a state exactly π out-of-phase with the initial state about the rotation axis. We renormalize the initial mixed state to a pure state in order to compute the fidelity loss from the CPT or SRT process alone.

can transition to $|-1_g\rangle$ some of the time. This is because, experimentally, the excited state levels $|R_{e1}\rangle$ and $|L_{e1}\rangle$ each contain anywhere from 1% to 3% of the excited state spin sublevel $|-1_{e1}\rangle$. A spin in the$|-1_g\rangle$ sublevel is not resonant with our red lasers and will therefore appear dark. This suggests that there might be higher fidelities resulting from implementation of this type of control within a system that lacks decay mechanisms such an intersystem crossing.

Through our tomographic reconstructions, we are able to determine that the fidelity of our spin-state initialization saturates at roughly 80% after 100 ns (Fig. B.10A). The fidelities of a σ_{X} or σ_{Y} π rotation are as high as 69% if we assume a pure initial state as the initial state instead the mixed state used in the experiment (Fig. B.10B, C). A σ_{Z} π rotation could have process fidelities as high as 90% (Fig. B.10D), but as the initial states used for that experiment were of lower fidelity than any other experiment, this estimation may be rather optimistic.

B.5 Arbitrary spin-state readout

The following pulse sequence was used to perform the DBP readout protocol.

Our DBP optical spin readout protocol begins with preparation with non-resonant 532 nm excitation to prepare the state in $|0_g\rangle$. This is followed by an on-chip microwave pulse to prepare the spin at various points about

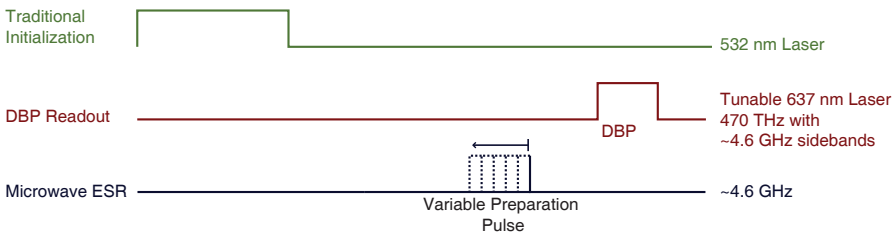

Figure B.11: Pulse sequence for arbitrary spin-state readout The above pulse sequence was used for the data presented in Fig. 3.9. The DBP readout experiments consisted of 3.75×10^6 iterations of this pulse sequence.

the Bloch sphere. In the case of Fig. 3.9a, the pulse corresponds to a $\pi/2$ pulse, and its phase is varied to place the spin at various points about the Bloch sphere equator. In the case of Fig. 3.9b, its pulse duration is varied to induce Rabi oscillations between the ground state spin sublevels, $|0_g\rangle$ and $|+1_g\rangle$, initializing the spin at various points along a meridian. A DBP pulse of 400 ns is used to read out the spin state and is delayed 450 ns from the microwave initialization pulse, much like the delay between the CPT initialization and the ESR $\pi/2$ projection pulses for quantum state tomography of CPT and SRT. Spin readout protocols such as QST could be performed directly with DBP mitigating the need for ESR; however, the differing PL contrasts between polar and azimuthal spin readout as a result of qubit dephasing must be appropriately calibrated out (Fig. 3.9).

To determine the quality of DBP spin readout vs. traditional "green" spin readout via the ISC, we analyze the signal-to-shot-noise ratio of both readout methods. Shot noise of counted photons is the primary noise source

in our data, which is a common feature for these types of experiments with proper mitigation of any systematic errors such as experimental drift. Each data point in Fig. 3.9 consists of summed photon counts of $n = 3.75 \times 10^6$ individual spin readouts using a 400 ns DBP pulse. When fit to a sinusoid, the polar Bloch sphere readout in Fig. 3.9b results in $I_{BZ} = 4850$ counts if the spin is in the bright state and $I_{DZ} = 1750$ counts if the spin is in the dark state (averaged fit values of $|0_g\rangle$ and $|+1_g\rangle$ data). The equatorial Bloch sphere readout in Fig. 3.9b with reduced contrast primarily due to dephasing results in $I_{BX} = 5380$ counts if the spin is in the bright state and $I_{DX} = 3160$ counts if the spin is in the dark state (averaged fit values of $|X_g\rangle$ and $|-X_g\rangle$ data). To compare to traditional ISC "green" readout, we will assume reasonable numbers for green readout with our specific confocal setup: a 400 ns readout window with 20,000 Cts/s for the $m_s = 0$ spin state, and a 30% reduction of counts for $m_s = \pm 1$ spin states during this window. For an equivalent averaging time ($n = 3.75 \times 10^6$), this corresponds to green spin readout counts of: $I_{BG} = 30{,}000$ and $I_{DG} = 21,000$. The number of spin readouts (N_i) required for the noise standard deviation ($\sqrt{n}$) to be roughly equal to the full-scale readout contrast is:

$$N_i = \frac{n/2 \times (I_{Bi} + I_{Di})}{(I_{Bi} - I_{Di})^2} \tag{B.14}$$

the number of individual spin readouts to get a signal-to-noise ratio of unity for these three readout techniques (Polar DBP (N_{Z}), Azimuthal DBP (N_{X}), and green ISC (N_{G}) are respectively:

$$N_{\mathrm{Z}} = 1290,\ N_{\mathrm{X}} = 3250,\ N_{\mathrm{G}} = 1180$$

Therefore, using these rough numbers, DBP on a polar axis ("spin up" vs. "spin down") has a signal-to-noise ratio comparable to green spin up/down readout, while DBP on a precessing equatorial axis ("spin left" vs. "spin right") takes roughly three times as much averaging to get the same signal-to-noise ratio as the other two techniques.

B.6 All-optical Ramsey measurement

We use the pulse sequence in Fig. B.12 to take the data for the top portion of Fig. 3.10 and in Fig. B.13.

The Ramsey data plotted in Fig. 3.10 of the main text shows the difference in measured PL for two orthogonal initial spin projections, $\Delta\mathrm{PL} = \mathrm{PL}(|-X_{\mathrm{g}}\rangle) - \mathrm{PL}(|X_{\mathrm{g}}\rangle)$. The difference cancels the contribution to the PL from the ISC decay in the optical Ramsey measurements (Fig. B.13), and effectively measures the projection $\langle S_X \rangle$ of the spin at the end of the free precession period. In both cases the data is fit to a function of the form

$$\Delta\mathrm{PL} = A \exp\left(-\frac{\tau^2}{2T_2^{*2}}\right)\Big\{C_1 \cos\big[2\pi(-\Delta_{GS} - \omega_{\mathrm{HF}}/2\pi)(\tau-\tau_0)\big] + \cos\big[-2\pi\Delta_{GS}(\tau-\tau_0)\big] + C_2\cos\big[2\pi(-\Delta_{GS}+\omega_{\mathrm{HF}}/2\pi)(\tau-\tau_0)\big]\Big\}, \tag{B.15}$$

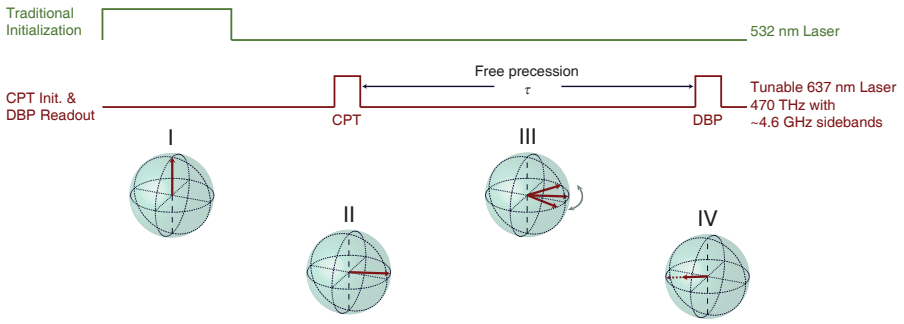

Figure B.12: Pulse sequence for arbitrary spin-state readout I. We begin with a non-resonant 532 nm excitation to prepare the state in $|0_g\rangle$. II. The state is then initialized onto the equator with a CPT pulse of length 50 ns, in one of four azimuthal positions $\pi/2$ out-of-phase from one another other. III. The spin state dephases during free precession, τ, which is varied. IV. The state is then read out with a DBP pulse of length 50 ns of a fixed phase. The data of two opposite CPT pulse phases were subtracted and plotted in the top of Fig. 3.10. The EOM microwave detuning, $\Delta_{GS} \sim -7.5$ MHz, is from the mean qubit precession.

where

$$\Delta_{GS} = \delta_{GS}/h - \omega_{mw}/2\pi, \tag{B.16}$$

and includes the threefold hyperfine coupling to the ^{14}N nuclear spin with frequency, ω_{HF}, inhomogeneous dephasing with characteristic time T_2^*, and independent amplitudes for the three hyperfine components. The temporal offset τ_0 accounts for the effects of finite-duration initialization and readout pulses. Best-fit parameter values for the curves plotted in Fig. 3.10 are provided in Table B.2.

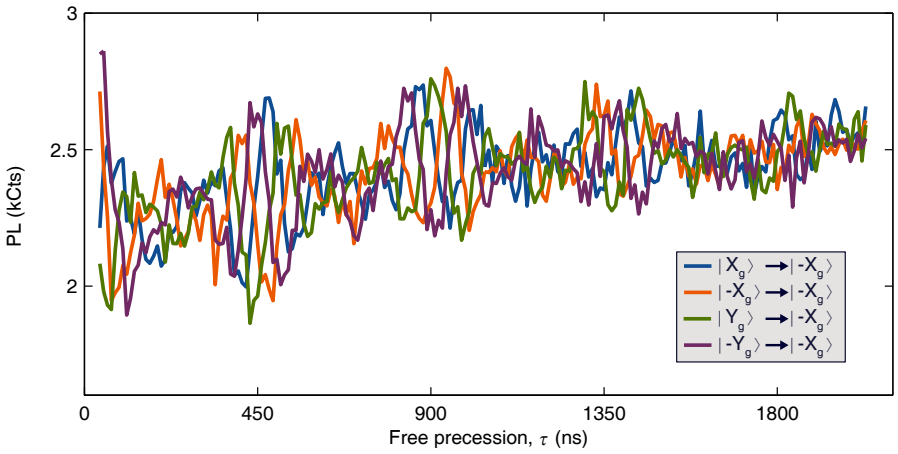

Figure B.13: Non-subtracted all-optical Ramsey measurement Four different phases of a time-domain Ramsey experiment were measured and are plotted above. The overall background is due to the CPT pulse populating the dark ISC, which subsequently decays over time, making the DBP PL brighter as it gets further away from the CPT pulse.

Table B.2: Ramsey fit parameters Best-fit parameter values from fits of the model of Eq. B.15 to the data in Fig. 3.10 of the main text. Uncertainties are standard error.

	T_2^* (μs)	Δ_{GS} (MHz)	$\omega_{\mathrm{HF}}/2\pi$ (MHz)	τ_0 (ns)	A (Cts)	C_1	C_2
Optical	1.13 ± 0.05	7.52 ± 0.01	2.19 ± 0.01	13 ± 1	253 ± 13	1.36 ± 0.07	0.64 ± 0.05
ESR	1.01 ± 0.03	7.34 ± 0.01	2.20 ± 0.01	-12 ± 2	1230 ± 40	1.16 ± 0.04	0.68 ± 0.04

B.7 All-optical Hahn echo measurement

We use the pulse sequence in Fig. B.14 to take the data in Fig. 3.12.

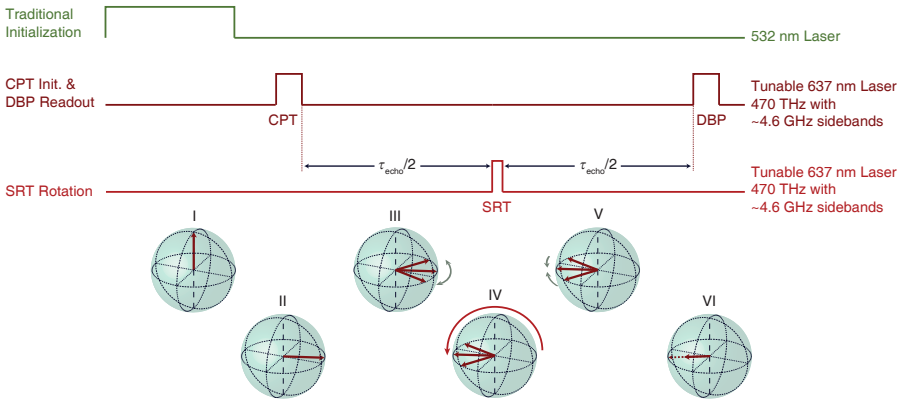

Figure B.14: Pulse sequence for all-optical Hahn echo measurement I. A 532 nm excitation is used to prepare the state into $|0_g\rangle$. II. The spin is initialized on the Bloch equator with a CPT pulse (Fig. 3.6a). III. Dephasing of the spin state occurs during free precession for a delay $\tau_{\text{echo}}/2$. IV. The spin is then rotated by a SRT pulse (Fig. 3.11a). V. Rephasing of the spin state occurs during a period of $\tau_{\text{echo}}/2$. VI. Finally the spin state is readout along the equator with a DBP pulse (Fig. 3.9), corresponding to a bright state either in-phase or π out-of-phase with the CPT pulse. The Hahn precession time, τ_{echo}, is varied.

Table B.3: Hahn echo fit parameters Best-fit parameter values from fits of the model to the data in Fig. 3.12 of the main text. Uncertainties are standard error.

	T_2 (μs)	A (Cts)
Optical	893 ± 51	538 ± 29
ESR	909 ± 30	2991 ± 99

In Fig. 3.12, the all-optical Hahn echo measurement is plotted on top of the data set for the ESR-based Hahn echo. We use least squares to fit the function $\Delta\text{PL} = A \exp\left(-\left(\tau_{\text{echo}}/T_2\right)^3\right)$ to our data and infer T_2 ~900 µs

for both measurements. The fitting parameters are provided in Table B.3.

Appendix C

Supporting data for Chapter 4

C.1 Theoretical model of stimulated Raman adiabatic passage (STIRAP)

In this section, we present the theoretical model we use to describe the NV center in a Λ configuration driven by two optical laser fields (Fig. 4.1a). We numerically solve a quantum master equation and obtain good agreement with the experimental measurements of the dark-state magnitude (Fig. 4.4a) and the Berry-phase visibility (Fig. 4.11). We calculate the population of the bright states as well, which gives insight regarding the decrease in dark-state magnitude. Furthermore, the theoretical model allows us to extract the Berry phase itself.

C.1.1 Hamiltonian

In a properly chosen rotating frame, the Hamiltonian describing the NV center Λ system and the optical driving fields within the NV center level

structure is given by

$$H(t) = \frac{h}{2}\begin{pmatrix} 0 & 0 & 0 & 0 \\ 0 & 0 & 0 & \Omega_{-1}(t) \\ 0 & 0 & 2\delta & \Omega_{+1}(t)e^{i\phi(t)} \\ 0 & \Omega_{-1}(t) & \Omega_{+1}e^{-i\phi(t)} & 2\Delta \end{pmatrix}, \tag{C.1}$$

where the matrix representation is given in the basis $\{|0_g\rangle, |-1_g\rangle, |+1_g\rangle, |A_2\rangle\}$. In deriving $H(t)$, the rotating wave approximation has been applied. In Eq. (C.1), Δ denotes the detuning from one-photon resonance, δ is the detuning from two-photon resonance, $\Omega_i(t)$ is the time-varied Rabi frequency of the laser that drives the optical transition between $|i_g\rangle$ and $|A_2\rangle$ ($i = \pm 1$), and $\phi(t)$ is the relative phase between the two laser fields. In the further calculations, we use the exact pulse shapes $\Omega_i(t)$ (see, e.g., Fig. 4.2b), described in §C.3.1.

C.1.2 Quantum master equation

To model decoherence and relaxation, we use a quantum master equation that is, in Lindblad form, given by [142]

$$\dot{\rho}(t) = -i[H(t), \rho(t)] + \sum_k \left(L_k \rho(t) L_k^\dagger - \frac{1}{2} L_k^\dagger L_k \rho(t) - \frac{1}{2} \rho(t) L_k^\dagger L_k \right). \tag{C.2}$$

Here, $\rho(t)$ is a 4×4 density matrix describing the system and the Lindblad operators L_k specify various dissipative processes present in the actual experiment. In the following, we list all Lindblad operators that are used

for the numerical evaluation. We note that using the Lindblad formalism is equivalent to the methods developed in Ref. [143].

To describe relaxation processes from the optically excited state $|A_2\rangle$ to the ground-state manifold, we use three Lindblad operators (one for each ground-state spin level)

$$\begin{aligned} L_0 &= \sqrt{\Gamma_0}\,|0_{\rm g}\rangle\,\langle A_2|\,, \\ L_{-1} &= \sqrt{\Gamma_{-1}}\,|{-1_{\rm g}}\rangle\,\langle A_2|\,, \\ L_{+1} &= \sqrt{\Gamma_{+1}}\,|{+1_{\rm g}}\rangle\,\langle A_2|\,. \end{aligned} \tag{C.3}$$

The decay rates have been experimentally estimated to be $(\Gamma_0)^{-1} \approx 104$ ns, $(\Gamma_{-1})^{-1} \approx 31$ ns, and $(\Gamma_{+1})^{-1} \approx 24$ ns (see §C.2.2), assuming a lifetime of the excited state of $(\Gamma_0 + \Gamma_{-1} + \Gamma_{+1})^{-1} \approx 12$ ns (Ref. [144]).

Further decoherence comes from spin dephasing in the ground-state manifold. We use the $|0_{\rm g}\rangle$ spin state as reference and describe dephasing of the other two spin states with the Lindblad operators

$$L_{\rm spin,-1} = \sqrt{\Gamma_{\phi,\pm1}}\,|{-1_{\rm g}}\rangle\,\langle{-1_{\rm g}}|\,, \tag{C.4}$$

$$L_{\rm spin,+1} = \sqrt{\Gamma_{\phi,\pm1}}\,|{+1_{\rm g}}\rangle\,\langle{+1_{\rm g}}|\,. \tag{C.5}$$

The decoherence time, $T_{\phi,\pm1} = (\Gamma_{\phi,\pm1})^{-1} = 2.25\,\mu$s, is a free parameter in the model and is intended to simulate the decrease in the Berry phase visibility for longer traversal times, τ. Such decoherence is due to a number of factors, including the effects of spin dephasing from nuclear spin

bath fluctuations and unaccounted driving by additional detuned laser harmonics generated by the electro-optic modulator (EOM). These non-ideal processes permit non-adiabatic transitions to occur even while, in principle, the evolution due to the main driving fields becomes more adiabatic for increased τ. An expanded model taking into account the effect of the far-detuned laser harmonics will be found in the published version of this work.

Additionally, we include orbital dephasing between the NV center ground and excited state. We assume a dephasing time of $T_{\phi,\mathrm{orb}} = 7$ ns, which has been measured in Ref. [34]. Although the measurement in Ref. [34] was for a different spin orbit eigenstate, we use the same value for the orbital dephasing time between the excited state $|A_2\rangle$ of our experiments and each ground state spin level, respectively, in order to minimize the number of free parameters. The Lindblad operator for this dissipative process is given by

$$L_{\mathrm{orb}} = \sqrt{2\Gamma_{\phi,\mathrm{orb}}} = |A_2\rangle \langle A_2| , \tag{C.6}$$

with $(\Gamma_{\phi,\mathrm{orb}})^{-1} = T_{\phi,\mathrm{orb}} = 7$ ns.

C.1.3 Dark state magnitude

To obtain the dark state occupation probability (see Fig. 4.4a), we numerically solve the quantum master equation [Eq. (C.2)] to obtain the density matrix of the system at each instant of time t, with an initial state that

accounts for imperfect initialization

$$\rho(0) = 0.2\,|0_{\rm g}\rangle\langle 0_{\rm g}| + 0.8\,|-1_{\rm g}\rangle\langle -1_{\rm g}| + 0\,|+1_{\rm g}\rangle\langle +1_{\rm g}|\,. \tag{C.7}$$

We define Pauli operators

$$\begin{aligned}
\sigma_x &= |-1_{\rm g}\rangle\langle +1_{\rm g}| + |+1_{\rm g}\rangle\langle -1_{\rm g}|\,,\\
\sigma_y &= -i\,|-1_{\rm g}\rangle\langle +1_{\rm g}| + i\,|+1_{\rm g}\rangle\langle -1_{\rm g}|\,,\\
\sigma_z &= |-1_{\rm g}\rangle\langle -1_{\rm g}| - |+1_{\rm g}\rangle\langle +1_{\rm g}|\,,
\end{aligned} \tag{C.8}$$

that act within the $\{|-1_{\rm g}\rangle, |+1_{\rm g}\rangle\}$ subspace. The components of the Bloch vector on the $|-1_{\rm g}\rangle, |+1_{\rm g}\rangle$ Bloch sphere are then defined as

$$\begin{aligned}
X(t) &= \mathrm{Tr}[\sigma_x\rho(t)],\\
Y(t) &= \mathrm{Tr}[\sigma_y\rho(t)],\\
Z(t) &= \mathrm{Tr}[\sigma_z\rho(t)].
\end{aligned} \tag{C.9}$$

In Fig. 4.4a, we normalized the magnitude of the Bloch vector to its initial length, i.e. the plotted value is

$$\frac{\sqrt{X(t)^2 + Y(t)^2 + Z(t)^2}}{\sqrt{X(0)^2 + Y(0)^2 + Z(0)^2}}. \tag{C.10}$$

During the decrease of the dark state magnitude, the Λ system partially occupies one of the non-dark eigenstates, the bright states, which can be seen in Fig. C.1 The dark state of the Hamiltonian $H(t)$ in Eq. (C.1) is given by

$$|D(t)\rangle = \frac{1}{\sqrt{\Omega_{-1}(t)^2 + \Omega_{+1}(t)^2}}\left(\Omega_{+1}(t)\,|-1_{\rm g}\rangle - \Omega_{-1}(t)e^{i\phi}\,|+1_{\rm g}\rangle\right), \tag{C.11}$$

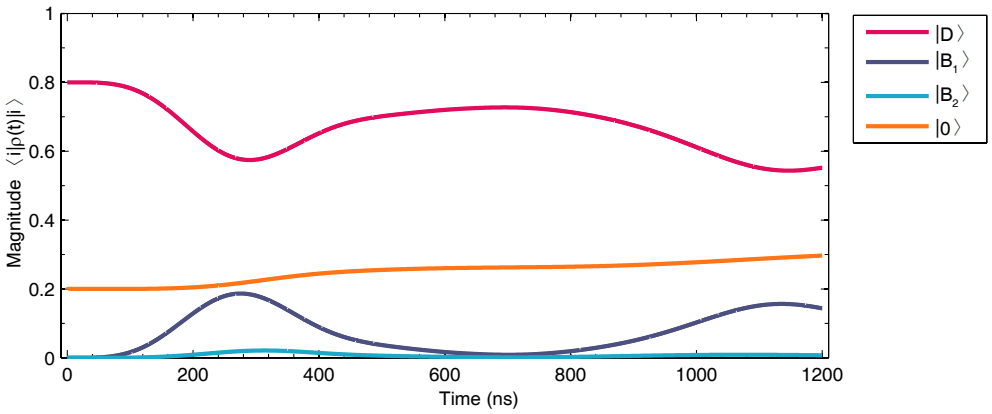

Figure C.1: Instantaneous populations of STIRAP eigenstates. Population $\langle i|\rho(t)|i\rangle$ of eigenstates $|i\rangle$ of Hamiltonian $H(t)$ [Eq. (C.1)]. The dark state $|D(t)\rangle$ and the two bright states $|B_1(t)\rangle$ and $|B_2(t)\rangle$ are given in Eqs. (C.11) - (C.13). $\Delta = 60\,\mathrm{MHz}$ and $\Omega_R = 31\,\mathrm{MHz}$.

and the two bright states are

$$|B_1(t)\rangle \propto \Omega_{-1}(t)\,|-1_\mathrm{g}\rangle + \Omega_{+1}(t)e^{i\phi}\,|+1_\mathrm{g}\rangle + \left(\Delta - \sqrt{\Delta^2 + \Omega_{-1}(t)^2 + \Omega_{+1}(t)^2}\right)|A_2\rangle \quad \text{(C.12)}$$

$$|B_2(t)\rangle \propto \Omega_{-1}(t)\,|-1_\mathrm{g}\rangle + \Omega_{+1}(t)e^{i\phi}\,|+1_\mathrm{g}\rangle + \left(\Delta + \sqrt{\Delta^2 + \Omega_{-1}(t)^2 + \Omega_{+1}(t)^2}\right)|A_2\rangle\,. \quad \text{(C.13)}$$

C.1.4 Berry phase

For the measurement of the Berry phase, the system is initialized to $|0_\mathrm{g}\rangle$ and a $\pi/2$ pulse generates an equal superposition of $|0_\mathrm{g}\rangle$ and $|-1_\mathrm{g}\rangle$. Imperfect initialization is modeled with an initial state

$$\rho(0) = 0.2\,|0_\mathrm{g}\rangle\langle 0_\mathrm{g}| + 0.8\,|-1_\mathrm{g}\rangle\langle -1_\mathrm{g}| + 0\,|+1_\mathrm{g}\rangle\langle +1_\mathrm{g}|\,, \quad \text{(C.14)}$$

to which a perfect $\pi/2$ pulse is applied, and we then solve the master equation numerically. From the calculations, we can extract the Berry phase from the argument of the matrix element $\langle -1_{\rm g}|\rho(\tau)|0_{\rm g}\rangle$, where τ is the traversal time of the STIRAP loop,

$$\mathrm{Arg}\left[\langle -1_{\rm g}|\rho(\tau)|0_{\rm g}\rangle\right] = \eta + \gamma_{\rm B}. \tag{C.15}$$

Here, η denotes the additionally acquired dynamical phase. To distinguish between the dynamical and the geometrical phase contributions, we apply the following procedure. Defining Pauli operators analogously to the previous case,

$$\begin{aligned}
\tau_x &= |0_{\rm g}\rangle\langle -1_{\rm g}| + |-1_{\rm g}\rangle\langle 0_{\rm g}|\,, \\
\tau_y &= -i\,|0_{\rm g}\rangle\langle -1_{\rm g}| + i\,|-1_{\rm g}\rangle\langle 0_{\rm g}|\,, \\
\tau_z &= |0_{\rm g}\rangle\langle 0_{\rm g}| - |-1_{\rm g}\rangle\langle -1_{\rm g}|\,,
\end{aligned} \tag{C.16}$$

we can extract the components of the state on the $|0_{\rm g}\rangle, |-1_{\rm g}\rangle$ Bloch sphere,

$$\begin{aligned}
X(t) &= \mathrm{Tr}[\tau_x\rho(t)], \\
Y(t) &= \mathrm{Tr}[\tau_y\rho(t)], \\
Z(t) &= \mathrm{Tr}[\tau_z\rho(t)].
\end{aligned} \tag{C.17}$$

We run the numerical calculation for different wedge angles Φ and fit the projection $X(\tau)$ after the STIRAP loop [Eqs. (C.34) and (C.35)] to

$$X(\tau) = A_1 + \mathcal{V}_1\cos(\eta_1 + \gamma_{\rm B}), \tag{C.18}$$

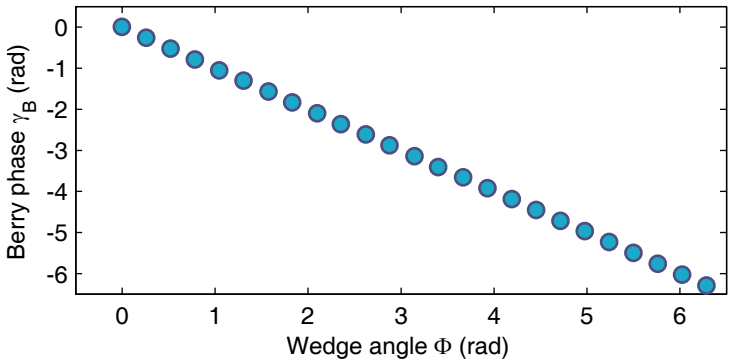

Figure C.2: Predicted Berry phase as a function of Φ. Berry phase as a function of the enclosed wedge angle Φ for a traversal time of $\tau = 1200$ ns, Rabi frequency $\Omega_R = 31\,\mathrm{MHz}$, detuning $\Delta = 60\,\mathrm{MHz}$, and an initial state $\rho(0) = 0.2\,|0_\mathrm{g}\rangle\langle 0_\mathrm{g}| + 0.8\,|-1_\mathrm{g}\rangle\langle -1_\mathrm{g}| + 0\,|+1_\mathrm{g}\rangle\langle +1_\mathrm{g}|$.

where the phase shift due to the dynamical phase η_1 is a free parameter. The Berry phase is then obtained by substracting η from Eq. (C.15), and the result, as a function of the enclosed wedge angle Φ, as shown in Fig. C.2. The numerical calculations thereby confirm the linear dependence of Eq. 4.1.

For the visibility of the Berry phase, we start with the same initial state as in Eq. (C.14), implement the first STIRAP loop, followed by a π pulse in the $|0_\mathrm{g}\rangle, |-1_\mathrm{g}\rangle$ subspace, and eventually apply the second STIRAP loop enclosing the negative wedge angle. We run the protocol for various wedge angles, similar to the single STIRAP case, and fit the component $X(2\tau)$ to

$$X(2\tau) = A_2 + \mathcal{V}_2 \cos(\eta_2 + 2\gamma_\mathrm{B}). \tag{C.19}$$

The visibility is then given by fit parameter $\mathcal{V}_2$ and is shown in Fig. C.3

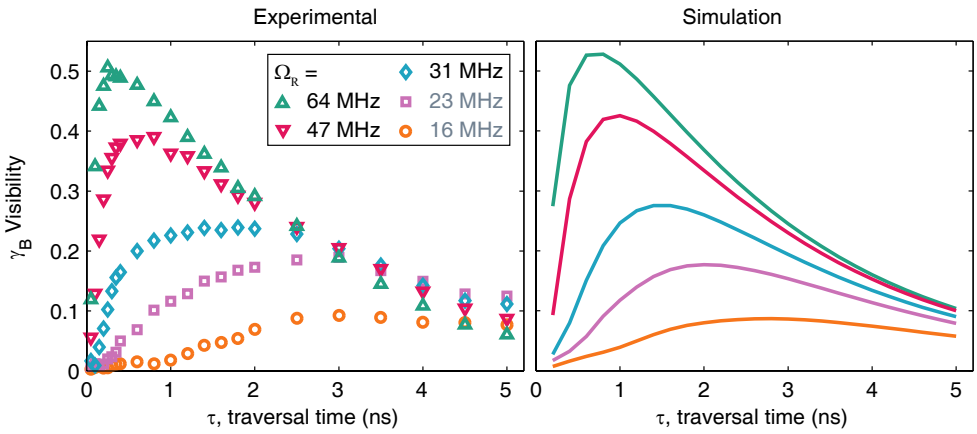

Figure C.3: Simulated Berry phase visibility. Visibility of the Berry phase γ_{B} [cf. Eq. (C.19)] as a function of the traversal time τ, for different peak Rabi frequencies Ω_{R}, compared to the experimental data shown in Fig. 4b of the main text. Simulations performed with corresponding values of the optical driving (Ω_R) are indicated by matching colors.

for various traversal times τ and peak Rabi frequencies Ω_{R} (cf. Fig. 4.11). The dynamic phase, η_2, is nominally zero as we actively cancel the dynamic phase in an echo sequence.

In a Λ system with a more energetically isolated excited state, improvements to visibility could be realized. This isolation is measured by the energy separation to the nearest excited state, ν_{ES} (2.9 GHz in our system), and sets a limit on the Zeeman-tuned separation of the lower levels of the Λ system, $\nu_{-1,+1}$ (655 MHz in our system). Ideally, $\nu_{-1,+1} \ll \nu_{ES}$ such that the stronger lower order harmonics do not drive additional transitions. This harmonic separation, $\nu_{-1,+1}$, then limits the maximum optical driving powers, Ω_R (64 MHz in our experiment), which would enable faster adiabatic evolution and minimize the effect of decoherence to improve vis-

ibility.

C.1.5 State fidelity

In the perfect case, the desired state to reach after the two STIRAP loop sequence is

$$|\psi(2\tau)\rangle = \frac{1}{\sqrt{2}}\left(|0_{\mathrm{g}}\rangle + e^{2i\gamma_{\mathrm{B}}}|-1_{\mathrm{g}}\rangle\right), \tag{C.20}$$

where the dynamical phase is perfectly cancelled. The fidelity F of the actual state of the system $\rho(2\tau)$ towards $|\psi(2\tau)\rangle$ is

$$F = \langle\psi(2\tau)|\,\rho(2\tau)\,|\psi(2\tau)\rangle\,. \tag{C.21}$$

The state $\rho(2t)$ can be generally written as

$$\rho(2\tau) = \rho_{0,0}\,|0_{\mathrm{g}}\rangle\langle 0_{\mathrm{g}}| + \rho_{0,-1}\,|0_{\mathrm{g}}\rangle\langle -1_{\mathrm{g}}| + \rho_{-1,0}\,|-1_{\mathrm{g}}\rangle\langle 0_{\mathrm{g}}| + \rho_{-1,-1}\,|-1_{\mathrm{g}}\rangle\langle -1_{\mathrm{g}}| + \ldots, \tag{C.22}$$

where the time dependence of the matrix elements has been omitted for clarity. The remaining matrix elements in Eq. (C.22) are not relevant for the further calculation. The fidelity is the calculated to be

$$\begin{aligned}
F &= \frac{1}{2}\left(\rho_{0,0} + \rho_{-1,-1} + e^{2i\gamma_{\mathrm{B}}}\rho_{0,-1} + e^{-2i\gamma_{\mathrm{B}}}\rho_{-1,0}\right)\\
&= \frac{1}{2}\left(\rho_{0,0} + \rho_{-1,-1} + 2\mathrm{Re}\left[e^{2i\gamma_{\mathrm{B}}}\rho_{0,-1}\right]\right)\\
&= \frac{1}{2}\left(\rho_{0,0} + \rho_{-1,-1} + 2\mathrm{Re}\left[\frac{1}{2}\Big(\cos(2\gamma_{\mathrm{B}}) + i\sin(2\gamma_{\mathrm{B}})\Big)\Big(X(2\tau) - iY(2\tau)\Big)\right]\right)\\
&= \frac{1}{2}\left(\rho_{0,0} + \rho_{-1,-1} + \Big(\cos(2\gamma_{\mathrm{B}})X(2\tau) + \sin(2\gamma_{\mathrm{B}})Y(2\tau)\Big)\right)\\
&= \frac{1}{2}\left(\rho_{0,0} + \rho_{-1,-1} + \mathcal{V}_2\right),
\end{aligned} \tag{C.23}$$

where $\mathcal{V}_2$ denotes the visibility [cf. Eq. (C.19), the parameter $A_2 \approx 0$ in the adiabatic case],

$$X(2\tau) = \mathcal{V}_2 \cos(2\gamma_{\mathrm{B}}) \tag{C.24}$$

$$Y(2\tau) = \mathcal{V}_2 \sin(2\gamma_{\mathrm{B}}). \tag{C.25}$$

C.2 Experimental details: Understanding the NV excited state

C.2.1 Excited state structure

The NV center in this experiment has an orbital strain splitting that varies between 6.8 and 7.4 GHz due to thermal cycling of the cryostat. This strain splits the excited state orbitals $|E_X\rangle$ and $|E_Y\rangle$. In addition, we apply an external 117 G magnetic field to split the ground state $|-1_g\rangle$ and $|+1_{\mathrm{g}}\rangle$ spin sublevels by $\nu_{-1,+1} = 655$ MHz. This leads to triplet ground state splittings of $\nu_{0,-1} = 2.550$ GHz, and $\nu_{0,+1} = 3.205$ GHz. The strain and magnetic field conditions described determine the full excited state structure of the NV center. In Figure C.4a, we plot the transitions between the $|0_{\mathrm{g}}\rangle$ and coupled excited states (blue), as well as the transitions between the ground $|-1_{\mathrm{g}}\rangle$ state and the coupled excited states (red). These transitions are determined through a photoluminescence excitation measurement with a tunable 637 nm narrow-line laser. The $|A_2\rangle$ excited state is the upper level of our lambda system, as it couples to both $|-1_{\mathrm{g}}\rangle$ and $|+1_{\mathrm{g}}\rangle$, and the strain

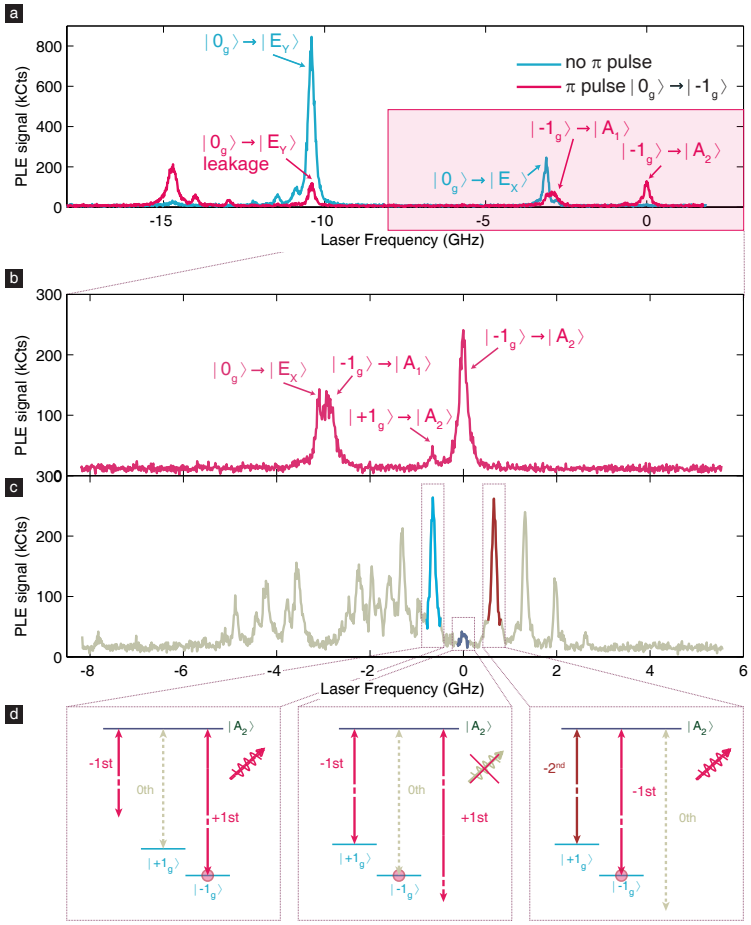

Figure C.4: NV center excited state via PLE. a) Transitions between the ground state and excited state of the NV center as seen in a photoluminescence excitation (PLE) measurement for an initial state $|0_g\rangle$ (blue) and $|-1_g\rangle$ (red). **b)** Zoom in of excited state transitions measured through PLE in the upper branch of the NV center excited state. The transitions that are pumped in the system are $|-1_g\rangle$ to $|A_2\rangle$ and $|+1_g\rangle$ to $|A_2\rangle$. **c)** PLE measurement with the the non-zero harmonics of the laser swept through the transitions reveals a convolution between the harmonic structure of the laser and the excited state structure of the NV center. Certain peaks are highlighted to indicate when harmonics are driving certain transitions as indicated in d. **d)** Cartoon of harmonic configurations that either pump the system emitting light (left and right) or in which the system already exists in the dark state (center).

and magnetic fields split the $|A_2\rangle$ level from the next highest level, $|A_1\rangle$, by 2.9 GHz. In Figure C.4b, we examine the excited state transitions closest to the $|-1_g\rangle$ to $|A_2\rangle$ transition, which include transitions to $|A_1\rangle$ and $|E_X\rangle$.

To generate sidebands on the tunable laser, we use a fiber-coupled electro-optic modulator (EOM), with harmonics at 655 MHz ($\nu_{-1,+1}$). These changes are done adiabatically in order to perform our STIRAP interaction. When the zeroth harmonic is extinguished, and we scan the laser across these various excited state transitions, we can get a snapshot of the harmonic structure of the laser convolved with the excited state structure, as seen in Fig. C.4c. Certain peaks are highlighted and a description of which sidebands correspond to particular transitions within the NV center level structure is provided in Fig. C.4d.

C.2.2 Branching ratios of $|A_2\rangle$ excited state

As $|A_2\rangle$ acts as the excited state of our Λ system, understanding its branching ratios is important for considering loss mechanisms in our optical Berry phase process. To do so, we selectively populate either $|-1_g\rangle$ or $|+1_g\rangle$ and pump on its respective transition to $|A_2\rangle$. As a function of pump time, we examine the decays into all three ground state spin sublevels ($|-1_g\rangle$,$|0_g\rangle$, $|+1_g\rangle$), plotted in Fig. C.5.

In each case, for the two spin sublevels not illuminated, the population

accumulates via $|A_2\rangle$, and we fit the measured counts, N_i, to

$$N_i = A_i e^{-B_i t} + C_i (i = 0, -1, +1) \tag{C.26}$$

From the data taken we determine the ratios of the change in the population of the ground state levels, where the change in the population is defined as $\Delta N_i = N_i(t \to \infty) - N_i(t = 0) = A_i$:

$$\frac{\Delta N_0}{\Delta N_{+1}} = 0.23 \quad \text{and} \quad \frac{\Delta N_0}{\Delta N_{-1}} = 0.3 \tag{C.27}$$

If we pump on the $|-1_g\rangle$ state, we assume the change in population of the other two ground state levels is related to the excited state population via:

$$\frac{dN_0}{dt} = \Gamma_0 N_{A_2} \quad \text{and} \quad \frac{dN_{+1}}{dt} = \Gamma_{+1} N_{A_2} \tag{C.28}$$

It then follows:

$$\frac{\Delta N_0}{\Delta N_{+1}} = \frac{\Gamma_0}{\Gamma_{+1}} \tag{C.29}$$

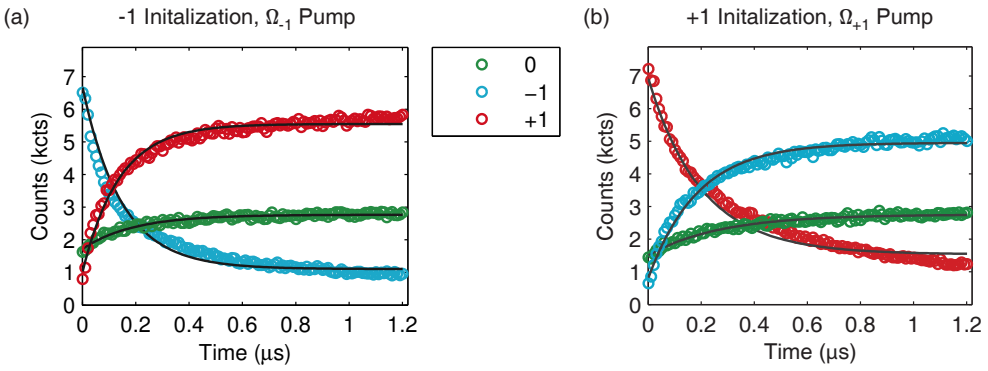

Figure C.5: Spin-dependent decay from $|A_2\rangle$. Time-resolved populations of the ground state spin sublevels as a function of optical pump time on **a)** an optical transition between $|-1_g\rangle \to |A_2\rangle$ with an initial state $|-1_g\rangle$ and on **b)** an optical transition between $|+1_g\rangle \to |A_2\rangle$ with an initial state $|+1_g\rangle$. The change in populations determine the branching ratios of $|A_2\rangle$.

And likewise for pumping on the $|+1_g\rangle$ state:

$$\frac{\Delta N_0}{\Delta N_{-1}} = \frac{\Gamma_0}{\Gamma_{-1}} \tag{C.30}$$

The total decay rate is given by the excited state lifetime:

$$\Gamma_0 + \Gamma_{+1} + \Gamma_{-1} = \Gamma_{GS} = \frac{1}{12 \text{ ns}} \tag{C.31}$$

Solving this system we obtain the following decay rates into the various ground state spin sublevels:

$$\begin{aligned} \Gamma_{+1} &= \frac{1}{24 \text{ ns}} \\ \Gamma_{-1} &= \frac{1}{31.2 \text{ ns}} \\ \Gamma_0 &= \frac{1}{104.2\text{ns}} \end{aligned} \tag{C.32}$$

C.3 Experimental details: STIRAP

C.3.1 Implementing STIRAP

We use STIRAP to adiabatically transport our dark state,

$$|D\rangle = \cos\left(\frac{\theta(t)}{2}\right)|-1_g\rangle - \sin\left(\frac{\theta(t)}{2}\right)e^{i\phi(t)}|+1_g\rangle \tag{C.33}$$

to enclose the wedge-like slices in the Bloch sphere of $|1_g\rangle$ and $|+1_g\rangle$, where $\theta(t) \in [0, 180°]$ and $\phi(t) \in [0, 360°]$ denote the polar and azimuthal angles of this sphere. To implement this procedure in our experiment, we modulate the microwaves driving an electro-optic modulator in order to change the relative amplitude and phase of the frequency sidebands on top of a carrier

frequency generated by a single-mode, narrow line tunable 637 nm laser. The driving microwaves are tuned to the separation of the $|-1_{\mathrm{g}}\rangle$ and $|+1_{\mathrm{g}}\rangle$ levels at $\nu_{-1,+1} = 655\,\mathrm{MHz}$. In our case, we use the zeroth harmonic, or fundamental, to pump the $|-1_{\mathrm{g}}\rangle$ to $|A_2\rangle$ transition, and the red-shifted first harmonic to drive the $|+1_{\mathrm{g}}\rangle$ to $|A_2\rangle$ transition. The harmonics of the electro-optic modulator follow the series of Bessel functions of the first kind, $J_n(x)$, such that our optical driving fields are defined as,

$$\Omega_{-1}(t) = J_0\big(g(t)\cdot r_1\big) \tag{C.34}$$

$$\Omega_{+1}(t)e^{-i\phi_0(t)} = J_1\big(g(t)\cdot r_1\big)e^{-i\phi_0(t)} \tag{C.35}$$

where r_1 is the first root of $J_0(x)$. This factor accounts for the preset microwave amplification that extinguishes the fundamental harmonic when $g(t) = 1$ (i.e. $g(t) = 1 \rightarrow \Omega_{-1}(t) = 0$). For our experiments, we use a sinusoidal microwave pulse to transport the dark state from one pole to the other and back again,

$$g(t) = \frac{\cos\left(\frac{2\pi t}{\tau}\right) + 1}{2} \tag{C.36}$$

where τ is the traversal time of our STIRAP interaction. From this, we see that the ideal trajectory of the dark state can be given by the following azimuthal and polar angle trajectories as a function of time,

$$\phi_0(t) = \phi_i + \Phi\cdot H\left(t - \frac{\tau}{2}\right) \tag{C.37}$$

$$\theta_0(t) = 2\tan^{-1}\frac{\Omega_{-1}(t)}{\Omega_{+1}(t)} \tag{C.38}$$

where $H(t)$ is the Heaviside step function, ϕ_i is the relative phase between the sidebands for the first half of the trajectory, and Φ, the wedge angle, is the increment added to the phase for the second half of the trajectory.

C.3.2 Quantum state tomography of the STIRAP path

To perform the time-resolved state tomography measurements (seen in Fig. 4.3) which are used to reconstruct the path of the dark state on the $|-1_g\rangle/|+1_g\rangle$ Bloch sphere, we use the pulse sequence shown in Fig. C.6, similar to time-resolved state tomography done Chapters 3 and 5. The sequence consists of 121 distinct time interruptions of a 1200 ns STIRAP interaction, resulting in a time resolution of 10 ns. For all sequences discussed in this appendix, we begin with a standard 532 nm laser pulse to reset the charge state and initialize NV center into $|0_g\rangle$. The population is then transferred from $|0_g\rangle$ to $|-1_g\rangle$ with a π pulse, tuned to 2.55 GHz ($\nu_{0,-1}$). A specific time-resolution of STIRAP is performed to bring the dark state into a particular $|-1_g\rangle$ and $|+1_g\rangle$ superposition. We then transfer the population in $|-1_g\rangle$ back to $|0_g\rangle$, leaving the spin state in a $|0_g\rangle$ and $|+1_g\rangle$ superposition. From there we perform state tomography on the spin state, measuring X, Y, and Z projections using $\pi/2$ pulses tuned to 3.205 GHz ($\nu_{0,+1}$) and a second 637 nm laser tuned to the $|0_g\rangle$ to $|E_X\rangle$ transition to read out the population in $|0_g\rangle$.

From those projections, we reconstruct the path of the spin on the Bloch sphere as seen in Fig. 4.3. Total magnitude of the vector may exceed 1, as all projections are normalized by the initial state of the spin, which is imperfectly initialized into $|-1_g\rangle$. In addition, an overall decrease in total counts is observed as the STIRAP duration increases due to loss out of the $|-1_g\rangle$ and $|+1_g\rangle$ subspace. To correctly evaluate the length of the projections we find the average of the $+Z$ and $-Z$ projections. This average corresponds to the center of the $|-1_g\rangle$ / $|+1_g\rangle$ Bloch sphere and all projections are measured from this point.

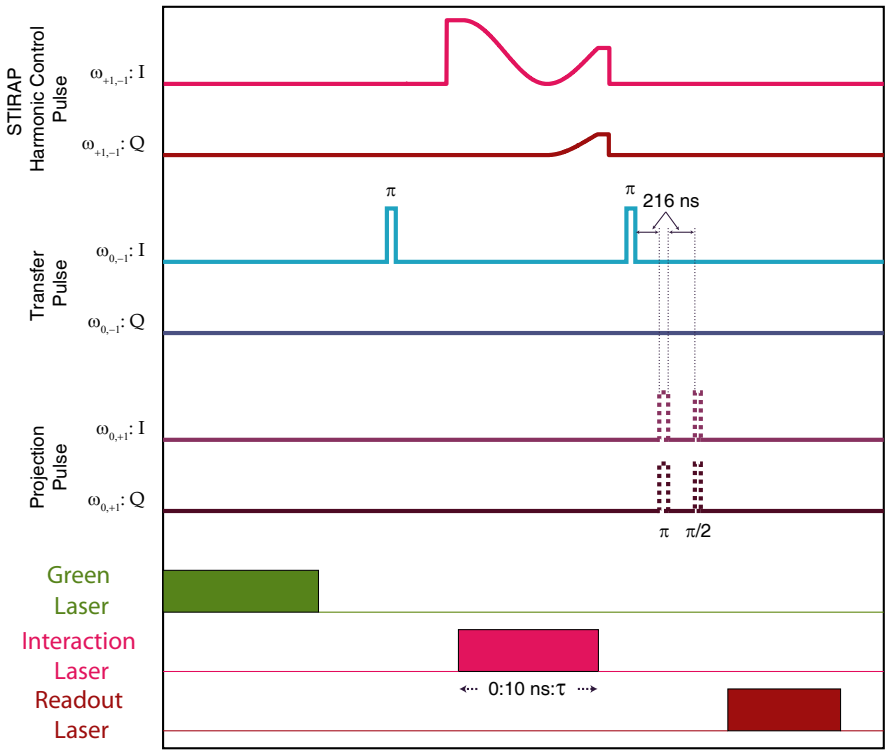

Figure C.6: Pulse sequence for time-resolved tomography of STIRAP. Green laser (532 nm) pulse initializes the spin into $|0_g\rangle$. π pulse tuned to $\nu_{0,-1}$ transfers the spin to $|-1_g\rangle$. Interaction laser (637 nm coupled to EOM) pulse duration varies for different iterations of the experiment to reveal time dynamics of the spin during STIRAP which moves the spin around the $|-1_g\rangle$ / $|+1_g\rangle$ Bloch sphere. The spin ends up in a superposition of $|-1_g\rangle$ and $|+1_g\rangle$. A second π pulse also tuned to $\nu_{0,-1}$ transfers the portion in $|-1_g\rangle$ to $|0_g\rangle$ resulting in a superposition state of $|0_g\rangle$ and $|+1_g\rangle$. This state is then read out through state tomography, consisting of X, Y, and Z projections using a $\pi/2$ pulse tuned to $\nu_{0,+1}$ which are read out through a second resonant 637 nm read-out laser tuned to the $|0_g\rangle$ to $|E_X\rangle$ to read out the population in $|0_g\rangle$.

C.4 Experimental details: Berry phase accumulation

C.4.1 Pulse sequence

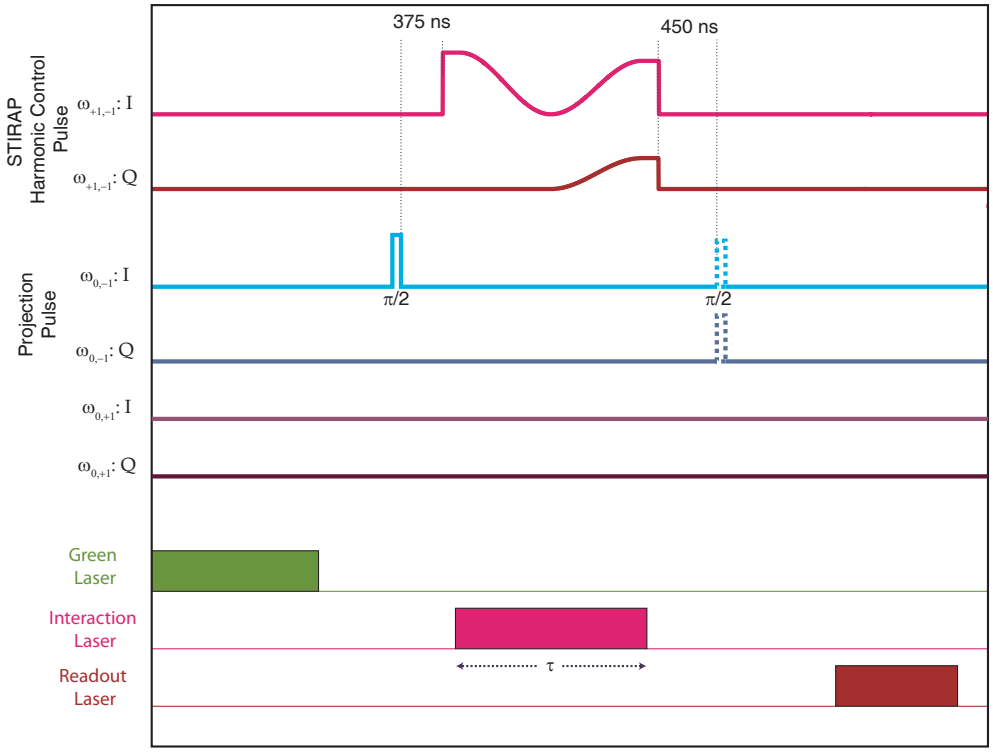

Figure C.7: Pulse sequence for Berry phase accumulation. 532 nm laser pulse initializes the spin into $|0_g\rangle$. $\pi/2$ pulse tuned to $\nu_{0,-1}$ transfers the spin to the equator of the $|0_g\rangle/|-1_g\rangle$. STIRAP laser (637 nm coupled to EOM) pulse encloses a wedge angle Φ on the $|-1_g\rangle$ /$|+1_g\rangle$ Bloch sphere. A second $\pi/2$ pulse tuned to $\nu_{0,-1}$ either projects the X or Y component of the final state. This state is then read out through a second resonant 637 nm tuned to the $|0_g\rangle$ to $|E_X\rangle$ to read out the population in $|0_g\rangle$, resulting in X and Y projections detailing the phase accumulation due to STIRAP.

To measure the accumulation of Berry phase, γ_B, (Figs. 4.6 - 4.9) we

use the following pulse sequence (Fig. C.7), the details of which are largely described in the main text. This measurement sequence includes contributions from a dynamic phase that is fixed for all wedge angles. Unlike the previous pulse sequence, in addition to the preparation pulse, the projection pulses are also on the $|0_g\rangle$ and $|-1_g\rangle$ Bloch sphere. Because of nuclear effects, the projection pulse must occur at a time when the nuclear hyperfine states of the NV center rephase, around 450 ns after the end of the STIRAP interaction, as described in §B.2. This sequence is performed for a variety of intended γ_B angles. The resulting projections are normalized by the difference in the measure of the photon counts emitted when the spin is intialized into $|0_g\rangle$ versus $|-1_g\rangle$, such that the normalization factor, $N_{diff} = N_{|0_g\rangle} - N_{|-1_g\rangle}$.

C.4.2 Understanding the dynamic phase

To understand the origin of the dynamic phase, η, we perform a series of Berry phase enclosure measurements (12 different wedge angles, Φ) while varying the two-photon detuning, δ, traversal time, τ, and optical Rabi frequency, Ω_R. For a given Ω_R and δ, we perform these Berry phase measurements at five different τ (200, 400, 600, 800, and 1000 ns). For each τ, the resulting projections are then fit to determine the fixed dynamic phase. In Fig. C.8, we plot the dynamic phase accumulated at $\Omega_R = 31$ MHz, for increasing τ at various δ.

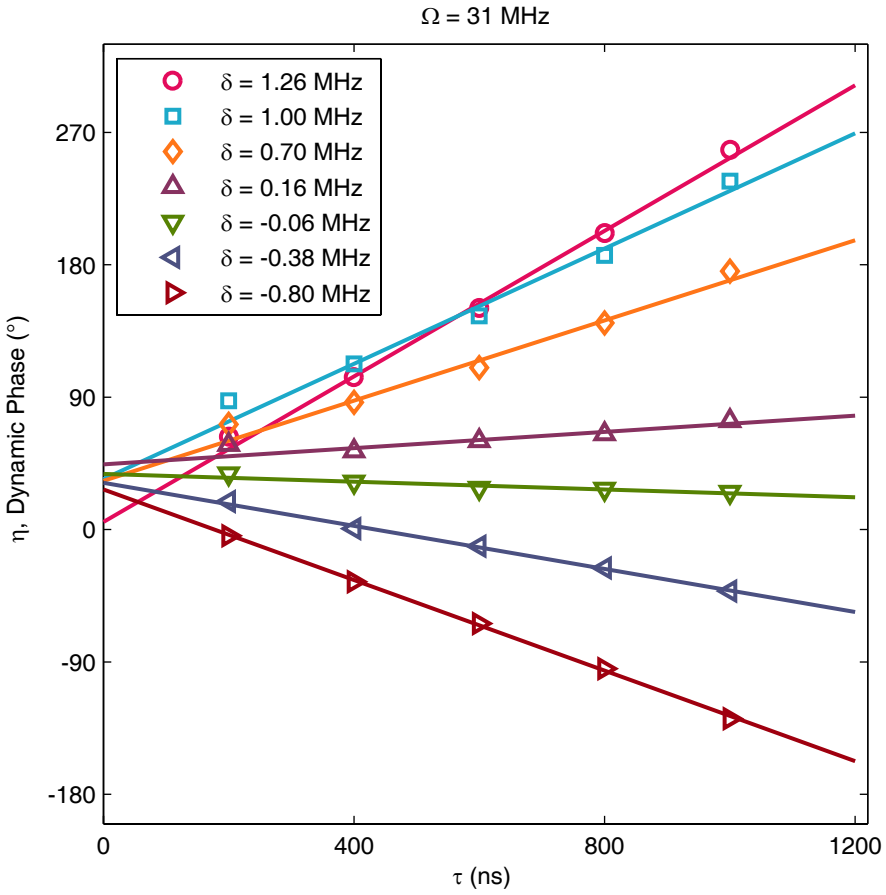

Figure C.8: Accumulated dynamic phase, η, due to τ and δ. Measured dynamic phases for a given two-photon detuning, δ, at various STIRAP traversal times, τ taken at a $\Omega_R = 31$ MHz. For each detuning a slope, $d\eta/d\tau$, is found resulting in a Stark frequency shift, Σ_η, which is plotted in Fig. 4.10. This data is representative of similar sets taken at $\Omega_R = 64, 47$, and 23 MHz, and the resulting Σ_η/δ for those sets is plotted in the inset of Fig. 4.10.

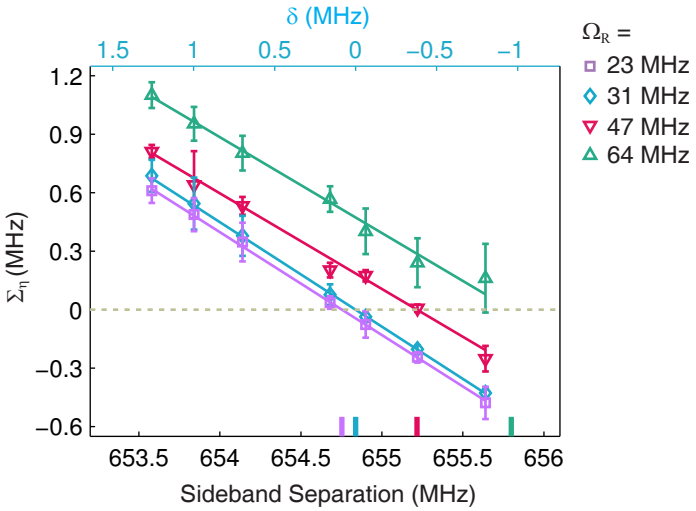

Figure C.9: Dark state Stark shift as a function of two-photon detuning. The resulting Σ_η as a function of absolute sideband frequency separation for $\Omega_R = 64$, 47, 31, and 23 MHz. The data reveal a linear dependence of the energy shift on the two-photon detuning with similar slopes across all four values of Ω_R showing that the dynamic phase results from an optical stark effect. The data also reveal an unexplained shift in the point of two-photon resonance, $\delta = 0$.

For each δ, we fit the slope, $d\eta/d\tau$, of the acquired phase over time, and derive the respective frequency shift, $\Sigma_\eta = +1/(360°)\ d\eta/d\tau$, of the dark state energy. We then plot the frequency shifts as a function of absolute sideband frequency separation, in Fig. C.9. We find that all have similar slopes ($\Sigma_\eta/\delta \approx 0.55$) as a function of sideband frequency separation, but the two-photon resonance, $\delta = 0$, shifts to a higher sideband frequency separation for increasing optical Rabi frequency. This shift is not fully understood, but may be due to an additional optical Stark effect separating the $|-1_g\rangle$ and $|+1_g\rangle$ states from one another.

To derive the relationship of the dark state frequency (energy) shift, we

begin with the dark eigenstate at $\delta = 0$,

$$|D\rangle = \cos\left(\frac{\theta(t)}{2}\right)|-1_g\rangle - \sin\left(\frac{\theta(t)}{2}\right)e^{i\phi(t)}|+1_g\rangle. \tag{C.39}$$

We then apply a perturbation Hamiltonian, assuming small two-photon detuning, δ, given by:

$$V = h\delta|+1_g\rangle\langle+1_g| \tag{C.40}$$

Through first order perturbation theory the modification to the dark state energy should be:

$$E_{|D\rangle,V} = \langle D|V|D\rangle = h\delta sin^2\left(\frac{\theta(t)}{2}\right) \tag{C.41}$$

The energy shift of the dark state has no dependence on the azimuthal trajectory of the dark state, $\phi(t)$, but only on the polar trajectory, $\theta(t)$. Given our path as defined in Equations C.37 and C.38, we find that the energy shift of the dark state has no dependence on either the wedge angle, Φ, or the maximal optical Rabi frequency, Ω_R, and it only relies on the ratio of the pumps as a function of time, $(\Omega_{-1}(t))/(\Omega_{+1}(t))$. Taking the time average of our path, we find:

$$\Sigma_\eta = \frac{\langle E_{|D\rangle,V}\rangle}{h} = 0.55\delta \tag{C.42}$$

This figure is in good agreement with our data regarding the dynamic phase accumulation as a function of two-photon detuning, δ, as seen in Fig. 4.10.

C.5 Experimental details: echoed Berry phase accumulation

C.5.1 Pulse Sequence

As mentioned in the Ch. 4, we use a Hahn echo sequence to cancel out the dynamic phase contribution to focus on the Berry phase accumulation. In addition to cancelling out the dynamic phase, it also eliminates a decrease in visibility due to pumping out of the $|-1_g\rangle$ and $|+1_g\rangle$ subspace and into $|0_g\rangle$. While such pumping still persists in a Hahn echo, the secondary effect of moving the state away from the equator is eliminated, providing the fullest visibility at the equator. The pulse sequence we use (for Figs. 4.11 - 4.15) is seen in Fig. C.10. This sequence is also used for the noise robustness experiments. An example set of $\delta\phi$ noise is plotted on the STIRAP harmonic control pulse.

C.5.2 Estimating the true distribution of Berry phase

In Ch. 4, we show both the shot-noise broadened distributions of four Berry phase, $\hat{\sigma}_{\gamma_B,echo}$, shown in Fig. 4.13, along with a corrected, σ_{γ_B}, (see Figure 4.15), where the shot noise contribution from the broadened distribution has been subtracted in quadrature. In this section, we will discuss in more detail how we estimate and correct for the shot noise contribution.

For each of our noise profile experiments, we take a zero-noise Berry phase calibration measurement along with a Berry phase calibration at a given noise amplitude, s_θ and s_ϕ, all at a given wedge angle, Φ to extract the

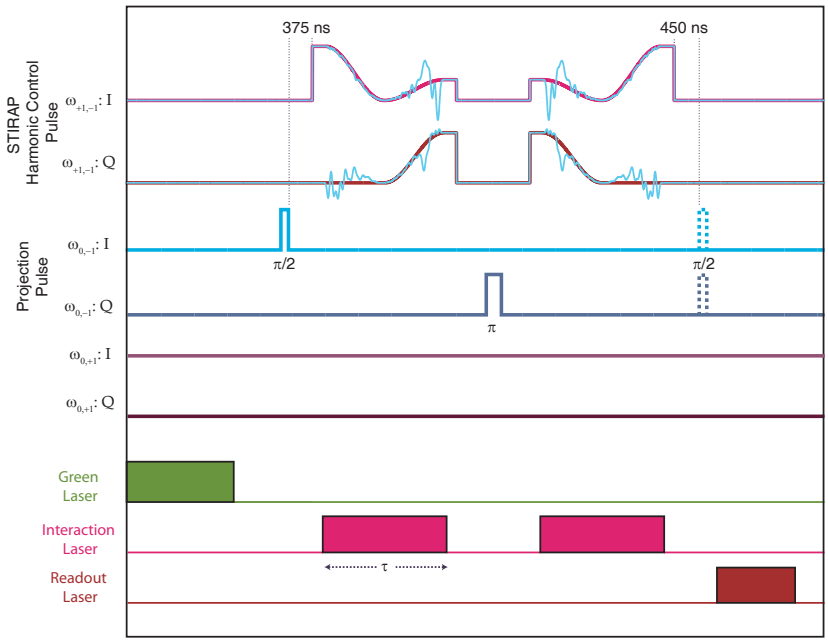

Figure C.10: Pulse sequence for Berry phase Hahn echo. 532 nm nm laser pulse initializes the spin into $|0_g\rangle$. $\pi/2$ pulse tuned to $\nu_{0,-1}$ transfers the spin to the equator of the $|0_g\rangle / |-1_g\rangle$. STIRAP laser (637 nm coupled to EOM) pulse performs a positive loop enclosing $\gamma_{B,1} = -\Phi$ on the $|-1_g\rangle / |+1_g\rangle$ Bloch sphere, and a total phase of $\xi_1 = \gamma_{B,1} + \eta$. A π pulse tuned to $\nu_{0,-1}$ then flips the sign of that acquired phase. A second STIRAP pulse performs a negative loop enclosing $\gamma_{B,2} = \Phi$ on the $|-1_g\rangle / |+1_g\rangle$ Bloch sphere, resulting in an additional phase of $\xi_2 = \gamma_{B,2} + \eta$. The total phase acquisition on the $|0_g\rangle / |-1_g\rangle$ Bloch sphere is then $\xi = -\xi_1 + \xi_2 = \gamma_{B,echo} = 2\Phi$. A final $\pi/2$ pulse tuned to $\nu_{0,-1}$ projects the X, $-X$, Y, or $-Y$ component of the final state. This state is then read out through a second resonant readout laser (637 nm) tuned to the $|0_g\rangle$ to $|E_X\rangle$ to read out the population in $|0_g\rangle$, resulting in differential X and Y projections detailing the phase accumulation due to STIRAP.

mean value for the $\pm X$ and $\pm Y$ projections. Along with these calibrations we take 250 instances of noise conforming to an Ornstein-Uhlenbeck process for a given noise amplitude.

We fit the zero noise calibration set to following fit functions,

$$\begin{aligned} X_+ &= A_X \cos(2\Phi) + \overline{X_+} \\ Y_+ &= A_Y \sin(2\Phi) + \overline{Y_+} \\ X_- &= -A_X \cos(2\Phi) + \overline{X_-} \\ Y_- &= -A_Y \sin(2\Phi) + \overline{Y_-} \end{aligned} \tag{C.43}$$

where A_X and A_Y are the amplitudes for the X and Y projections, and $\overline{X_+}$,$\overline{Y_+}$,$\overline{X_-}$, and $\overline{Y_-}$ are the offsets for $\pm X$ and $\pm Y$ respectively. Note that since we are using a Hahn echo sequence, we do not include a dynamic phase (η) component as this should effectively be cancelled out. This also means that $\gamma_{B,echo} = 2\Phi$ as we enclose a loop on either side of the Hahn echo sequence.

We then offset the $\pm X$ and $\pm Y$ for each instance of noise by their respective zero noise mean values, and take the differential to compute the X_{diff} and Y_{diff} components,

$$\begin{aligned} X_{diff} &= (X_{+,noise} - X_{-,noise}) - \left(\overline{X_+} - \overline{X_-}\right) \\ Y_{diff} &= (Y_{+,noise} - Y_{-,noise}) - \left(\overline{Y_+} - \overline{Y_-}\right) \end{aligned} \tag{C.44}$$

and extract

$$\gamma_{B,noise} = \tan^{-1}\left[\frac{Y_{diff}}{X_{diff}}\right]. \tag{C.45}$$

We find that even though the individual offsets vary across different noise profiles, the differences in the offsets, $\left(\overline{X_+} - \overline{X_-}\right)$ and $\left(\overline{Y_+} - \overline{Y_-}\right)$, remain constant and approximately equal to the zero-noise case. We also set the integration time of each noise profile such that the differential contrast is greater than 1000 counts for sufficient averaging.

The resulting data and distributions are shown in Fig. C.11 for an example s_ϕ profile. The distribution of $\gamma_{B,echo}$ is Gaussian in nature (Fig. C.11b), and we extract the normal distribution parameters, the mean, $\mu_{\gamma_{B,echo}}$, and the standard deviation, $\hat{\sigma}_{B,echo}$. However, the value of $\hat{\sigma}_{B,echo}$ is still broadened by the shot noise. In order to compensate for this we use the distribution of the error in $\gamma_{B,echo}$ (Fig. C.11c), which is equivalent to the shot noise of the measurement. While this distribution is not quite Gaussian in nature, we simplify by estimating μ_{shot} as the median of the distribution, and the width, σ_{shot}, from the standard deviation. We then estimate the 95% confidence error on the mean of the distribution as

$$2\sigma_{\mu,shot} = 2\frac{\sigma_{shot}}{\sqrt{N}}. \tag{C.46}$$

Also worth noting, all standard deviations of the distributions, σ_i, are quoted as true single σ's, where as all errors are quoted as 95% confidence intervals (2σ).

We use these values to calculate the corrected value of σ_{γ_B} by subtract-

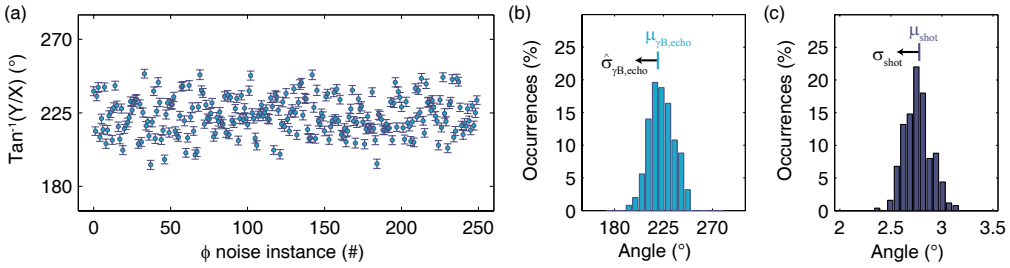

Figure C.11: Noise distribution of $s_\phi = 8°$. **a)** The distribution in $\tan^{-1}(Y_{diff}/X_{diff})$ values for the 250 unique instances of $s_\phi = 8°$ where X and Y are the differential contrasts defined above. **b)** A histogram of these measured angular values for $\gamma_{B,echo}$. The standard deviation $\hat{\sigma}_{\gamma_{B,echo}}$ is derived from this distribution **c)** A histogram of the distribution of the error of $\gamma_{B,echo}$. The value μ_{shot} and its error are derived from this distribution.

ing the shot noise component,

$$\sigma_{\gamma_B} = \frac{\sqrt{\hat{\sigma}^2_{\gamma_B,echo} - \mu^2_{shot}}}{2}. \tag{C.47}$$

We divide the value by two to account for the distribution that develops after only one loop within the Hahn echo is performed.

C.5.3 Relationship of Berry phase variance to applied noise

To investigate the robustness of the optically accumulated Berry phase to fluctuations in the two Rabi laser fields, we introduce deviations $\delta\theta$ and $\delta\phi$ to the ideal control trajectory, simulating fluctuations in the relative amplitude and phase, respectively, of the two laser fields. The deviations $\delta\theta$ and $\delta\phi$ conform to a Ornstein-Uhlenbeck (O.U.) process, characterized by a Lorentzian spectrum of frequencies with a bandwidth $\Delta\nu$ and a Gaussian

distribution of amplitudes with mean zero and standard deviation $s_i = \sqrt{P_i}\,(i = \theta, \phi)$, where P_i is the noise power. Under the assumption that the state trajectory follows the noise deviations adiabatically, the statistics of the measured Berry phase can be related to the statistics of the applied noise following the theoretical framework presented in Ref. [90]. When this calculation is extended to our STIRAP-accumulated Berry phase, we find that the relationship between the variance of the Berry phase to the power of fluctuations in ϕ is independent of geometric factors, in contrast to previous results for two level qubits in a bias field [90, 91]. We verify this prediction experimentally in Fig. 4.15 of the main text.

In STIRAP, the dark state

$$|D\rangle = \cos\left(\frac{\theta(t)}{2}\right)|-1_{\mathrm{g}}\rangle - \sin\left(\frac{\theta(t)}{2}\right)e^{i\phi(t)}\,|+1_{\mathrm{g}}\rangle \tag{C.48}$$

is adiabatically transported to enclose a wedge-like slice in the Bloch sphere of $|-1_{\mathrm{g}}\rangle$ and $|+1_{\mathrm{g}}\rangle$. The Berry connection, a local gauge potential for the Berry phase, can be determined for the dark state. The components of this Berry connection, $\vec{A}_{\vec{R}} = i\langle D| \bigtriangledown_{\vec{R}} |D\rangle$, with $\vec{R} = (\theta, \phi)$, are calculated as

$$\begin{aligned} A_\theta &= 0 \\ A_\phi &= -\frac{1}{2}\left(1 - \cos\left(\theta\right)\right). \end{aligned} \tag{C.49}$$

The Berry phase $\gamma_B = \int_{R_i}^{R_f} \vec{A}_{\vec{R}} \cdot d\vec{R}$ can be Taylor expanded about the ideal trajectory by considering $\theta(t) = \theta_0(t) + \delta\theta(t)$ and $\phi(t) = \phi_0(t) + \delta\phi(t)$, where $\theta_0\,(\phi_0)$ specifies the unperturbed trajectory, and $\delta\theta\,(\delta\phi)$ is the

applied stochastic noise. The ideal trajectories corresponding to a wedge of opening angle Φ on the Bloch sphere are given by equations C.37 ($\phi_0(t)$), and C.38 ($\theta_0(t)$). For tractability in this calculation, we apply a linear approximation to the ideal $\theta_0(t)$, using

$$\theta_0(t) = \begin{cases} \frac{2\pi t}{\tau} \left(0 < t < \frac{\tau}{2}\right) \\ 2\pi \left(1 - \frac{t}{\tau}\right) \left(\frac{\tau}{2} < t < \tau\right) \end{cases} \tag{C.50}$$

The ideal $\theta_0(t)$, along with its approximation for this calculation, is shown in Fig. C.12.

Following Ref. [90], the total Berry phase assuming adiabatic following of the noise is

$$\begin{aligned} \gamma_B &= \int_0^\tau \left[A_\phi(\theta_0) + \delta A_\phi\right] \left(\dot{\phi}_0 + \delta\dot{\phi}\right) dt \\ &\cong \gamma_B^0 + \int_0^\tau \left(\delta A_\phi \dot{\phi}_0 dt\right) + \int_0^\tau A_\phi(\theta_0)\delta\dot{\phi} dt \end{aligned} \tag{C.51}$$

where γ_B^0 is intended Berry phase in the absence of noise and we have neglected second order corrections in the fluctuations. Using Eq. C.49,

$$\delta A_\phi = -\frac{\sin\left(\theta_0\right)}{2}\delta\theta, \tag{C.52}$$

and using Eq. C.37,

$$\dot{\phi}_0 = \Phi \cdot \delta(t - \tau/2), \tag{C.53}$$

where $\delta(t)$ denotes the Dirac delta function. The term $\int_0^T \delta A_\phi \dot{\phi}_0 dt$ therefore is zero since $\sin\left(\theta_0(\tau/2)\right) = \sin\left(\pi\right) = 0$ and implies that the Berry

phase is robust against deviations $\delta\theta$ to first order. Writing out the remaining term, we find

$$\begin{aligned}\delta\gamma_B = \gamma_B - \gamma_B^0 &= -\int_0^\tau \frac{1}{2}\left(\cos\left(\theta_0(t)\right) - 1\right)\delta\dot{\phi}dt \\ &= -\frac{1}{2}\int_0^\tau \cos\left(\frac{2\pi t}{\tau}\right)\delta\dot{\phi}dt \end{aligned} \tag{C.54}$$

where we have set the part corresponding to the total derivative $\int_0^T \delta\dot{\phi}dt = \delta\phi(T) - \delta\phi(0) = 0$ since $\delta\phi(T) = \delta\phi(0) = 0$ due to the envelope function we apply to the noise (shown in Fig C.12b), in order to maintain adiabaticity when turning on and off the noise. Eq. C.54 can further be simplified using integration by parts to yield

$$\begin{aligned}\delta\gamma_B &= -\frac{1}{2}\cos\left(\frac{2\pi t}{\tau}\right)\delta\phi|_0^\tau - \frac{1}{2}\int_0^\tau \frac{2\pi}{\tau}\sin\left(\frac{2\pi t}{\tau}\right)\delta\phi dt \\ &= -\frac{\pi}{\tau}\int_0^\tau \sin\left(\frac{2\pi t}{\tau}\right)\delta\phi dt. \end{aligned} \tag{C.55}$$

When $\delta\phi$ is a stochastic random variable under an O.U. process, we find the mean Berry phase deviation $\langle\delta\gamma_B\rangle = 0$ and that its variance $\langle{\delta\gamma_B}^2\rangle$ can be computed as

$$\begin{aligned}\langle{\delta\gamma_B}^2\rangle &= \left(\frac{\pi}{\tau}\right)^2 \int_0^\tau \int_0^\tau \sin\left(\frac{2\pi t^{'}}{\tau}\right)\sin\left(\frac{2\pi t^{''}}{\tau}\right)\langle\delta\phi^{'}\delta\phi^{''}\rangle dt^{'}dt^{''} \\ &= \left(\frac{\pi}{\tau}\right)^2 \int_0^\tau \int_0^\tau \sin\left(\frac{2\pi t^{'}}{\tau}\right)\sin\left(\frac{2\pi t^{''}}{\tau}\right) P_\phi \exp\Big(-2\pi\Delta\nu|t^{''} - t^{'}|\Big) dt^{'}dt^{''} \end{aligned} \tag{C.56}$$

where we have used the fact that the auto-correlation function $\langle\delta\phi^{'}\delta\phi^{''}\rangle = P_\phi \exp\big(-2\pi\Delta\nu|t^{''} - t^{'}|\big)$ for O.U. random variables of power P and band-

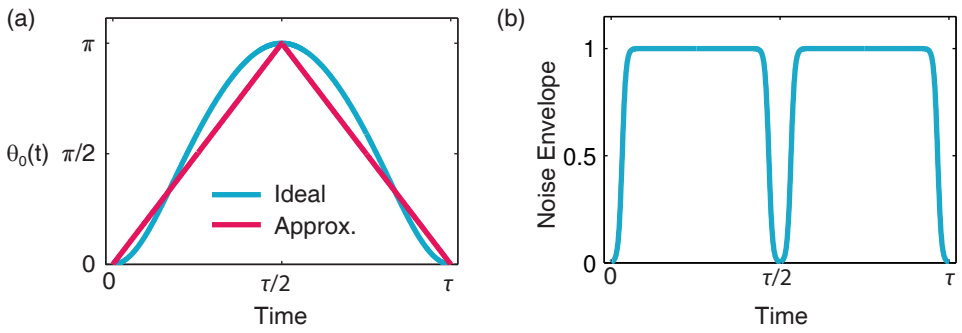

Figure C.12: Trajectory of $\theta_0(t)$ and noise envelope a) The ideal $\theta_0(t)$ trajectory (blue) is given by ratio of amplitudes of two harmonics produced by an electro-optic modulator. For the purpose of the calculation, a linear approximation (red) is used. **b)** The O.U. noise time series $\delta\theta$ or $\delta\phi$ are multiplied by an envelope function that goes to 0 at $t = 0, \tau/2, \tau$. This envelope function ensures adiabaticity when the noise is turned on and off, and when the wedge angle is opened.

width $\Delta\nu$. The last integral can be evaluated to yield the final relation

$$\sigma^2_{\gamma_B} = \langle \delta\gamma_B^2 \rangle = \frac{P_\phi}{2}\left[\frac{1 - e^{-2\pi\Delta\nu\tau}}{(1 + (\Delta\nu\tau)^2)^2} + \frac{\pi\Delta\nu\tau}{1 + (\Delta\nu\tau)^2}\right], \tag{C.57}$$

showing the statistical variation of the Berry phase to only depend on P_ϕ and the product $\Delta\nu\tau$, and not on the geometric factors that determine the value of the Berry phase itself. In Fig. 5d of the main text, we report the experimentally measured Berry phase standard deviations σ_{γ_B} for both θ and ϕ noise for various noise amplitudes s_i and constant Lorentzian bandwidth $\Delta\nu = 3\,\text{MHz}$. Together with the STIRAP cycle time of τ =1.2 µs, Eq. C.57 predicts an expected relation of $\sigma^2_{\gamma_B} = 0.41P_\phi = 0.41s^2_\phi$, or $\sigma_{\gamma_B} = 0.64s_\phi$, which is seen to reasonably agree with the measured data. In Fig. 5e of the main text, we vary the product $\Delta\nu\tau$ experimentally for

constant P_ϕ and confirm the behavior of Eq. C.57.

Appendix D

Unanswered questions

As is to be expected with any scientific endeavor, there always exist unanswered questions. These are interesting and unexpected effects that appear during the course of an experiment for which no explanation is immediately obvious or abundantly crucial to the task at hand. In the context of the work presented in this thesis, we have stumbled upon our own fair share of curiosities that have eluded explanation and are discussed below.

D.1 The role of the 405 nm repump

During the experiments discussed in Chapter 2 probing the effect of applied electric fields on NV center orbital transitions, we discovered some very interesting charging behavior. As discussed, the 532 nm (2.3 eV) laser light would photoionize charge traps within the diamond. With the application of voltages to the lithographic gates on the sample, we observe a long-lived nonequilibrium charge distribution that cause an amplification or screening

of the local electric field. We attribute this effect, in particular, to the photoionization of substitutional nitrogen atoms as they lie $\approx 1.7-2.2$ eV below the conduction band [66, 67, 68].

While this is the crux of the photoinduced field discussed, these traps remain charged for long periods of time, and full relaxation with 532 nm would take several hours. To combat this, we discovered that the application of 405 nm (3.1 eV) would significantly alter the charging behavior of the system. Most importantly, it acted as a "reset" of the equilibrium charge distribution with no applied voltage. As such, we would apply a pulse of 405 nm laser light (≈ 10 μW) to fully relax the charge traps within ≈ 10 s for all experiments discussed in Chapter 2.

However, the actual dynamics resulting from the application of the 405 nm were briefly explored, but never fully explained. In general, we found that the NV center optical transitions were somewhat less stable - i.e. for several NV centers, more spectral diffusion of the optical transitions was observed. In addition, we also observed more screening of the applied electric field than with the 532 nm light. Some NV centers even exhibited screening of the applied field in both directions out to magnitudes of $|100$ V$|$.

In Fig. D.1a, we plot the Stark shift response of the same NV center as shown in Fig. 2.3 (reproduced in Fig. D.1b for comparison), but with the application of 405 nm light. We note that instead of the amplification

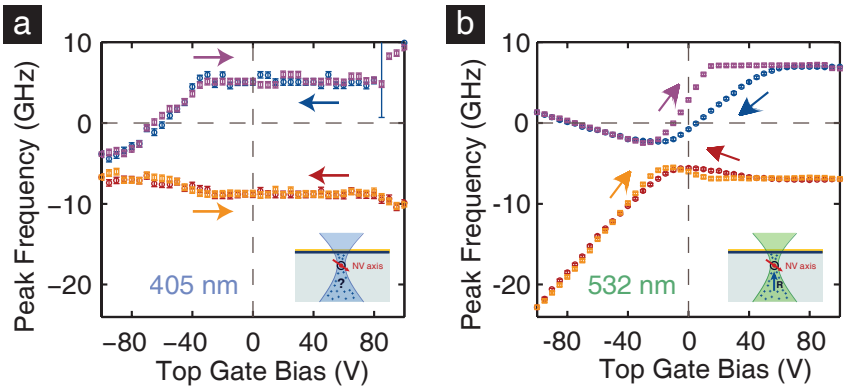

Figure D.1: Response of optical transitions to external voltages under 405 nm **illumination a)** Under 405 nm illumination, the Stark-shift response of NV center optical transitions for an NV center 13 μm below a transparent top gate, as a function of top-gate voltage stepped in a loop over ≈ 160 min. **b)** Under 532 nm illumination, the Stark-shift response of NV center optical transitions for an NV center 13 μm below a transparent top gate, as a function of top-gate voltage stepped in a loop over ≈ 160 min.

for negative applied voltages and screening for positive applied voltages above a threshold bias seen in 532 nm light, we find the threshold bias for 405 nm light exists at a negative voltage, ∼ 40 V. In addition, the hysteresis present for 532 nm light is significantly reduced for 405 nm light, a result of the much faster relaxation times under 405 nm illumination. In addition, we observe an unusual inability to screen the electric field for large positive voltages. This feature was repeatedly seen on a number of NV centers in several different samples. However, other NV centers exhibited screening across the entire range of applied voltages with 405 nm light. Some of these discrepancies could be due to different annealing conditions of samples affecting the charge traps and Fermi level within the diamond

and/or mounting approaches that ground the back of the sample; however, it is clear, the behavior is quite different from the behavior under 532 nm illumination.

Perhaps different charge traps are photoexcited by the more energetic 405 nm light, such as vacancies or N3 centers. The screening of both positive and negative voltages is also puzzling. Finally, the relaxation time constant of the charge traps photoexcited by the 405 nm is much faster than under 532 nm illumination. Clearly, there is some interesting physics occuring within the diamond that may be interesting to probe.

D.2 Decoherence within a driven Λ system

As discussed in Chapters 3 and 4, and the corresponding appendices to those experiments (B and C), many of our procedures involving dark states are limited in fidelity, however, our understanding of the exact role that many of the sources of decoherence play is not complete. As discussed in §B.4 and §C.1, a number of factors play a role determining both the purity of the final dark state, as well as our ability to adiabatically shift the dark state across the Bloch sphere.

Most importantly, we are dealing with Λ systems that occur within a larger subspace of electronic levels, thus loss into and coupling to these other levels can be detrimental to our intended procedure. An ideal system consists of two ground states coupled to an excited level; however, the NV

center consists of three distinct spin sublevels in the ground state and six spin-orbit levels in the excited state. In the case of the experiments described in Chapter 3, the excited state of the Λ system was formed by an anticrossing to mix the two excited state spin sublevels of interest. This, however, also created a second level only 250 MHz detuned in energy to which coupling would produce an orthogonal dark state. In the case of the experiments described in Chapter 4, we used an already mixed excited state level, $|A_2\rangle$, that was well isolated from the next nearest level (2.9 GHz away in energy); however, it is weakly coupled to the reference ground state $|0_g\rangle$ leading to loss out of the intended subspace. In addition, the intersystem crossing in the NV center, while beneficial in providing room temperature readout and initialization of the spin state, acts as another mechanism for loss out of our subspace. To combat this in the Berry phase experiments, we used an excited level that has very little coupling to the singlet levels through the intersystem crossing in $|A_2\rangle$.

In addition to the role that other levels play, we suspect that additional sidebands may play a significant role in the Berry phase experiments (Ch. 4). Here, unlike in Chapter 3, the ground state splitting is much smaller (655 MHz vs. 4.6 GHz), and thus at longer timescales, the additional detuned harmonics produced by the EOM, may drive the Λ system in unintended ways. We suggest that this plays a role in the long-time decay mechanism seen in the Berry phase visibility in Fig. 4.11. Other mecha-

nisms such as spectral diffusion and the intrinsic nuclear hyperfine levels within the ground state spin sublevels may also play a role in the decoherence of dark state purity and Berry phase visibility, but are relatively insignificant.

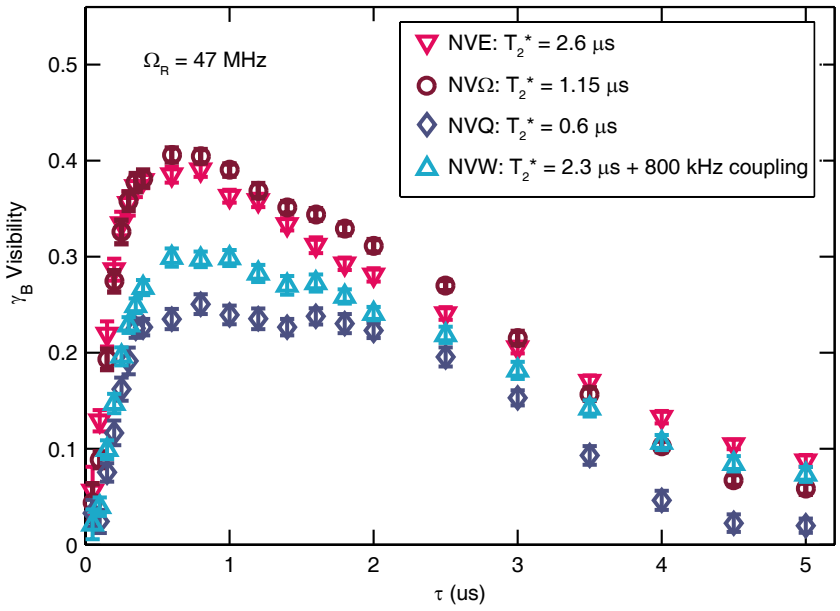

Figure D.2: Berry phase visibility for NV centers exhibiting different T_2^* times The visibility of the Berry phase, γ_B, as a function of traversal time, τ, for four different NV centers exhibiting different T_2^* spin coherence times driven at Ω_R = 47 MHz. The raspberry red points correspond to Berry phase visibility from NV "Euro", the NV center used in the experiments described in Ch. 4 and Appendix C

However, the role one decoherence mechanism is not as well understood. That is the role of the inhomogenous spin coherence decay, T_2^*, of the ground state spins, as well as coupling to nearby coupled spins. Our suspicion is that this decay time is frozen to some extent during the optical interaction, as is typically seen during a microwave Rabi oscillation, but

balances with the optical driving power to determine some final dark state purity. To fully investigate the role T_2^* plays within an optically driven Λ system, a systematic investigation of many NV centers would need to be performed in order to account for other variations between NV centers (spectral diffusion, strain splitting of the orbital levels, etc.). We took a brief foray into this by examining the Berry phase visibility of four NV centers as a function of STIRAP traversal time. The results, plotted in Fig. D.2, show the visibility of the Berry phase in a Hahn echoed sequence, similar to the $\Omega_R = 47\,\mathrm{MHz}$ data set in Fig. 4.11.

While the sample size is small (only four NV centers) it appears that in general the shorter the spin coherence time, the more reduced the visibility, suggesting poorer dark state purity. However, this is not fully consistent across the four NV centers measured. In particular, the NV center that is strongly coupled to a nearby spin with a coupling strength of $\approx 800\,\mathrm{kHz}$ has a reduced visibility when compared to NV centers of similar or lesser T_2^* times.

While we could perhaps extract some general trends, accounting for the role that this decay time plays in a quantum master equation approach model as seen in Appendix C has thus far yielded no qualitative match to experiments. Thus, it remains unanswered as to what exactly the interplay is between this spin dephasing and optical driving and how it affects the purity of the dark state.

References

[1] I. Newton, *Opticks: or a Treatise of the Reflexions, Refractions, Inflexions, and Colours of Light* (1704).

[2] J. Fraunhofer, *Denkschriften der Königlichen Akad. der Wissenschaften zu München* **5**, 193 (1814).

[3] J. Fraunhofer, *Denkschriften der Königlichen Akad. der Wissenschaften zu München* **8**, 3 (1821).

[4] M. Planck, *Verhandlungen der Dtsch. Phys. Gesellschaft* **2**, 237 (1900).

[5] A. Einstein, *Ann. Phys.* **17**, 132 (1905).

[6] T. H. Maiman, *Nature* **187**, 493 (1960).

[7] D. J. Wineland, *Rev. Mod. Phys.* **85**, 1103 (2013).

[8] S. Haroche, *Rev. Mod. Phys.* **85**, 1083 (2013).

[9] C. C. Gerry, P. L. Knight, *Introductory Quantum Optics* (Cambridge University Press, New York, 2005).

[10] J. Stark, *Ann. Phys.* **43**, 965 (1914).

[11] B. B. Buckley, Coherent light-matter interactions of defect spins in solids, Ph.D. thesis, University of California, Santa Barbara (2013).

[12] H. R. Gray, R. M. Whitley, C. R. Stroud, *Opt. Lett.* **3**, 218 (1978).

[13] M. Fleischhauer, A. Imamoglu, J. P. Marangos, *Rev. Mod. Phys.* **77**, 633 (2005).

[14] K. Bergmann, H. Theuer, B. W. Shore, *Rev. Mod. Phys.* **70**, 1003 (1998).

[15] C. Santori, P. Tamarat, P. Neumann, J. Wrachtrup, D. Fattal, R. G. Beausoleil, J. Rabeau, P. Olivero, A. D. Greentree, S. Prawer, F. Jelezko, P. Hemmer, *Phys. Rev. Lett.* **97**, 247401 (2006).

[16] E. Togan, Y. Chu, A. Imamolu, M. D. Lukin, *Nature* **478**, 497 (2011).

[17] D. A. Golter, K. N. Dinyari, H. Wang, *Phys. Rev. A* **87**, 35801 (2013).

[18] X. D. Xu, B. Sun, P. R. Berman, D. G. Steel, A. S. Bracker, D. Gammon, L. J. Sham, *Nature Phys.* **4**, 692 (2008).

[19] W. R. Kelly, Z. Dutton, J. Schlafer, B. Mookerji, T. A. Ohki, J. S. Kline, D. P. Pappas, *Phys. Rev. Lett.* **104**, 163601 (2010).

[20] C. H. Dong, V. Fiore, M. C. Kuzyk, H. L. Wang, *Science* **338**, 1609 (2012).

[21] D. J. Wineland, C. Monroe, W. M. Itano, B. E. King, D. Leibfried, D. M. Meekhof, C. Myatt, C. Wood, *Fortschritte Der Phys.* **46**, 363 (1998).

[22] H. Goto, K. Ichimura, *Phys. Rev. A* **74**, 53410 (2006).

[23] D. A. Golter, H. Wang, *Phys. Rev. Lett.* **112**, 116403 (2014).

[24] G. Davies, M. F. Hamer, *Proc. R. Soc. London A Math. Phys. Sci.* **348**, 285 (1976).

[25] A. Gruber, A. Drabenstedt, C. Tietz, L. Fleury, J. Wrachtrup, C. von Borczyskowski, *Science* **276**, 2012 (1997).

[26] M. W. Doherty, N. B. Manson, P. Delaney, F. Jelezko, J. Wrachtrup, L. C. Hollenberg, *Phys. Rep.* **528**, 1 (2013).

[27] M. W. Doherty, N. B. Manson, P. Delaney, L. C. L. Hollenberg, *New J. Phys.* **13** (2011).

[28] J. R. Maze, A. Gali, E. Togan, Y. Chu, A. Trifonov, E. Kaxiras, M. D. Lukin, *New J. Phys.* **13** (2011).

[29] J. R. Weber, W. F. Koehl, J. B. Varley, A. Janotti, B. B. Buckley, C. G. Van de Walle, D. D. Awschalom, *Proc. Natl. Acad. Sci. U. S. A.* **107**, 8513 (2010).

[30] W. F. Koehl, B. B. Buckley, F. J. Heremans, G. Calusine, D. D. Awschalom, *Nature* **479**, 84 (2011).

[31] A. L. Falk, B. B. Buckley, G. Calusine, W. F. Koehl, V. V. Dobrovitski, A. Politi, C. A. Zorman, P. X.-L. Feng, D. D. Awschalom, *Nature Commun.* **4**, 1819 (2013).

[32] D. J. Christle, A. L. Falk, P. Andrich, P. V. Klimov, J. U. Hassan, N. T. Son, E. Janzén, T. Ohshima, D. D. Awschalom, *Nature Mater.* **14**, 160 (2015).

[33] A. Batalov, V. Jacques, F. Kaiser, P. Siyushev, P. Neumann, L. J. Rogers, R. L. McMurtrie, N. B. Manson, F. Jelezko, J. Wrachtrup, *Phys. Rev. Lett.* **102**, 195506 (2009).

[34] L. C. Bassett, F. J. Heremans, D. J. Christle, C. G. Yale, G. Burkard, B. B. Buckley, D. D. Awschalom, *Science* **345**, 1333 (2014).

[35] K. M. Fu, C. Santori, P. E. Barclay, L. J. Rogers, N. B. Manson, R. G. Beausoleil, *Phys. Rev. Lett.* **103**, 256404 (2009).

[36] L. J. Rogers, R. L. McMurtrie, M. J. Sellars, N. B. Manson, *New J. Phys.* **11**, 063007 (2009).

[37] W. B. Gao, A. Imamoglu, H. Bernien, R. Hanson, *Nature Photon.* **9**, 363 (2015).

[38] L. Robledo, L. Childress, H. Bernien, B. Hensen, P. F. Alkemade, R. Hanson, *Nature* **477**, 574 (2011).

[39] L. Robledo, H. Bernien, T. van der Sar, R. Hanson, *New J. Phys.* **13**, 25013 (2011).

[40] E. Togan, Y. Chu, A. S. Trifonov, L. Jiang, J. Maze, L. Childress, M. V. G. Dutt, A. S. Sorensen, P. R. Hemmer, A. S. Zibrov, M. D. Lukin, *Nature* **466**, 730 (2010).

[41] H. Kosaka, N. Niikura, *Phys. Rev. Lett.* **114**, 53603 (2015).

[42] B. B. Buckley, G. D. Fuchs, L. C. Bassett, D. D. Awschalom, *Science* **330**, 1212 (2010).

[43] H. Bernien, L. Childress, L. Robledo, M. Markham, D. Twitchen, R. Hanson, *Phys. Rev. Lett.* **108**, 43604 (2012).

[44] A. Sipahigil, M. L. Goldman, E. Togan, Y. Chu, M. Markham, D. J. Twitchen, A. S. Zibrov, A. Kubanek, M. D. Lukin, *Phys. Rev. Lett.* **108**, 143601 (2012).

[45] L. C. Bassett, F. J. Heremans, C. G. Yale, B. B. Buckley, D. D. Awschalom, *Phys. Rev. Lett.* **107**, 266403 (2011).

[46] H. Bernien, B. Hensen, W. Pfaff, G. Koolstra, M. S. Blok, L. Robledo, T. H. Taminiau, M. Markham, D. J. Twitchen, L. Childress, R. Hanson, *Nature* **497**, 86 (2013).

[47] W. Pfaff, B. J. Hensen, H. Bernien, S. B. van Dam, M. S. Blok, T. H. Taminiau, M. J. Tiggelman, R. N. Schouten, M. Markham, D. J. Twitchen, R. Hanson, *Science* **345**, 532 (2014).

[48] R. E. George, L. M. Robledo, O. J. Maroney, M. S. Blok, H. Bernien, M. L. Markham, D. J. Twitchen, J. J. Morton, G. A. Briggs, R. Hanson, *Proc. Natl. Acad. Sci. U. S. A.* **110**, 3777 (2013).

[49] B. Hensen, H. Bernien, A. E. Dréau, A. Reiserer, N. Kalb, M. S. Blok, J. Ruitenberg, R. F. L. Vermeulen, R. N. Schouten, C. Abellán, W. Amaya, V. Pruneri, M. W. Mitchell, M. Markham, D. J. Twitchen, D. Elkouss, S. Wehner, T. H. Taminiau, R. Hanson, *arXiv* **1508.05949** (2015).

[50] M. Lončar, A. Faraon, *MRS Bull.* **38**, 144 (2013).

[51] A. Faraon, P. E. Barclay, C. Santori, K. M. C. Fu, R. G. Beausoleil, *Nature Photon.* **5**, 301 (2011).

[52] A. Faraon, C. Santori, Z. H. Huang, V. M. Acosta, R. G. Beausoleil, *Phys. Rev. Lett.* **109** (2012).

[53] T. M. Babinec, B. J. M. Hausmann, M. Khan, Y. Zhang, J. R. Maze, P. R. Hemmer, M. Loncar, *Nature Nanotechnol.* **5**, 195 (2010).

[54] J. C. Lee, D. O. Bracher, S. Cui, K. Ohno, C. A. McLellan, X. Zhang, P. Andrich, B. Alemán, K. J. Russell, A. P. Magyar, I. Aharonovich,

A. Bleszynski Jayich, D. Awschalom, E. L. Hu, *Appl. Phys. Lett.* **105**, 261101 (2014).

[55] C. G. Yale, B. B. Buckley, D. J. Christle, G. Burkard, F. J. Heremans, L. C. Bassett, D. D. Awschalom, *Proc. Natl. Acad. Sci. U. S. A.* **110**, 7595 (2013).

[56] C. G. Yale, F. J. Heremans, B. B. Zhou, A. Auer, G. Burkard, D. D. Awschalom, *arXiv* **1507.08993** (2015).

[57] F. J. Heremans, Engineering and Manipulating Single Spins in Diamond, Ph.D. thesis, University of California, Santa Barbara (2013).

[58] J. R. Maze, P. L. Stanwix, J. S. Hodges, S. Hong, J. M. Taylor, P. Cappellaro, L. Jiang, M. V. Dutt, E. Togan, A. S. Zibrov, A. Yacoby, R. L. Walsworth, M. D. Lukin, *Nature* **455**, 644 (2008).

[59] G. Balasubramanian, I. Y. Chan, R. Kolesov, M. Al-Hmoud, J. Tisler, C. Shin, C. Kim, A. Wojcik, P. R. Hemmer, A. Krueger, T. Hanke, A. Leitenstorfer, R. Bratschitsch, F. Jelezko, J. Wrachtrup, *Nature* **455**, 648 (2008).

[60] B. J. Maertz, A. P. Wijnheijmer, G. D. Fuchs, M. E. Nowakowski, D. D. Awschalom, *Appl. Phys. Lett.* **96** (2010).

[61] F. Dolde, H. Fedder, M. W. Doherty, T. Nobauer, F. Rempp, G. Balasubramanian, T. Wolf, F. Reinhard, L. C. L. Hollenberg, F. Jelezko, J. Wrachtrup, *Nature Phys.* **7**, 459 (2011).

[62] E. Vanoort, M. Glasbeek, *Chem. Phys. Lett.* **168**, 529 (1990).

[63] P. Tamarat, T. Gaebel, J. R. Rabeau, M. Khan, A. D. Greentree, H. Wilson, L. C. Hollenberg, S. Prawer, P. Hemmer, F. Jelezko, J. Wrachtrup, *Phys. Rev. Lett.* **97**, 83002 (2006).

[64] P. Tamarat, N. B. Manson, J. P. Harrison, R. L. McMurtrie, A. Nizovtsev, C. Santori, R. G. Beausoleil, P. Neumann, T. Gaebel, F. Jelezko, P. Hemmer, J. Wrachtrup, *New J. Phys.* **10** (2008).

[65] J. Isberg, A. Tajani, D. J. Twitchen, *Phys. Rev. B* **73** (2006).

[66] R. G. Farrer, *Solid State Commun.* **7**, 685 (1969).

[67] J. Rosa, M. Vanecek, M. Nesladek, L. M. Stals, *Diam. Relat. Mater.* **8**, 721 (1999).

[68] F. J. Heremans, G. D. Fuchs, C. F. Wang, R. Hanson, D. D. Awschalom, *Appl. Phys. Lett.* **94** (2009).

[69] S. D. Barrett, P. Kok, *Phys. Rev. A* **71**, 60310 (2005).

[70] L. Childress, J. M. Taylor, A. S. Sorensen, M. D. Lukin, *Phys. Rev. A* **72** (2005).

[71] B. B. Blinov, D. Leibfried, C. Monroe, D. J. Wineland, *Quantum Inf. Process.* **3**, 45 (2004).

[72] K. J. Boller, A. Imamolu, S. E. Harris, *Phys. Rev. Lett.* **66**, 2593 (1991).

[73] D. Budker, D. F. Kimball, S. M. Rochester, V. V. Yashchuk, *Phys. Rev. Lett.* **83**, 1767 (1999).

[74] J. Vanier, *Appl. Phys. B-Lasers Opt.* **81**, 421 (2005).

[75] A. Aspect, E. Arimondo, R. Kaiser, N. Vansteenkiste, C. Cohen-Tannoudji, *Phys. Rev. Lett.* **61**, 826 (1988).

[76] F. Hilser, G. Burkard, *Phys. Rev. B* **86**, 125204 (2012).

[77] J. Berezovsky, M. H. Mikkelsen, N. G. Stoltz, L. A. Coldren, D. D. Awschalom, *Science* **320**, 349 (2008).

[78] K. W. Murch, U. Vool, D. Zhou, S. J. Weber, S. M. Girvin, I. Siddiqi, *Phys. Rev. Lett.* **109**, 183602 (2012).

[79] F. Jelezko, T. Gaebel, I. Popa, A. Gruber, J. Wrachtrup, *Phys. Rev. Lett.* **92**, 76401 (2004).

[80] V. V. Dobrovitski, A. E. Feiguin, D. D. Awschalom, R. Hanson, *Phys. Rev. B* **77** (2008).

[81] H. Kosaka, T. Inagaki, Y. Rikitake, H. Imamura, Y. Mitsumori, K. Edamatsu, *Nature* **457**, 702 (2009).

[82] J. E. Thomas, P. R. Hemmer, S. Ezekiel, C. C. Leiby, R. H. Picard, C. R. Willis, *Phys. Rev. Lett.* **48**, 867 (1982).

[83] D. M. Toyli, C. D. Weis, G. D. Fuchs, T. Schenkel, D. D. Awschalom, *Nano Lett.* **10**, 3168 (2010).

[84] J. Wrachtrup, F. Jelezko, *J. Phys.-Condens. Mat.* **18**, S807 (2006).

[85] R. Blume-Kohout, *New J. Phys.* **12** (2010).

[86] G. Lindblad, *Commun. Math. Phys.* **48**, 119 (1976).

[87] H.-P. Breuer, F. Petruccione, *The theory of open quantum systems* (Oxford University Press, Oxford ; New York, 2002).

[88] S. Pancharatnam, *Proc. Indian Acad. Sci. - Sect. A* **44**, 247 (1956).

[89] M. V. Berry, *Proc. R. Soc. London A Math. Phys. Eng. Sci.* **392**, 45 (1984).

[90] G. De Chiara, G. M. Palma, *Phys. Rev. Lett.* **91**, 090404 (2003).

[91] S. Berger, M. Pechal, A. A. Abdumalikov, C. Eichler, L. Steffen, A. Fedorov, A. Wallraff, S. Filipp, *Phys. Rev. A* **87**, 60303 (2013).

[92] P. Zanardi, M. Rasetti, *Phys. Lett. A* **264**, 94 (1999).

[93] L. M. Duan, J. I. Cirac, P. Zoller, *Science* **292**, 1695 (2001).

[94] J. Anandan, *Phys. Lett. A* **133**, 171 (1988).

[95] J. Jones, V. Vedral, A. Ekert, G. Castagnoli, *Nature* **403**, 869 (2000).

[96] D. Leibfried, B. DeMarco, V. Meyer, D. Lucas, M. Barrett, J. Britton, W. M. Itano, B. Jelenković, C. Langer, T. Rosenband, D. J. Wineland, *Nature* **422**, 412 (2003).

[97] P. J. Leek, J. M. Fink, A. Blais, R. Bianchetti, M. Göppl, J. M. Gambetta, D. I. Schuster, L. Frunzio, R. J. Schoelkopf, A. Wallraff, *Science* **318**, 1889 (2007).

[98] A. A. Abdumalikov Jr, J. M. Fink, K. Juliusson, M. Pechal, S. Berger, A. Wallraff, S. Filipp, *Nature* **496**, 482 (2013).

[99] C. Zu, W.-B. Wang, L. He, W.-G. Zhang, C.-Y. Dai, F. Wang, L.-M. Duan, *Nature* **514**, 72 (2014).

[100] S. Arroyo-Camejo, A. Lazariev, S. W. Hell, G. Balasubramanian, *Nature Commun.* **5**, 4870 (2014).

[101] K. Zhang, N. M. Nusran, B. R. Slezak, M. V. G. Dutt, *arXiv* **1410.2791** (2014).

[102] K. Toyoda, K. Uchida, A. Noguchi, S. Haze, S. Urabe, *Phys. Rev. A* **87**, 52307 (2013).

[103] Z. Kis, F. Renzoni, *Phys. Rev. A* **65**, 032318 (2002).

[104] D. Møller, L. B. Madsen, K. Mølmer, *Phys. Rev. A* **75**, 62302 (2007).

[105] U. Gaubatz, P. Rudecki, S. Schiemann, K. Bergmann, *J. Chem. Phys.* **92**, 5363 (1990).

[106] B. Pingault, J. N. Becker, C. H. H. Schulte, C. Arend, C. Hepp, T. Godde, A. I. Tartakovskii, M. Markham, C. Becher, M. Atatüre, *Phys. Rev. Lett.* **113**, 263601 (2014).

[107] L. J. Rogers, K. D. Jahnke, M. H. Metsch, A. Sipahigil, J. M. Binder, T. Teraji, H. Sumiya, J. Isoya, M. D. Lukin, P. Hemmer, F. Jelezko, *Phys. Rev. Lett.* **113**, 263602 (2014).

[108] J. Riedrich-Möller, C. Arend, C. Pauly, F. Mücklich, M. Fischer, S. Gsell, M. Schreck, C. Becher, *Nano Lett.* **14**, 5281 (2014).

[109] M. Widmann, S.-Y. Lee, T. Rendler, N. T. Son, H. Fedder, S. Paik, L.-P. Yang, N. Zhao, S. Yang, I. Booker, A. Denisenko, M. Jamali, S. A. Momenzadeh, I. Gerhardt, T. Ohshima, A. Gali, E. Janzén, J. Wrachtrup, *Nature Mater.* **14**, 164 (2015).

[110] N. R. Jungwirth, Y. Y. Pai, H. S. Chang, E. R. MacQuarrie, K. X. Nguyen, G. D. Fuchs, *J. Appl. Phys.* **116**, 043509 (2014).

[111] R. Kolesov, *Phys. Rev. A* **72**, 051801 (2005).

[112] K. Xia, R. Kolesov, Y. Wang, P. Siyushev, R. Reuter, T. Kornher, N. Kukharchyk, A. D. Wieck, B. Villa, S. Yang, J. Wrachtrup, *Phys. Rev. Lett.* **115**, 093602 (2015).

[113] J. Hansom, C. H. H. Schulte, C. Le Gall, C. Matthiesen, E. Clarke, M. Hugues, J. M. Taylor, M. Atatüre, *Nature Phys.* **10**, 725 (2014).

[114] C. López, *Adv. Mater.* **15**, 1679 (2003).

[115] L. Marseglia, J. P. Hadden, A. C. Stanley-Clarke, J. P. Harrison, B. Patton, Y. L. D. Ho, B. Naydenov, F. Jelezko, J. Meijer, P. R. Dolan, J. M. Smith, J. G. Rarity, J. L. O'Brien, *Appl. Phys. Lett.* **98**, 133107 (2011).

[116] N. Aslam, G. Waldherr, P. Neumann, F. Jelezko, J. Wrachtrup, *New J. Phys.* **15** (2013).

[117] G. D. Fuchs, A. L. Falk, V. V. Dobrovitski, D. D. Awschalom, *Phys. Rev. Lett.* **108**, 157602 (2012).

[118] T. Hirayama, M. Sheik-Bahae, *Opt. Lett.* **27**, 860 (2002).

[119] A. Lenef, S. W. Brown, D. A. Redman, S. C. Rand, J. Shigley, E. Fritsch, *Phys. Rev. B* **53**, 13427 (1996).

[120] G. D. Fuchs, V. V. Dobrovitski, D. M. Toyli, F. J. Heremans, D. D. Awschalom, *Science* **326**, 1520 (2009).

[121] A. Gilchrist, N. K. Langford, M. A. Nielsen, *Phys. Rev. A* **71**, 062310 (2005).

[122] A. Faraon, C. Santori, Z. Huang, K.-M. C. Fu, V. M. Acosta, D. Fattal, R. G. Beausoleil, *New J. Phys.* **15**, 025010 (2013).

[123] J. J. García-Ripoll, P. Zoller, J. I. Cirac, *Phys. Rev. Lett.* **91**, 157901 (2003).

[124] M. J. Madsen, D. L. Moehring, P. Maunz, R. N. Kohn, L.-M. Duan, C. Monroe, *Phys. Rev. Lett.* **97**, 040505 (2006).

[125] G. Romero, D. Ballester, Y. M. Wang, V. Scarani, E. Solano, *Phys. Rev. Lett.* **108**, 120501 (2012).

[126] V. M. Acosta, C. Santori, A. Faraon, Z. Huang, K.-M. C. Fu, A. Stacey, D. A. Simpson, K. Ganesan, S. Tomljenovic-Hanic, A. D. Greentree, S. Prawer, R. G. Beausoleil, *Phys. Rev. Lett.* **108**, 206401 (2012).

[127] O. V. Zwier, D. O'Shea, A. R. Onur, C. H. van der Wal, *Sci. Rep.* **5**, 10931 (2015).

[128] T. Müller, C. Hepp, B. Pingault, E. Neu, S. Gsell, M. Schreck, H. Sternschulte, D. Steinmüller-Nethl, C. Becher, M. Atatüre, *Nature Commun.* **5**, 3328 (2014).

[129] C. Hepp, T. Müller, V. Waselowski, J. N. Becker, B. Pingault, H. Sternschulte, D. Steinmüller-Nethl, A. Gali, J. R. Maze, M. Atatüre, C. Becher, *Phys. Rev. Lett.* **112**, 036405 (2014).

[130] A. Sipahigil, K. Jahnke, L. Rogers, T. Teraji, J. Isoya, A. Zibrov, F. Jelezko, M. Lukin, *Phys. Rev. Lett.* **113**, 113602 (2014).

[131] P. V. Klimov, A. L. Falk, B. B. Buckley, D. D. Awschalom, *Phys. Rev. Lett.* **112**, 087601 (2014).

[132] A. L. Falk, P. V. Klimov, B. B. Buckley, V. Ivády, I. A. Abrikosov, G. Calusine, W. F. Koehl, A. Gali, D. D. Awschalom, *Phys. Rev. Lett.* **112**, 187601 (2014).

[133] G. Calusine, A. Politi, D. D. Awschalom, *Appl. Phys. Lett.* **105**, 011123 (2014).

[134] M. Zhong, M. P. Hedges, R. L. Ahlefeldt, J. G. Bartholomew, S. E. Beavan, S. M. Wittig, J. J. Longdell, M. J. Sellars, *Nature* **517**, 177 (2015).

[135] C. Clausen, I. Usmani, F. Bussières, N. Sangouard, M. Afzelius, H. de Riedmatten, N. Gisin, *Nature* **469**, 508 (2011).

[136] D. M. Toyli, D. J. Christle, A. Alkauskas, B. B. Buckley, C. G. Van de Walle, D. D. Awschalom, *Phys. Rev. X* **2**, 31001 (2012).

[137] V. V. Dobrovitski, G. de Lange, D. Riste, R. Hanson, *Phys. Rev. Lett.* **105** (2010).

[138] P. B. Slater, *Phys. Lett. A* **247**, 1 (1998).

[139] E. Laloy, J. A. Vrugt, *Water Resour. Res.* **48**, W01526 (2012).

[140] J. S. Liu, F. Liang, W. H. Wong, *J. Am. Stat. Assoc.* **95**, 121 (2000).

[141] M.-H. Chen, Q.-M. Shao, *J. Comput. Graph. Stat.* **8**, 69 (1999).

[142] C. W. Gardiner, P. Zoller, *Quantum Noise* (Springer, Berlin, 2004).

[143] D. Møller, L. B. Madsen, K. Mølmer, *Phys. Rev. A* **77**, 022306 (2008).

[144] A. Batalov, C. Zierl, T. Gaebel, P. Neumann, I. Y. Chan, G. Balasubramanian, P. R. Hemmer, F. Jelezko, J. Wrachtrup, *Phys. Rev. Lett.* **100** (2008).